BINARIES AND THE DYNAMICAL EVOLUTION OF GLOBULAR CLUSTERS

by

Jun Ji

A dissertation submitted in partial fulfillment
of the requirements for the degree of
Doctor of Philosophy
(Astronomy and Astrophysics)
in The University of Michigan
2011

Doctoral Committee:

Professor Joel N. Bregman, Chair
Professor Fred C. Adams
Professor Mario L. Mateo
Associate Professor Jon Matthew Miller
Associate Professor John D. Monnier
Assistant Professor Oleg Y. Gnedin

To my wife *Yanpeng* and my son *Dennis*

ACKNOWLEDGEMENTS

There are many people who I would like to acknowledge at this milestone in my life. First and foremost, I would like to thank my wife Yanpeng, who gave me courage when I was at the bottom, and pushed me hard when I was procrastinating. I would like to thank my son Dennis, who brought me lots of fun to pass my Dark Age and help me feel the responsibility as a father.

I would like to give my special thanks to my advisor, Joel Bregman, for his mentorship and support. I made two big decisions in my life when I was at Ann Arbor, getting married and having a baby. Without Joel's great support, I couldn't move to my wife in Arkansas and still keep my research continuing. I appreciate that he understands how life will change when having a new baby, and appreciate his tolerance on the slow progress of my research. I would also like to thank Joel for his patience and efforts on improving my English grammar, especially when writing papers, dissertation, and proposals.

I thank my committee, Mario Mateo, Jon Miller, John Monnier, Oleg Gnedin, and Fred Adams, for taking their time to be involved with my studies and gave me valuable advice for my thesis. I would like to acknowledge the staff (Ann Smith, Brian Cox, Sarah Lloyd, and Roy Bonser) of the Michigan Astronomy Department. Without their support, life would be much tougher.

I would like to give my special gratitude to my fellow graduate students at U of M. Jeffrey Fogel, my former officemate, had lots of chats with me and helped me through the first few months of ”cultural shock”. Jessica Werk, whose jokes I never got, I admire your leadership, initiative, and passion. Zhaohuan Zhu, who gave me countless free rides to and from the airport, I admire your smartness and hardworking. Javier Alonso, who occasionally shouted in his office, gave me countless help in my research. There are also many other former and current graduate students whom I would never forget. I had many precious memories with you guys at the happy hours, mock thanksgiving dinner, wine and cheers party, Anime night, apple picking, corn maze, football party, Halloween and Christmas party, and air-hockey tournament. Without you guys, there would be no life for me outside of research at Ann Arbor.

I would also like to express my thanks to my mom and dad and my mother in law, who came to Arkansas and helped us take care of our son for several months, despite the boring and lonely life during that time.

Without any of you, I couldn't finish my thesis and be where I am today. I give my truly gratitude from my heart to all of you!

TABLE OF CONTENTS

DEDICATION ii

ACKNOWLEDGEMENTS iii

LIST OF FIGURES viii

LIST OF TABLES xi

LIST OF APPENDICES xiii

ABSTRACT xiv

CHAPTER

1. Introduction 1

- 1.1 Early Theories for the Globular Cluster Dynamical Evolution 1
- 1.2 The Modern Simulations for the Globular Cluster Dynamical Evolution Including Binaries 5
  - 1.2.1 Monte-Carlo Simulations 5
  - 1.2.2 N-body Simulations 9
  - 1.2.3 Full Analytical Analysis 9
  - 1.2.4 Their Agreements and Divergences 9
- 1.3 The Observations of the Globular Cluster Binaries 13
  - 1.3.1 X-ray Point Sources in Globular Clusters 13
  - 1.3.2 Radial Velocity Variables 14
  - 1.3.3 Eclipsing Binaries 15
  - 1.3.4 Photometric Binaries from the Color-magnitude Diagrams 16
- 1.4 Outline of this Thesis Work 20

2. HST Observations of Globular Cluster Binaries: Methodology 21

- 2.1 Sample Selection 21
- 2.2 Data Reduction and Photometry 22

2.3 The Artificial Star Tests 29
    2.3.1 Defining the Main-sequence Ridge Line 29
    2.3.2 Performing the Artificial Star Tests 31
    2.3.3 Photometric Accuracy, Uncertainty, and Completeness 31
2.4 The High Mass-ratio Binary Fraction 33
    2.4.1 The Model for the Superposition of Stars 35
    2.4.2 The Model for the Field Star Population 37
    2.4.3 Estimate the High Mass-ratio Binary Fraction . . . 37
2.5 The Global Binary Fractions 39
    2.5.1 The Star Counting Method 39
    2.5.2 The χ^2 Fitting Method 41
2.6 The Binary Fraction Radial Analysis 43
    2.6.1 The Analyzing Method 46
    2.6.2 The Radial CMD Qualities 46
2.7 Discussions on the Techniques 46
    2.7.1 The Photometric Errors 47
    2.7.2 The Metallicity Dispersion 47
    2.7.3 The Differential Reddening 48

3. HST Observations of Globular Cluster Binaries: Results . . 49

3.1 Binary Fractions within the Whole Field of View 49
3.2 Binary Fractions within the Half-mass Radius 52
3.3 Binary Fractions within the Core Regions 59
3.4 The Radial Distribution of the Binary Fractions 65
3.5 The Catalog for the High Mass-ratio Binary Candidates . . . 67
    3.5.1 Selecting Criteria 69
    3.5.2 The Catalog 70
    3.5.3 The Properties of the Binary Candidates 73

4. Summary and Future Work 75

4.1 Summary 75
    4.1.1 Summary of the Methodology 75
    4.1.2 Summary of the Results 75
4.2 Future Work 77
    4.2.1 Improvement for the PSF Fitting Program 77
    4.2.2 Proper Motion to Screen Field Stars 77
    4.2.3 Studies with the Ground-based Telescopes 78
    4.2.4 Studies on the White Dwarf Populations 78
    4.2.5 Correlation of Binary Fractions with X-ray Point Source Frequencies in Globular Clusters 79

APPENDICES 80

BIBLIOGRAPHY 228

LIST OF FIGURES

Figure

1.1 Comparisons of the surface brightness profiles for globular clusters . 3
1.2 Monte-Carlo simulations by Fregeau et al. (2003) 7
1.3 The ratios of the core to the half-mass radius Vs. binary fractions by Fregeau & Rasio (2007) 8
1.4 Binary fractions evolving with time by Ivanova et al. (2005) 8
1.5 Binary fractions evolving with time by Chatterjee et al. (2010) . . . 8
1.6 The N-body simulations by Hurley et al. (2007) 10
1.7 An example of N-body simulation for NGC 6397 by Hurley et al. (2008) 11
1.8 Binary radial distributions and mass-ratio distributions by Sollima (2008). 12
1.9 Chandra X-ray images for globular clusters 14
1.10 Radial velocity variable in M3 (Hut et al., 1992a) 15
1.11 The light curves of three eclipsing binaries in NGC 5466 (Mateo et al., 1990). 16
1.12 The photometric binaries from the CMD of NGC 5053 17
1.13 Comparisons of images of 47 Tuc between VLT and HST 19
2.1 Distributions of properties for the sample 24
2.2 Comparisons of the CMD quality between Dolphot V1.0 and V1.2 . 27
2.3 Example for the observed CMD and the straightened CMD: NGC 4590 30
2.4 Examples of images and fake CMDs: NGC 5053 and NGC 1851 . . 32
2.5 Examples for the artificial star tests: NGC 5053 and NGC 1851 . . 34
2.6 Demonstration of the regions when measuring the minimum binary fraction for NGC 5053 and NGC 2808 40
2.7 The residual color distribution fitted by only Gaussian model and by the best-fit model 44
2.8 Model components for the fitting 45
2.9 Isochrone Models at different metallicity. 48
3.1 Comparisons of binary fractions from the whole field of view between different methods 53
3.2 The binary mass ratio distribution function constrained by the sample results 53
3.3 Same as Figure 3.1, but for half-mass radius results. 56

3.4 The half-mass radius binary fractions Vs. different cluster properties 58
3.5 Core binary fractions Vs. different cluster properties 61
3.6 Same as Figure 3.1, but for all radial bin results. 66
3.7 Combined high mass-ratio ($q > 0.5$) binary fractions Vs. radius . . . 68
3.8 The CMDs for selecting high mass-ratio binary candidates. 71
3.9 The CMDs for selecting high mass-ratio binary candidates (continued) 72
3.10 The CMDs for selecting high mass-ratio binary candidates (continued). 73
3.11 Properties of the high mass-ratio binary candidates in the catalog . 74
A.1 Semi-major axis VS. planet minimum mass for 228 extra-solar planets 87
B.1 Monte Carlo simulation rules for determining the frequency of blending of stars 91
B.2 Monte Carlo simulation results for the blending effect 91
D.1 Initial mass function and the resulted binary mass-ratio distribution for α in the range of (-2,3) 97
D.2 Initial mass function and the resulted binary mass-ratio distribution for three common IMFs 98
E.1 ngc104 100
E.2 ngc288 101
E.3 ngc362 102
E.4 ngc1851 103
E.5 ngc2808 104
E.6 ngc4590 105
E.7 ngc5053 106
E.8 m3 107
E.9 ngc5466 108
E.10 ngc5897 109
E.11 ngc5904 110
E.12 ngc5927 111
E.13 ngc6093 112
E.14 ngc6101 113
E.15 ngc6121 114
E.16 m13 115
E.17 ngc6218 116
E.18 ngc6341 117
E.19 ngc6352 118
E.20 ngc6362 119
E.21 ngc6397 120
E.22 ngc6541 121
E.23 ngc6624 122
E.24 ngc6637 123
E.25 ngc6652 124
E.26 ngc6656 125
E.27 ngc6723 126
E.28 ngc6752 127
E.29 ngc6809 128

E.30 ngc6981 129
E.31 ngc7078 130
E.32 ngc7099 131
E.33 Arp2 132
E.34 Palomar12 133
E.35 Terzan7 134
F.1 Radial analysis for ngc104 136
F.2 Radial analysis for ngc288 137
F.3 Radial analysis for ngc362 138
F.4 Radial analysis for ngc1851 139
F.5 Radial analysis for ngc2808 140
F.6 Radial analysis for ngc4590 141
F.7 Radial analysis for ngc5053 142
F.8 Radial analysis for m3 143
F.9 Radial analysis for ngc5466 144
F.10 Radial analysis for ngc5897 145
F.11 Radial analysis for ngc5904 146
F.12 Radial analysis for ngc5927 147
F.13 Radial analysis for ngc6093 148
F.14 Radial analysis for ngc6101 149
F.15 Radial analysis for ngc6121 150
F.16 Radial analysis for m13 151
F.17 Radial analysis for ngc6218 152
F.18 Radial analysis for ngc6341 153
F.19 Radial analysis for ngc6352 154
F.20 Radial analysis for ngc6362 155
F.21 Radial analysis for ngc6397 156
F.22 Radial analysis for ngc6541 157
F.23 Radial analysis for ngc6624 158
F.24 Radial analysis for ngc6637 159
F.25 Radial analysis for ngc6652 160
F.26 Radial analysis for ngc6656 161
F.27 Radial analysis for ngc6723 162
F.28 Radial analysis for ngc6752 163
F.29 Radial analysis for ngc6809 164
F.30 Radial analysis for ngc6981 165
F.31 Radial analysis for ngc7078 166
F.32 Radial analysis for ngc7099 167
F.33 Radial analysis for Arp2 168
F.34 Radial analysis for Palomar12 169
F.35 Radial analysis for Terzan7 170

LIST OF TABLES

Table

2.1 Basic properties of the Galactic globular clusters in the sample[a] . . 23
2.2 HST ACS observation log 25
2.3 Example of the fitting results for NGC 4590. 43
3.1 Fitting results for whole field of view 54
3.2 Fitting results within half light radius 55
3.3 Fitting results for the half-mass binary fractions Vs. different properties of clusters 57
3.4 The core binary fractions for 25 clusters with the high q method . . 60
3.5 Fitting results for the core binary fractions Vs. different properties of clusters 60
3.6 Fitting results for radial bins 62
3.7 Fitting results for binary fractions vs. radius. 67
G.1 Main-sequence binary candidate catalog for ngc288 172
G.2 Main-sequence binary candidate catalog for ngc362 175
G.3 Main-sequence binary candidate catalog for ngc1851 177
G.4 Main-sequence binary candidate catalog for ngc4590 179
G.5 Main-sequence binary candidate catalog for ngc5053 182
G.6 Main-sequence binary candidate catalog for ngc5466 184
G.7 Main-sequence binary candidate catalog for ngc5897 187
G.8 Main-sequence binary candidate catalog for ngc5904 191
G.9 Main-sequence binary candidate catalog for ngc6093 193
G.10 Main-sequence binary candidate catalog for ngc6101 195
G.11 Main-sequence binary candidate catalog for ngc6121 199
G.12 Main-sequence binary candidate catalog for ngc6218 201
G.13 Main-sequence binary candidate catalog for ngc6341 204
G.14 Main-sequence binary candidate catalog for ngc6362 207
G.15 Main-sequence binary candidate catalog for ngc6723 210
G.16 Main-sequence binary candidate catalog for ngc6752 212
G.17 Main-sequence binary candidate catalog for ngc6809 213
G.18 Main-sequence binary candidate catalog for ngc6981 216
G.19 Main-sequence binary candidate catalog for ngc7099 218
G.20 Main-sequence binary candidate catalog for m13 220

G.21 Main-sequence binary candidate catalog for Palomar12 222
G.22 Main-sequence binary candidate catalog for Terzan7 223
G.23 Main-sequence binary candidate catalog for Arp2 226

LIST OF APPENDICES

Appendix

A. Discussions on Hard Binaries and Planets in Globular Clusters 81

B. Estimate and Simulations of Superposition of Stars 88

C. Error Estimate for Binary Fractions 92

D. The Effect of the Stellar Initial Mass Function of Globular Clusters on the Binary Mass-ratio Distribution 94

E. Images, CMDs, LFs, and Residual Color Distributions for the Whole Field of View 99

F. CMDs, Residual Color Distributions, Binary Fractions Radial Distributions, and LFs for the Annular Bins 135

G. High Mass-ratio ($q > 0.5$) Binary Candidate Catalog 171

ABSTRACT

Binaries are thought to be the primary heating source in globular clusters, since they can heat the environment of globular clusters by converting their binding energy to the kinetic energy of the incoming stars through the dynamical interactions. Even a small primordial binary fraction is sufficient to postpone globular clusters from the core collapse for many relaxation times. So the binary fraction is an essential parameter which can dramatically affect the dynamical evolution of globular clusters. In this thesis work, I determined the binary fractions for a sample of 35 Galactic globular clusters with their color-magnitude diagrams (CMDs), which covers a wide range of the dynamical ages and metallicity. Those CMDs were constructed with the PSF photometry by Dolphot (V1.2) from their HST ACS archival data. Three different methods were used to estimate the binary fractions within the core, the half-mass radius, and the whole field of view regions. The binary fractions along the cluster radial bins were also analyzed. From the results, I found that the mean binary fractions within the core and the half-mass radii are 7.0% and 5.6%, respectively. The binary fractions within the core and the half-mass radii correlate with the cluster ages, with decreasing binary fractions against time, but not with their dynamical times and metallicity. The binary fractions within the half-mass radius also correlate with the cluster absolute V magnitudes, with fainter clusters having higher binary fractions. The radial distribution of the binary fractions show a significant correlation with the cluster radii, with decreasing values outwards. This is consistent with the mass segregation effect predicted by the simulations of the dynamical evolution of globular clusters. I also compiled a catalog containing 6,004 high mass-ratio binary candidates

selected from 23 Galactic globular clusters in our sample through their CMDs, which can be used to search the main-sequence-main-sequence binaries in globular clusters with the future radial velocity observations.

CHAPTER 1

Introduction

Globular clusters (GCs) are very old and simple systems in the Universe, as they only contain stars while having not much gas, dust, and dark matter. Those star systems usually have 10^5 to 10^6 old population stars (Hut et al., 1992a) only interacting with each other through the gravitational forces. Even in such a simple stellar environment, there are many questions unanswered. One of them is how they dynamically evolve.

1.1 Early Theories for the Globular Cluster Dynamical Evolution

There were large amount of studies over the last few decades focusing on how globular clusters evolve under the gravitational forces (see Elson et al. (1987), Spitzer (1987), and Hut et al. (1992a) for intense review). Early theories suggest four distinguished stages during the whole life of a globular cluster, according to its core radius, where the surface brightness is half of its central value (Spitzer, 1987), and its total mass. They are initial contraction, core collapse (Lynden-Bell & Wood, 1968; Cohn, 1980; Lynden-Bell & Eggleton, 1980), core oscillations (Sugimoto & Bettwieser, 1983; Bettwieser & Sugimoto, 1984), and evaporation (Spitzer, 1940). During the initial contraction stage, the core radius of a globular cluster contracts slowly with time. After several relaxation times, it reaches the core collapse stage where the core shrinks in size dramatically within a short time scale. The central stellar density becomes so high that the hard binaries, whose orbital velocities are much greater than the velocity dispersion of the host cluster (see Appendix A for discussions on hard binaries), can be formed through the dynamical processes. Those hard binaries can later provide heating energy to the cluster core by converting their binding energy to the kinetic energy of the incoming stars, which will prevent the core from further collapsing and eventually will make the core re-expand. The re-expansion will be halted when all the binaries are destroyed or have escaped. Then the core will undergo core collapse again. This core-collapse-and-re-expansion cycle is the core oscillation stage. There will be several such cycles at the core oscillation stage until the whole cluster is disrupted through evaporation process (i.e. high-speed stars escaping from the cluster).

One observational feature of the dynamical evolution is the collapsed cores of globular clusters through the surface brightness profile study. Newell & O'Neil (1978) gave the first observational evidence of a collapsed core in M15. Unlike other non-core-collapsed clusters, where the surface brightness profiles become flat towards the center, the core-collapsed cluster M15 shows a cusp feature (i.e. the surface brightness keep increasing toward the center, see Figure 1.1).

The median time scale for core collapse is short, about 2 Gyrs (Spitzer, 1987), comparing to the mean age of the Galactic globular clusters which is much greater than 5 Gyrs. This implies that the majority of the Galactic globular clusters today should have undergone core collapse. The survey of Galactic globular clusters by Djorgovski & King (1986), however, found only 21 out of 129 (or 16 %) globular clusters with collapsed cores. The more recent survey by Harris 1996 (2010 edition) shows a similar low fraction of the Galactic globular clusters with collapsed cores, 29 out of 157 (or 18 %). The contradictory of the core collapse time scale between

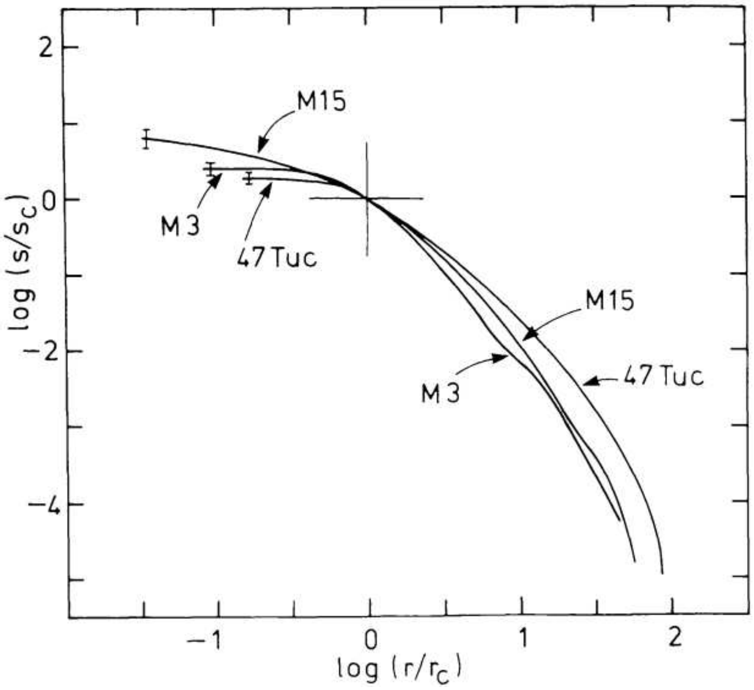

Figure 1.1: Comparisons of the surface brightness profiles for globular clusters (Newell & O'Neil, 1978). M15: core-collapsed cluster; M3 & 47 Tuc: normal clusters.

the theory and the observation raises the question whether the majority of globular clusters have undergone core collapse and now in the re-expanding phase (Goodman, 1984; Djorgovski & King, 1986; Elson et al., 1987), or they did not even have core collapse at all. Either way, there should be heating energy sources to re-expand the clusters, or to delay the clusters from core collapse.

There are mainly three ways to provide heating energy in the globular cluster cores: hard binaries, stellar mass loss, and intermediate-mass black holes. The binding energy of a hard binary can be released during interactions with other stars or binaries. The released energy can transfer to the incoming single star or the softer binary system, so as to heat up the stellar environment. The hard binary, on the other hand, will shrink in orbit and become harder, and eventually it will be destroyed or escape from the clusters (Heggie, 1975; Hut & Bahcall, 1983). The hard binaries can be formed dynamically during the late evolutional stage of a globular cluster, where the stellar density is so high that single stars can form hard binaries through dynamical interactions, such as quiescent low-mass X-ray binaries (qLMXBs), CVs, and millisecond pulsars (MSPs). The problem is, the observed number of those dynamically formed binaries is not enough to provide sufficient heating energy to the cluster cores (Goodman, 1987). The majority of hard binaries, however, might be formed primordially, i.e. they formed at the same time as other single stars in the host globular cluster (Goodman, 1987).

The stellar mass loss (in terms of stellar winds, planetary nebula, or supernova explosions) through the stellar evolution can diminish the mass of the cluster core, or decrease the potential energy of the cluster. The potential energy will decrease more than the kinetic energy of the system when reaching new equilibrium, making it an indirect heating source to the cluster (Hut et al., 1992a). The required stellar mass loss rate is $\sim 1\%$ of the total mass of the cluster for every relaxation time, which would be too bright for the core comparing to the observations (Goodman, 1984; Statler et al., 1987).

Intermediate-mass Black holes with mass less than 1000 $M_{\odot}$, can also provide an indirect heating source. They tend to capture passing-by stars, which makes those stars release part of their kinetic energy to the stellar environment. But the problem is how such intermediate-mass black holes formed in globular clusters or whether they exist at all (Goodman, 1984).

In summary, hard binaries are important in globular clusters, because they can provide heating energy to the cluster cores, and they can affect and accelerate the stellar evolution processes, so as to provide heating energy indirectly in terms of stellar mass loss. Early simple simulation shows that even a small fraction of primordial binaries can prevent globular clusters from core collapse for several relaxation times (Gao et al, 1991).

1.2 The Modern Simulations for the Globular Cluster Dynamical Evolution Including Binaries

Constructing a dynamical model of a globular cluster is not easy, as the total number ($10^5 \sim 10^6$) is too big for direct star-by-star tracking, and too small to use the mean field theory. Adding binaries in the model makes the simulation even more difficult. The time scale of a binary is from seconds to days comparing to the ages of a typical globular cluster (several Gyrs), and the distance is several AUs comparing to the size of a GC (tens of parsecs). Large magnitude span in both time and distance makes the simulation of the dynamical evolution for globular clusters really time expensive. This limited the early simulations to the size of several hundred stars to a few thousands (McMillan et al., 1990, 1991; McMillan & Hut, 1994), or similar to the open cluster condition, and only considered equal mass point stars (Gao et al, 1991; McMillan et al., 1990).

1.2.1 Monte-Carlo Simulations

The recent Monte-Carlo dynamical simulations of globular clusters are performed by Fregeau et al. (2003), who used a self-consistent two-dimensional Monte-Carlo simulation method, and assumed first only equal-mass binaries and later a mass-ratio range from 0 to 1 (Fregeau & Rasio, 2007). They included direct integration of binary scattering interactions (Fregeau & Rasio, 2007), and later also included single and binary stellar evolution codes SSE and BSE from Hurley et al. (2000), Hurley & Shara (2002), & Hurley et al. (2002) (Chatterjee et al., 2010). Ivanova et al. (2005) used a simplified model, considering stellar evolution with StarTrack (Belczynski et al., 2008), and the strong dynamical interactions of binaries are integrated numerically with Fewbody (Fregeau et al., 2004).

Their main results are in Figure 1.2 to 1.5. In Figure 1.2, the third part of the first plot shows the cluster size (in unit of the half-mass radius) versus time (in unit of the half-mass relaxation time). It is obvious that even with 2% binary fraction, it is sufficient to postpone the onset of core collapse for several relaxation times (22 t_{rh} with 2% binary fraction (solid line) VS. 10 t_{rh} without binaries (dashed line)). The second panel in this figure also shows the linear relationship between the core collapsed time (in unit of the core collapsed time without binaries) and the binary fractions. Note that, when the binary fraction is high enough, the globular cluster will be tidally disrupted even before reaching the core collapsed phase. The third plot in Figure 1.2 shows the binary fraction at different regions of the clusters evolving with time for different models. The binary fraction at the core region usually increases with time at the beginning due to mass segregation effect, where heavier stars (e.g. binaries) tend to sink to the core while lighter stars (e.g. single stars) tend to drift outwards, and decreases later due to the binary destructions and escaping. The binary fractions at outside region stay roughly the same over time.

In Figure 1.3, the ratio of the core to the half-mass radius is plotted against the binary fraction. At the low binary fraction region, the radius ratio increases, while at the high binary fraction region, the radius ratio decreases.

Figure 1.4 also shows the binary fraction evolution Vs. dynamical time by Ivanova et al. (2005). The core binary fraction increases from initial 0.2 to 0.35 at $4t_{rh}$ and decreases to 0.3 at $20t_{rh}$. The binary fraction at the outer region decreases from 0.2 to 0.08 at 20 t_{rh}.

Figure 1.5 shows the binary fractions vs. time at different regions (upper curve for core, lower curve for whole cluster) by Chatterjee et al. (2010). The core binary fraction increases with time till 16 Gyrs and decreases after that. The binary fractions outside the core radius generally stay unchanged over time.

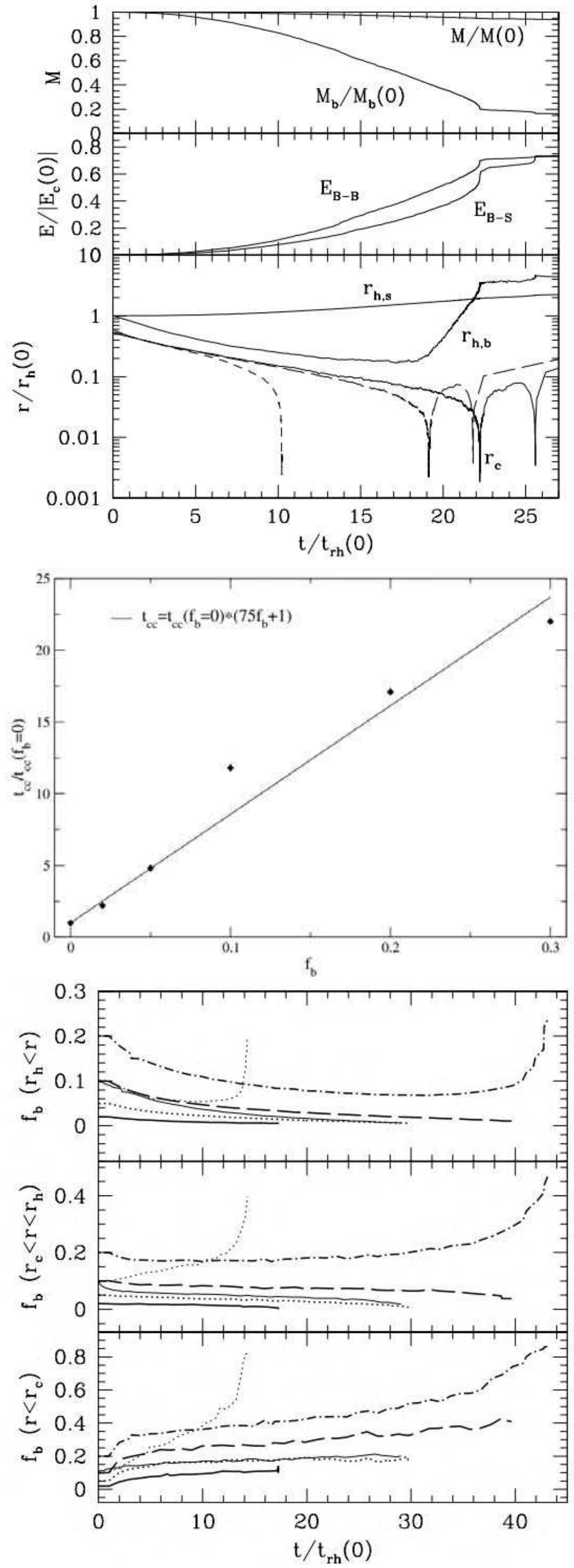

Figure 1.2: Monte-Carlo simulations by Fregeau et al. (2003). Upper panel: mass & core radius evolution with time; Middle panel: core collapse time in terms of the value without binaries Vs. binary fraction; Lower panel: binary fractions evolving with time at different regions.

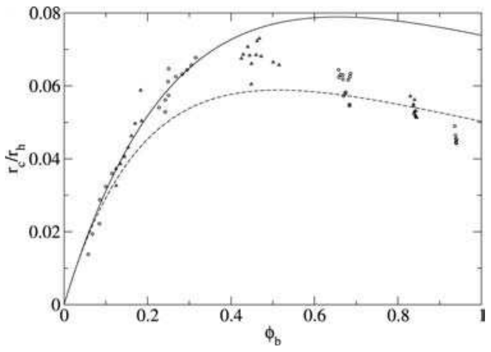

Figure 1.3: The ratios of the core to the half-mass radius Vs. binary fractions by Fregeau & Rasio (2007)

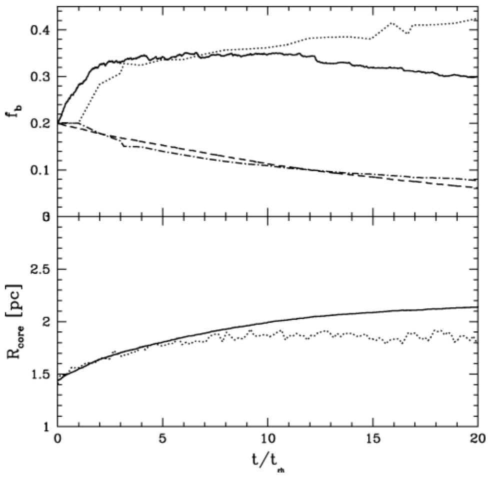

Figure 1.4: Binary fractions evolving with time by Ivanova et al. (2005), at core (upper solid curve) and whole cluster (lower long dashed curve).

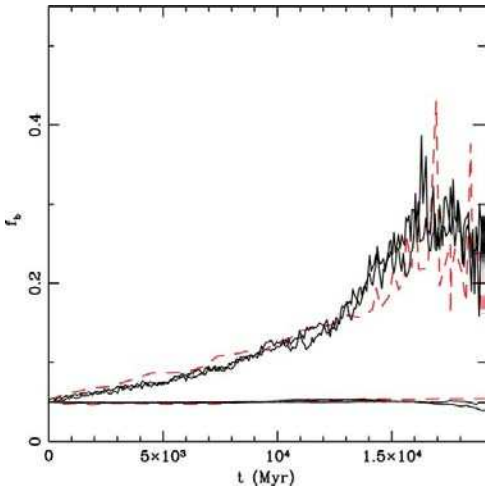

Figure 1.5: Binary fractions evolving with time by Chatterjee et al. (2010), at core (upper solid curve) and whole cluster (lower solid curve).

1.2.2 N-body Simulations

Hurley et al. (2007) performed the first realistic N-body simulations (n=100,000) of globular clusters including binaries in the range of 5% to 50%. Their results are similar to Figure 1.5, only that when binary fractions increase, there will be slightly deviations between different evolution curves (see Figure 1.6, first two rows). The lower two panels show the radial distribution of binary fractions, which decrease dramatically outwards to the half-mass radius, but stay unchanged beyond that.

Figure 1.7 gives an example of the dynamical model for NGC 6397 (Hurley et al., 2008), where the outer binary fraction (upper plot) remains unchanged over time while the core binary fraction (lower plot) increases against time. This gives us a way to measure the primordial binary fraction, i.e. only measuring the binary fraction outside the core.

1.2.3 Full Analytical Analysis

Sollima (2008) provides a full analytical method to construct the dynamical models of a globular cluster. Figure 1.8 shows the radial distribution of binary fractions at different ages and with different models. The decreasing feature of the binary fractions outwards is consistent with the N-body simulation by Hurley et al. (2007), suggesting that this radial distribution is the result of the dynamical mass segregation effect. The lower plots show the mass-ratio function evolution before and after the simulation.

1.2.4 Their Agreements and Divergences

There are some agreements and discrepancies between Monte Carlo simulations and N-body simulations. But one should realize that the core density and cluster mass are not the same, both of which affect the half-mass relaxation time and hence the mass segregation timescale, as well as the binary dynamical interaction rate. Fregeau et al. (2009) provides such comparison between Monte-Carlo and N-body simulations.

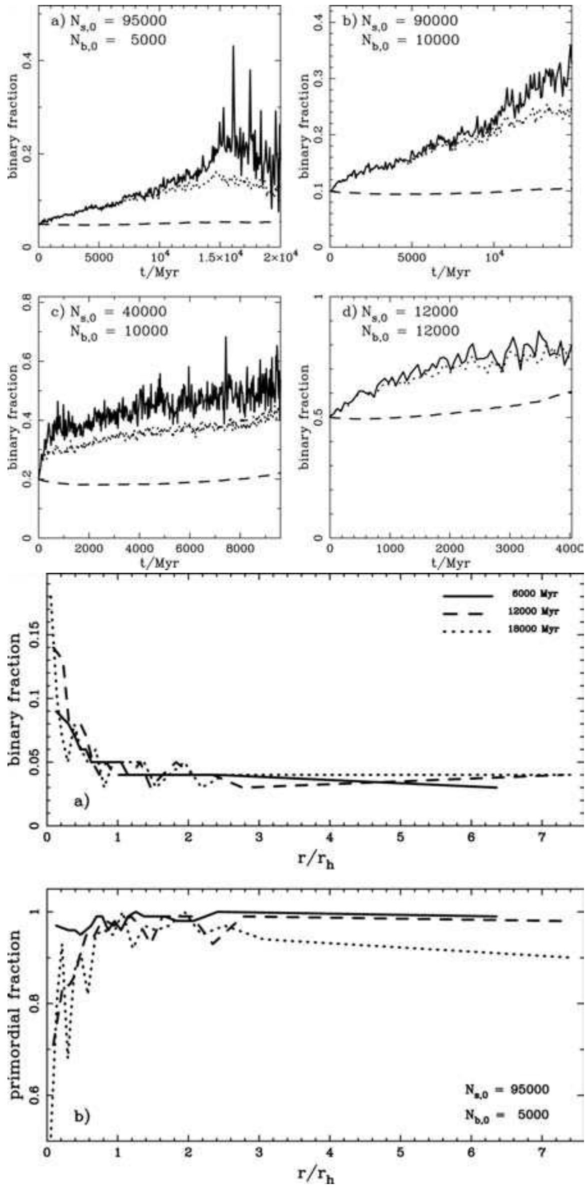

Figure 1.6: The N-body simulations by Hurley et al. (2007). Upper two rows: binary fractions evolving with time; Lower two rows: binary fractions radial distribution.

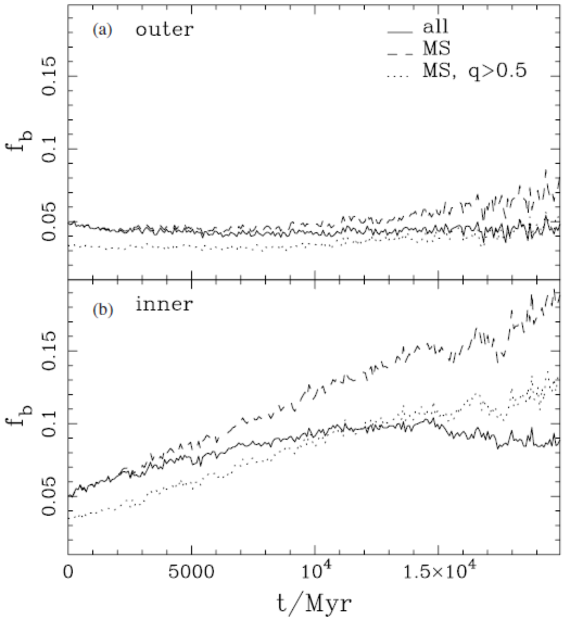

Figure 1.7: An example of N-body simulation for NGC 6397 by Hurley et al. (2008). Upper panel: outer binary fraction evolving with time; Lower panel: inner binary fraction evolving with time.

They found that the binary fraction increases in core with time (5% initial to 10% at present), dominated by mass segregation process. The overall binary fraction stays the same over time, due to the combination of stripping single stars from outskirts and binary disruptions. They also found that the observed MS-MS binaries only consist a small portion of the total true binaries (23% of all binaries at 14 Gyrs), while the majorities are in forms of MS-WD (44%) and WD-WD (32%) binaries.

The main agreements are that binaries can postpone core collapse, and globular clusters should show mass segregation features, such as the binary fractions radial distribution (see Figure 1.2, 1.6, and 1.8). The main disagreement is on whether the core binary fractions should increase with time (Fregeau et al., 2003; Hurley et al., 2007, 2008; Fregeau et al., 2009; Chatterjee et al., 2010) or decrease with time (Ivanova et al., 2005).

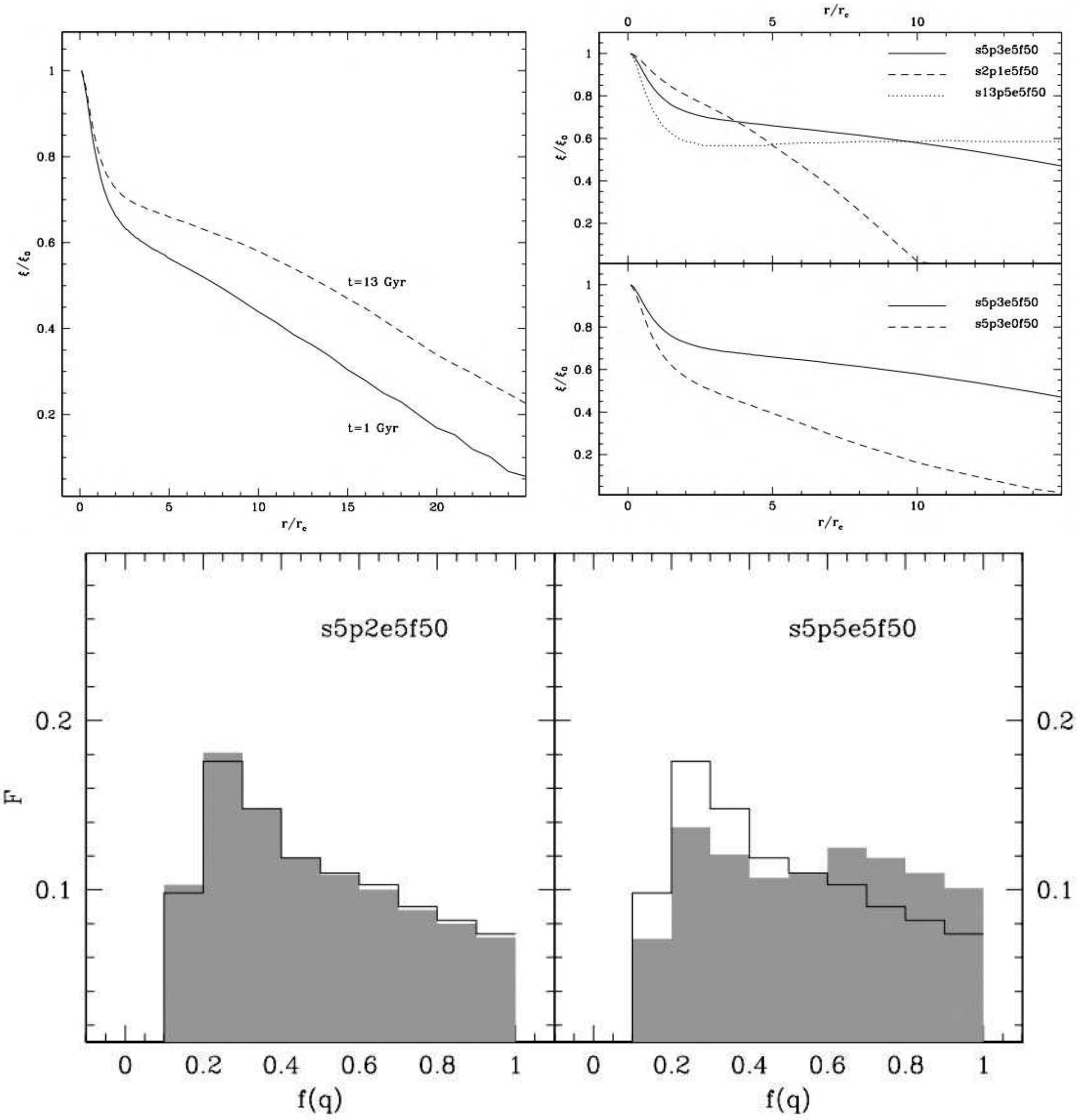

Figure 1.8: Binary radial distributions and mass-ratio distributions by Sollima (2008).

1.3 The Observations of the Globular Cluster Binaries

Although the theoretical models and simulations are well developed for the evolution of globular clusters with binary burning process, sufficient observations to test these models are lacking. One reason is that it is very difficult to isolate individual stars in the high density region such as the cores of globular clusters from the ground based telescope. The other reason is that photometry errors are very large due to superposition of those blending stars. These two difficulties make the determination of binaries fraction challenging.

1.3.1 X-ray Point Sources in Globular Clusters

Unlike the optical images of globular clusters, where hundreds of thousands of stars are observed in a small field, the X-ray images only show dozens of point sources (Figure 1.9). Those point sources can be categorized according to their X-ray luminosities (Heinke, 2011). The most luminous X-ray point sources in globular clusters are from the quiescent low-mass X-ray binaries (qLMXBs, a neutron star plus a donor at the low accreting state). The second luminous X-ray sources are CVs (a white dwarf plus a donor), followed by Chromospherically active binary stars (ABs, a main-sequence star plus a main-sequence/sub-giant star) and millisecond pulsars (MSPs, a recycled neutron star plus a donor). The qLMXBs, MSPs, and part of CVs are dynamically formed (Clark, 1975; Bailyn, 1995), as they are usually found in the dense core regions (Cohn et al., 2010) and their frequencies can be scaled by the closer encounter rates (Pooley et al., 2003; Pooley & Hut, 2006). ABs and part of CVs are thought to be primordial origin (Ivanova et al., 2006; Lu et al., 2011).

In summary, X-ray observations can be very effective to detect binaries in globular clusters, as those X-ray point sources are mainly binaries.

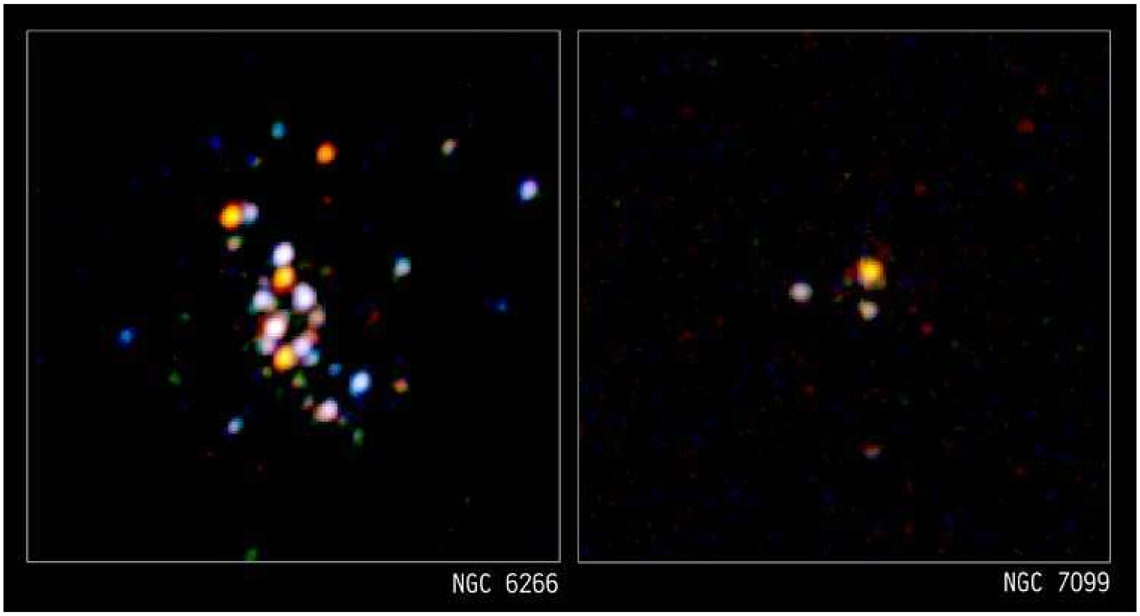

Figure 1.9: X-ray images for globular clusters (Credit:NASA/CXC/MIT/D.Pooley et al.). Left: NGC 6266; Right: NGC 7099.

1.3.2 Radial Velocity Variables

A direct method to detect binaries in globular clusters by optical observations is through the spectroscopic observation to measure radial velocity variations (see Figure 1.10 for example), which can only be applied to red giant and sub-giant stars. This is because those stars are bright in magnitude and cool in temperature, so there are many strong absorption lines for cross-correlation. This will improve the accuracy of radial velocity measurement to below 1 km/s. The drawback for this method is that it requires large amounts of observing time over several years, and the binary detecting rate is really low. Gunn & Griffin (1979) studied 111 giants in M3, with the accuracy of 1km/s, and none binaries were found. By improving the accuracy to 0.9 km/s, Pryor et al. (1988) only found 1 binary from those 111 giants in M3, suggesting very low efficiency in detecting binaries in GCs with radial velocity studies. Similarly, Yan & Cohen (1996) found 6 spectroscopic binaries in NGC 5053 by observing 77 giants and sub-giants. Cote & Ficher (1996) searched 33 turn-off dwarfs in M4, and inferred a 15 % of binary fraction. Cote et al. (1996) observed 109

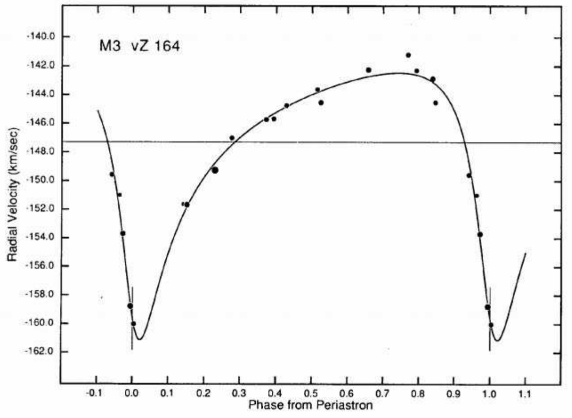

Figure 1.10: Radial velocity variable in M3 (Hut et al., 1992a). The fitted period is 2657^d, with a velocity amplitude of 9.3 km/s.

red giants in M22 with spectroscopy study, and found that only 1-3% of them are long period binaries.

For some long period binaries (greater than 10 years), even the current observational accuracy is not enough to discover the small radial velocity change over a reasonable time (5 years). For binaries composed of two main sequence stars, radial velocity observation present other challenges. Not only are these stars fainter than giants, but they have fewer lines for spectral cross-correlations, thereby demanding high S/N spectra that can place unreasonable demands on even the largest ground-based telescopes. Another issue with ground-based spectroscopic observations is that, even for good seeing conditions, multiple unrelated stars can fall in a single spectral PSF. This restricts such studies to the outer regions of globular clusters, which may not be representative of the dynamically more active inner parts.

1.3.3 Eclipsing Binaries

A different direct method for detecting binaries in GCs is through observation of eclipsing binaries. This method still needs a substantial amount of observing time investment to monitor many stars in globular clusters and search for the photometric variables through their light curves. While this method is biased by small orbital

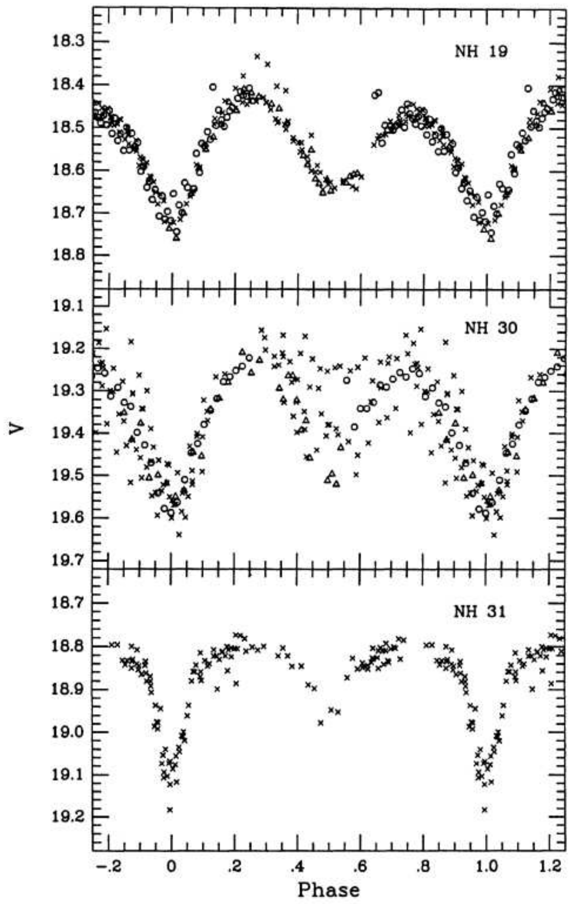

Figure 1.11: The light curves of three eclipsing binaries in NGC 5466 (Mateo et al., 1990).

inclination short period binaries, it is another valuable method for investigating binary systems. Mateo et al. (1990) detected three short-period eclipsing binaries in the blue stragglers in NGC5466 (see Figure 1.11). Yan & Mateo (1994) detected 5 short-period main-sequence eclipsing binaries in M71. And in M5 (=NGC5904), Yan & Reid (1996) found 6 short-period eclipsing binaries (1 blue straggler and 5 main sequence stars) outside 4 core radii.

1.3.4 Photometric Binaries from the Color-magnitude Diagrams

An indirect method, and the one used here, makes use of the accurate measurement of stars that form the main sequence in a color-magnitude diagram (CMD). For main sequence stars of a single age and metallicity, the width of the main sequence of single

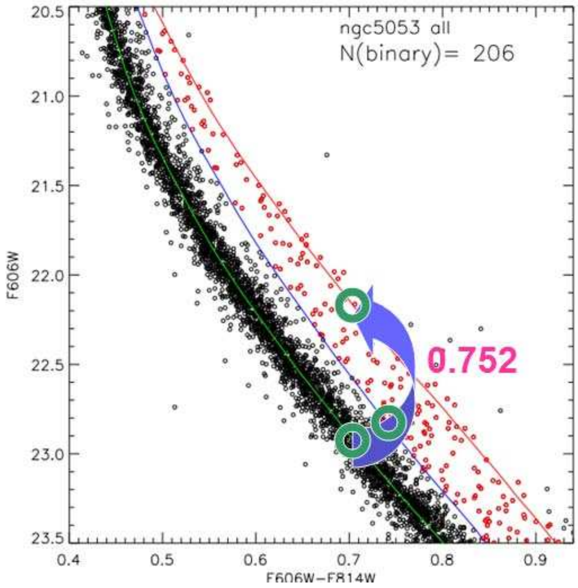

Figure 1.12: The photometric binaries from the CMD of NGC 5053. Black circles are main-sequence stars. The red circles are photometric binaries with mass-ratio greater than 0.5. The green, blue, and red curves are for binary populations with mass ratios equal 0, 0.5, and 1, respectively. The binaries follow the blue curved arrow from green curve to red curve with binary mass ratios from 0 to 1. The maximum up-shift in magnitude is 0.752 for equal-mass binaries.

stars should be limited only by measurement error. Relative to the single star main sequence, an unresolved binary star will be either redder, for a lower mass secondary, or brighter (by 0.75 mag) but at the same color for two stars of equal mass (see Figure 1.12). An ensemble of binaries forms a thickening to the red of the single star main sequence, which we can measure. This method is not biased on binary period distribution but on the binaries with mass ratios close to 1, and the binaries detected are mainly main-sequence-main-sequence ones. This method is very efficient in measuring the global binary fractions in globular clusters, as they only need one observation for images at two bands to construct the CMD.

The method is difficult to execute for the core regions for most clusters from the ground because of the precision required at faint magnitudes (S/N = 50-100 at V = 21) and in crowded fields. To date, only a few loose globular clusters have been studied for the binary fractions with ground-based telescopes at their outer regions.

Romani & Weinberg (1991) obtained a binary fraction of 9% within 10-30 core radii of NGC 6341 and 4% within 25-65 core radii for NGC 7099. Bolte (1992) measured a binary fraction of $> 10\%$ within 1-6 core radii for NGC 288. Clark et al. (2004) measured Palomar 13 and got the binary fraction of $(30 \pm 4)\%$ within 18 core radii.

The binary fractions at core regions, however, are the most sensitive parameter to the cluster dynamical time. Only the Hubble Space Telescope (HST) has sufficient sensitivity and spatial resolution to resolve even the core of globular clusters (see Figure 1.13). This greatly improves the photometric accuracy, and makes the measurement of binary fraction possible as a function of positions. This method can detect wide-separated binaries, but it is biased against binaries with low-mass secondaries. The benefit of this method is that, it requires relatively less observing time, and one can measure the global binary fraction without other assumptions. With HST, there are some studies with CMD method. Rubenstein & Bailyn (1997) measured that the binary fraction of NGC 6752 to be 15% - 38% in the inner core radius, and probably less than 16% beyond that. Bellazzini et al. (2002) also determined the binary fraction of NGC 288 within its half light radius to be $(15 \pm 5)\%$ with HST WFPC2 data, depending on the adopted binary mass ratio function. Its binary fraction outside the half light radius is less than 10%, and most likely closer to 0%. Richer et al. (2004) measured the evolved cluster M4 with proper-motion selected WFPC2 data. They found the binary fraction within 1.5 core radius is about 2%, decreasing to about 1% between 1.5 and 8.0 core radii. Zhao & Bailyn (2005) studied two clusters, M3 and M13, with WFPC2 data, and they found that the binary fraction of M3 within one core radius lies between 6% and 22%, and falls to 1% - 3% between 1-2 core radii. In M13, it was not possible to measure its binary fraction using their data, because the observed spread of the main-sequence is larger than the artificial star test, implying an intrinsic metallicity dispersion for M13. Davis et al. (2008) measured the binary fraction of the core collapsed cluster NGC 6397 with both ACS

Figure 1.13: Comparisons of images of 47 Tuc between VLT (left) and HST (right). Credit: (left) VLT/ESO/R. Kotak and H. Boffin; (right) NASA/ESA/G. Meylan

and WFPC2 data. They well constrained the binary fraction outside the half light radius to be $(1.2 \pm 0.4)\%$ with 126 orbits of observation with ACS and proper-motion selected clean data, and constrained the binary fraction within the half light radius to be $(5 \pm 1)\%$ with WFPC2 data.

Sollima et al. (2007) performed the first sample study for the binary fractions in globular clusters. They used aperture photometry to construct the CMDs for 13 low-density, high galactic latitude globular clusters with ACS data. They found a minimum of 6% binary fraction within one core radius for all clusters in their sample, and global fractions ranging from 10 to 50 per cent depending on the clusters and the assumed binary mass-ratio model.

Although the HST data become mature, systematical analysis of binary fractions and the direct comparison to theoretical predictions are still lacking, which is the motivation of this thesis work.

1.4 Outline of this Thesis Work

In this thesis, I compiled a sample of 35 Galactic globular clusters, a larger sample than previous efforts, and one that takes advantage of the wealth of the archived HST data. Chapter 2 will be focused on the methodology, including data analysis process, three different methods to measure the binary fractions, and the technical discussions. Chapter 3 will present the results, which include binary fractions within the core, the half-mass radius, and the whole field of view regions. Results of the correlation analysis between binary fractions and the clusters properties, such as ages, [Fe/H], Mv, and radius, will also present in Chapter 3, as well as the high mass-ratio binary candidate catalog and their properties. Chapter 4 will present the summary of this thesis and give suggestion for future work.

The major questions that this thesis work need to answer are 1) how the binary fractions, within the core and at outer region, evolve with time? 2) What are the binary fraction radial distributions in globular clusters? 3) Can we see any mass segregation effect in globular clusters? 4) How the observation results are comparing to the theoretical simulation predictions?

CHAPTER 2

HST Observations of Globular Cluster Binaries: Methodology

2.1 Sample Selection

To achieve the primary goal of determining the binary fraction, we need accurate color-magnitude diagrams (CMD). CMDs can be made from several different filters, such as a subset of B, V, R, and I, although for the main sequence in the late G to early M spectral region, the most accurate CMDs are composed from a subset of V, R, and I (V and I to be used when possible).

For good photometric errors (0.02 mag rms), about 6,000 stars on the CMD will yield an uncertainty in the binary fraction of 1.5-2% (after Hut et al. (1992a), Table 4). This type of photometric accuracy is achieved with WFPC2 V band images in 1500 seconds for V = 24.0 (m-M = 14.6 mag for a M1 star), or for V = 24.9 when using the ASC/WFC (m-M = 15.5 mag for a M1 star).

We examined the HST observations taken for every Galactic globular cluster in the list of Harris 1996 (2010 edition) and most have some WFPC2 or ACS observations, but many of these were taken in snapshot mode and are not sufficiently long to meet our criteria. We find about 35 globular clusters that are sufficiently luminous, and with long enough exposures that we can extract useful information on binary fractions. Most of those data sets are from the HST Treasury program for globular clusters with ACS observations in F606W and F814W filters (Sarajedini et al., 2007).

Table 2.1 shows the basic information for each cluster in this sample, including Galactic longitude (l), Galactic latitude (b), metallicity ([Fe/H]), foreground reddening E(B-V), absolute visual magnitude M_V, collapsed core (y/n), core radius (r_c), half light radius (r_h), log relaxation time at half mass radius ($\log t_{rh}$), age (t_9), and dynamical age (t_9/t_{rh}). The dynamical ages in this sample range from dynamical young clusters ($t_9/t_{rh} = 1.5$) to dynamical old one ($t_9/t_{rh} = 46.4$)(see upper right panel in Figure 2.1). The metallicities in this sample range from metal poor cluster ($[Fe/H] = -2.37$) to metal rich one ($[Fe/H] = -0.32$)(see Figure 2.1, lower left panel). Figure 2.1 lower right panel shows the distribution of those clusters relative to the Galactic disk plane, among which 9 clusters are within the ±15° Galactic latitudes, and are potentially affected by non-member stars.

Table 2.2 shows the HST ACS observation log for each cluster, including filter type, number of exposures used, exposure time per frame, and data set ID. We only used the long exposure frames here and did not include those short exposure frames, because we are only interested in the CMDs below the turn-off point.

2.2 Data Reduction and Photometry

We retrieved the HST ACS archival data on F606W and F814W bands for each cluster in our sample through the STSci, which have been calibrated with the most recent calibration frames on the fly. For each filter, all *FLT* images were drizzled to the same reference frame to measure any residual relative shifts among frames using *Multidrizzle*. This step is necessary as it can 1) provide better image alignments than the default pipeline; 2) and correct the default masks used to mask out good pixels due to inaccurate alignments for the calibration pipeline, which helps to recover more faint stars. A clean and deep drizzled image was generated as the reference frame,

Table 2.1: Basic properties of the Galactic globular clusters in the sample[a]

Object	l °	b °	[Fe/H]	E(B-V)	M_V	core collapse	r_c ′	r_h ′	log t_{rh}	t_9[b] Gyr	t_9/t_{rh}
NGC 104	305.89	-44.89	-0.72	0.04	-9.42		0.36	3.17	9.55	10.7	3.0
NGC 288	152.30	-89.38	-1.32	0.03	-6.75		1.35	2.23	9.32	11.3	5.4
NGC 362	301.53	-46.25	-1.26	0.05	-8.43	y	0.18	0.82	8.93	8.7	10.2
NGC 1851	244.51	-35.03	-1.18	0.02	-8.33		0.09	0.51	8.82	9.2	13.9
NGC 2808	282.19	-11.25	-1.14	0.22	-9.39		0.25	0.80	9.15	9.3	6.6
NGC 4590	299.63	36.05	-2.23	0.05	-7.37		0.58	1.51	9.27	11.2	6.0
NGC 5053	335.70	78.95	-2.27	0.01	-6.76		2.08	2.61	9.87	10.8	1.5
M 3	42.22	78.71	-1.50	0.01	-8.88		0.37	2.31	9.79	11.3	1.8
NGC 5466	42.15	73.59	-1.98	0.00	-6.98		1.43	2.30	9.76	12.2	2.1
NGC 5897	342.95	30.29	-1.90	0.09	-7.23		1.40	2.06	9.57	12.3	3.3
NGC 5904	3.86	46.80	-1.29	0.03	-8.81		0.44	1.77	9.41	10.9	4.2
NGC 5927	326.60	4.86	-0.49	0.45	-7.81		0.42	1.10	8.94	10.9[c]	12.5
NGC 6093	352.67	19.46	-1.75	0.18	-8.23		0.15	0.61	8.80	12.4	19.7
NGC 6121	350.97	15.97	-1.16	0.35	-7.19		1.16	4.33	8.93	11.7	13.7
NGC 6101	317.74	-15.82	-1.98	0.05	-6.94		0.97	1.05	9.22	10.7	6.4
M 13	59.01	40.91	-1.53	0.02	-8.55		0.62	1.69	9.30	11.9	6.0
NGC 6218	15.72	26.31	-1.37	0.19	-7.31		0.79	1.77	8.87	12.5	16.9
NGC 6341	68.34	34.86	-2.31	0.02	-8.21		0.26	1.02	9.02	12.3	11.7
NGC 6352	341.42	-7.17	-0.64	0.22	-6.47		0.83	2.05	8.92	9.9	11.9
NGC 6362	325.55	-17.57	-0.99	0.09	-6.95		1.13	2.05	9.20	11.0	6.9
NGC 6397	338.17	-11.96	-2.02	0.18	-6.64	y	0.05	2.90	8.60	12.1	30.4
NGC 6541	349.29	-11.19	-1.81	0.14	-8.52	y	0.18	1.06	9.03	14.0[d]	13.1
NGC 6624	2.79	-7.91	-0.44	0.28	-7.49	y	0.06	0.82	8.71	10.6	20.7
NGC 6637	1.72	-10.27	-0.64	0.18	-7.64		0.33	0.84	8.82	10.6	16.0
NGC 6652	1.53	-11.38	-0.81	0.09	-6.66		0.10	0.48	8.39	11.4	46.4
NGC 6656	9.89	-7.55	-1.70	0.34	-8.50		1.33	3.36	9.23	12.3	7.2
NGC 6723	0.07	-17.30	-1.10	0.05	-7.83	y	0.83	1.53	9.24	11.6	6.7
NGC 6752	336.49	-25.63	-1.54	0.04	-7.73	y	0.17	1.91	8.87	12.2	16.5
Terzan 7	3.39	-20.07	-0.32	0.07	-5.01		0.49	0.77	8.96	7.4	8.1
Arp 2	8.55	-20.79	-1.75	0.10	-5.29		1.19	1.77	9.70	11.3	2.3
NGC 6809	8.79	-23.27	-1.94	0.08	-7.57		1.80	2.83	9.29	12.3	6.3
NGC 6981	35.16	-32.68	-1.42	0.05	-7.04		0.46	0.93	9.23	9.5[e]	5.6
NGC 7078	65.01	-27.31	-2.37	0.10	-9.19	y	0.14	1.00	9.32	11.7	5.6
NGC 7099	27.18	-46.84	-2.27	0.03	-7.45	y	0.06	1.03	8.88	11.9	15.7
Palomar 12	30.51	-47.68	-0.85	0.02	-4.47		0.02	1.72	9.28	6.4	3.4

[a] all columns except ages t_9 are from Harris 1996 (2010 edition).

[b] ages t_9 are from Salaris & Weiss (2002) except [c] from Fullton et al. (1996), [d] from Alonso-Garcia (2010), and [e] from Sollima et al. (2007).

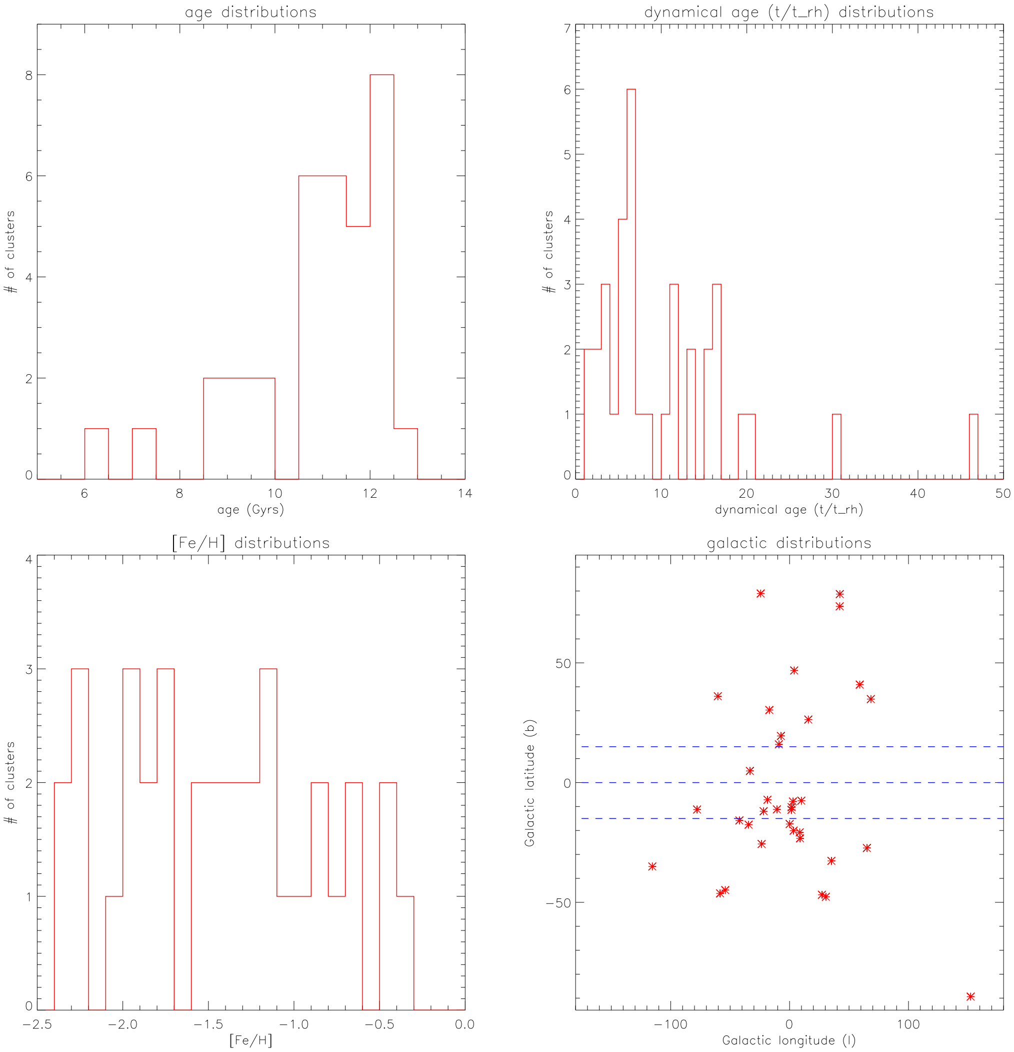

Figure 2.1: Distributions of properties for each globular clusters in the sample. Upper left: ages distribution. Upper right: dynamical ages distribution. Lower left: [Fe/H] distribution. Lower right: galactic position distribution.

Table 2.2: HST ACS observation log

Name	Filter	# of Exposures	Exposure Time (s)	Dataset
NGC 104	F606W	4	50	J9L960010
	F814W	4	50	J9L960020
NGC 288	F606W	4	130	J9L9AD010
	F814W	4	150	J9L9AD020
NGC 362	F606W	4	150	J9L930010
	F814W	4	170	J9L930020
NGC 1851	F606W	5	350	J9L910010
	F814W	5	350	J9L910020
NGC 2808	F606W	5	360	J9L947010
	F814W	5	370	J9L947020
NGC 4590	F606W	4	130	J9L932010
	F814W	4	150	J9L932020
NGC 5053	F606W	5	340	J9L902010
	F814W	5	350	J9L902020
M 3	F606W	4	130	J9L953010
	F814W	4	150	J9L953020
NGC 5466	F606W	5	340	J9L903010
	F814W	5	350	J9L903020
NGC 5897	F606W	4	340	J9L913010
	F814W	3	350	J9L913020
NGC 5904	F606W	4	140	J9L956010
	F814W	4	140	J9L956020
NGC 5927	F606W	5	350	J9L914010
	F814W	5	360	J9L914020
NGC 6093	F606W	5	340	J9L916010
	F814W	5	340	J9L916020
NGC 6101	F606W	5	370	J9L917010
	F814W	5	380	J9L917020
NGC 6121	F606W	4	25	J9L964010
	F814W	4	30	J9L964020
M 13	F606W	4	140	J9L957010
	F814W	4	140	J9L957020
NGC 6218	F606W	4	90	J9L944010
	F814W	4	90	J9L944020
NGC 6341	F606W	4	140	J9L958010
	F814W	4	150	J9L958020
NGC 6352	F606W	4	140	J9L959010
	F814W	4	150	J9L959020

continued on next page

continued from previous page

Name	Filter	# of Exposures	Exposure Time (s)	Dataset
NGC 6362	F606W	4	130	J9L934010
	F814W	4	150	J9L934020
NGC 6397	F606W	4	15	J9L965010
	F814W	4	15	J9L965020
NGC 6541	F606W	4	140	J9L936010
	F814W	4	150	J9L936020
NGC 6624	F606W	5	350	J9L922010
	F814W	5	350	J9L922020
NGC 6637	F606W	5	340	J9L937010
	F814W	5	340	J9L937020
NGC 6652	F606W	5	340	J9L938010
	F814W	5	340	J9L938020
NGC 6656	F606W	4	55	J9L948010
	F814W	4	65	J9L948020
NGC 6723	F606W	4	140	J9L941010
	F814W	4	150	J9L941020
NGC 6752	F606W	4	35	J9L966010
	F814W	4	40	J9L966020
NGC 6809	F606W	4	70	J9L963010
	F814W	4	80	J9L963020
NGC 6981	F606W	4	130	J9L942010
	F814W	4	150	J9L942020
NGC 7078	F606W	4	130	J9L954010
	F814W	4	150	J9L954020
NGC 7099	F606W	4	140	J9L955010
	F814W	4	140	J9L955020
Arp2	F606W	5	345	J9L925010
	F814W	5	345	J9L925020
Parlomar 12	F606W	5	340	J9L928010
	F814W	5	340	J9L928020
Terzan 7	F606W	5	345	J9L924010
	F814W	5	345	J9L924020

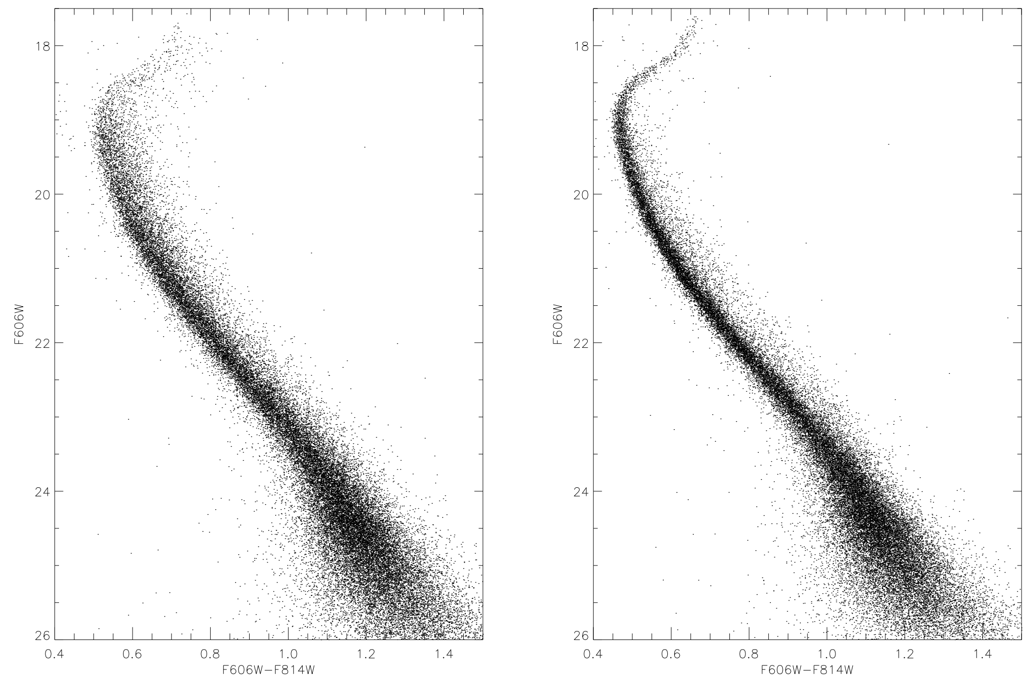

Figure 2.2: Comparisons of the quality of the CMDs for NGC 4590 between different version of Dolphot, V1.0 (left), V1.2 (right). The latter version shows significant improvement on the accuracy of the stars near turn-off point, and shows narrower spread on the main-sequence.

and all the accurate masks in *FLT* images were updated.

We then performed photometry with Dolphot (V1.2, Dolphin 2000), which is an automated CCD photometry package for general use and for HST data (ACS, WFPC2, and WPC3) with specially designed modules (ACS module (V1.2) here). We found significant improvement in the quality of PSF photometry for Dolphot V1.2 from V1.0. This can be found in Figure 2.2, where the CMD for NGC 4590 near the turn-off point is well-defined and the main sequence is narrower by Dolphot V1.2 (right panel) comparing to Dolphot V1.0 (left panel).

We prepared the *FLT* images with the following steps for later Dolphot usage. First, bad pixels were masked out and pixel areas were multiplied to all the *FLT* images with the *acsmask* command, and only the SCI frames were stored for further usage to save disk space. Second, all the *FLT* images were split into two chips with the *splitgroups* command. Third, sky maps were calculated for each chip with the *calcsky* command.

To perform photometry on individual *FLT* frames simultaneously while using the drizzled frame as the reference image, Dolphot requires alignment estimates relative to the reference frame for individual image. Thus we determined the RA and DEC of the center of each chip of the *FLT* image, found the pixel coordinates of that RA and DEC in the reference image, subtracted from the pixel coordinates of the center of the reference image, and input those as the initial image alignments for Dolphot. An alternative way to measure the initial alignments is to construct a star list with at least 3 stars per chip using *ds9* or *IRAF*. Each star entry has pixel coordinates in both the target and reference images. Then using the command *acsfitdistort*, we can obtain the initial alignments for each chip. This initial guess alignments are good enough, as Dolphot will further fine-tune the image alignments to the accuracy of 0.1 pixel within a two-pixel range.

We adopted the recommended parameter values in the input parameter file according to the Dolphot ACS manual, and performed PSF-fitting photometry. From the output photometry files, the error weighted average magnitudes for both the F814W and the F606W filters were used. Note that the magnitudes used here are instrumental ones with zero point set to VEGA system. To select good stars from artifacts (e.g. spikes around bright stars) and residual cosmic rays, we adopted the criteria as follows: $|sharpness| \leq 0.1$, $crowding \leq 0.5$, $object\ type \leq 2$, and each good star should be detected in at least two frames for each filter (i.e. $error\ flag < 8$ for each frame indicates a good detection). In practice, we chose stars one magnitude below the turn-off point, since close to the turn-off point, binary sequences turn to merge with the main sequence and lose all the binary information. We also discarded stars more than four magnitudes below the turn-off point, because stars near the detection threshold do not play an important role due to large photometric spread from the main-sequence stars. Figure 2.3 gives an example of the CMD from the PSF-fitting photometry. The red dashed lines indicate the portion of CMD we used during the analysis. Other lines will be discussed later.

2.3 The Artificial Star Tests

Without knowing the photometric errors, completeness, and the rate of superposition of stars, we cannot have accurate measurement of binary fractions from the CMD. The artificial star tests, however, can help us understand the photometric errors and accuracy, as well as completeness (or star recovery percentage) at different region of clusters and at different magnitudes. It can also simulate the rate of superposition of stars if performed properly.

2.3.1 Defining the Main-sequence Ridge Line

To perform artificial star tests and later CMD analysis, we need to define the main-sequence ridge line (MSRL) of the observed CMD first. We constructed the MSRL from the data instead of fitting theoretical isochrones to the CMD, as the latter method is not sufficiently accurate to define the ridge line. To define the MSRL from the CMD, we used a moving box method. In each step, we defined a box with a height of 0.1 magnitude in the F606W axis, and a width of all range in the color (F606W-F814W) axis. Then we searched the peak value of the color histograms in that box with a color bin-size of 0.0015 magnitude. The color value at the peak and the middle point of the box in the F606W axis direction are the defined MSRL for stars in that box. Next, the box was moved down 0.01 magnitude along the F606W axis, and we repeated the process above until all the observed magnitudes were measured. The result line was then smoothed with the moving average method with a period of 50. In Figure 2.3, the green line is the defined MSRL.

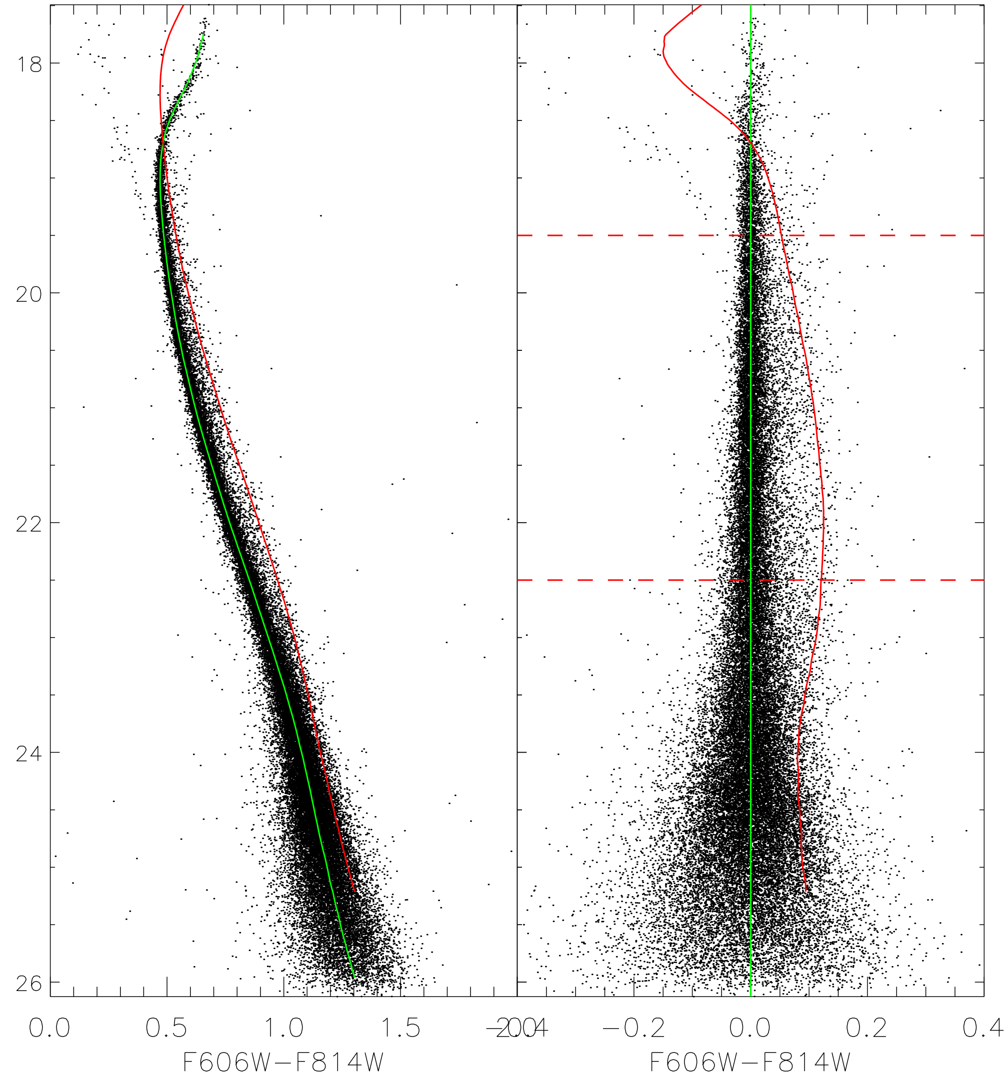

Figure 2.3: An example of the observed CMD (left) and the straightened CMD (right) for NGC 4590. The solid green line is the defined MSRL. The solid red line is the equal-mass binary population. Binary fraction is estimated within the range of the dashed red lines.

2.3.2 Performing the Artificial Star Tests

With the defined MSRL, we can perform the artificial star tests in Dolphot, with the parameter *FakeStars* set to a fake star list, which were generated by our own IDL routine. The F606W magnitudes of those fake stars were randomly generated while the F814W magnitudes were derived from the MSRL, so that all those fake stars are on the MSRL. The (X, Y) coordinates of those fake stars were randomly chosen from the area of the drizzled reference frame, but were not at the empty non-data CCD area. Each fake star in this list was added to each *FLT* frame one at a time, and was recovered using the same photometry process by Dolphot. Subsequently, all *FLT* frames were restored to original states and the next fake star was added. These processes were repeated until all the fake stars were added and recovered. The final photometric output file was screened using the same criteria as the observed one to select good fake stars. This method, which we added only one fake star at a time, does not introduce extra blending errors for those added fake stars, and one can generate as many of fake stars as needed. In practice, we added 100,000 fake stars for each image. Figure 2.4 shows two examples of the artificial star tests, NGC 5053 (low stellar density cluster) and NGC 1851 (high stellar density cluster). The green line is the input fake stars (total of 100,000 stars for each cluster), which are all on the MSRL. The scattered black dots are the recovered fake stars (69,995 stars for NGC 5053 and 52,205 stars for NGC 1851).

2.3.3 Photometric Accuracy, Uncertainty, and Completeness

After we have the input and recovered fake star lists, we can study the photometric accuracy and uncertainty. Here, we compared the photometry for two clusters, NGC 5053 (low stellar density cluster) and NGC 1851 (high stellar density cluster). Their HST ACS observations are very similar in exposure times: NGC 5053 (F606W: 340s*5, F814W: 350s*5) and NGC 1851 (F606W: 350s*5, F814W: 350s*5).

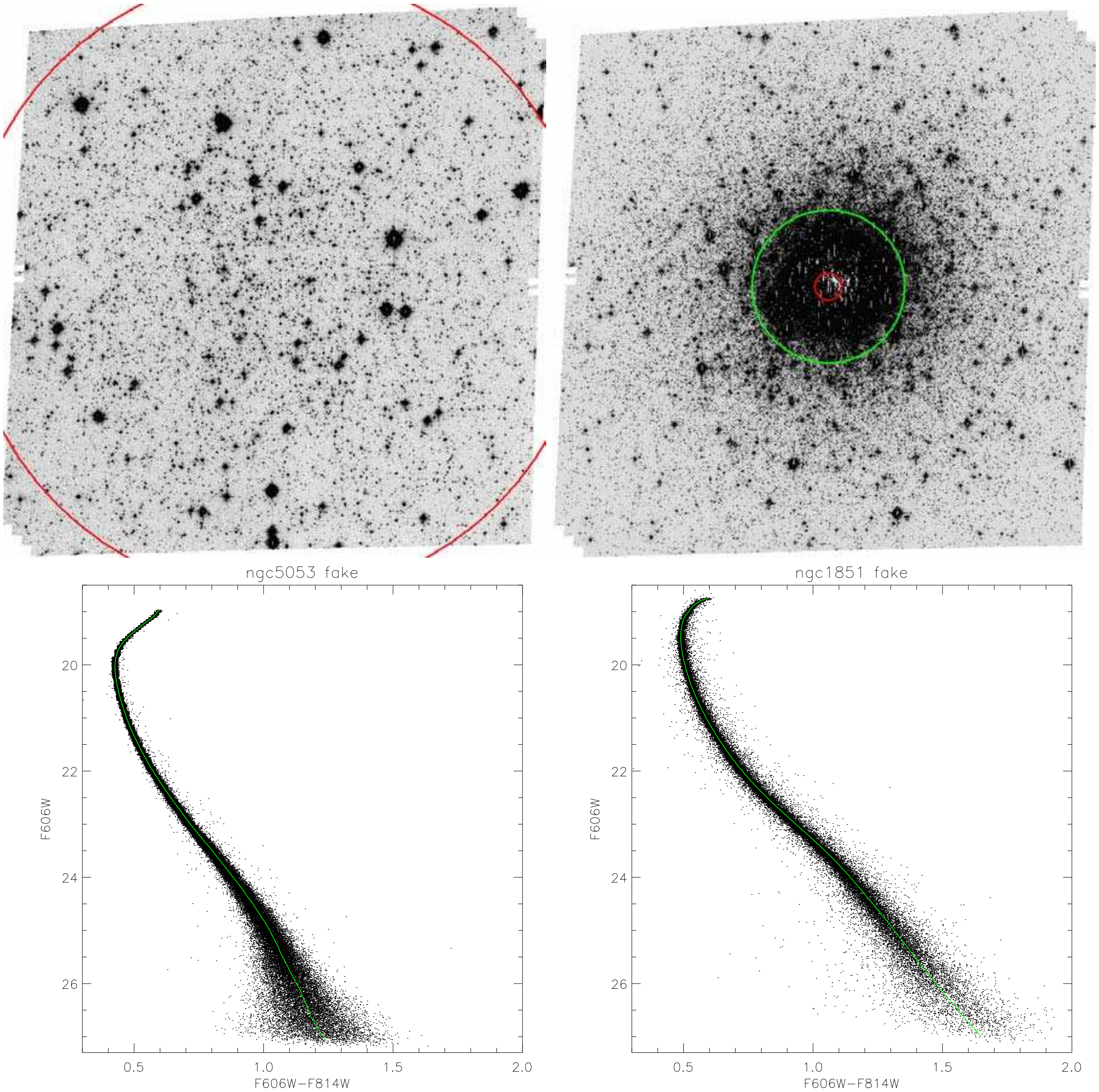

Figure 2.4: Two examples of artificial star tests. Left column: low stellar density cluster NGC 5053. Right column: high stellar density cluster NGC 1851. Upper panel: the observed ACS images for these two clusters. The red circle represents core region while the green one is for half light region. Lower panel: the input fake stars (green lines) and the recovered fake stars (black dots) on CMDs.

In Figure 2.5, we plot the magnitude differences for input and recovered stars for F606W filter (1st row) and F814W filter (2nd row). These plots indicate photometric discrepancies, and all of them showing differences within ±0.2 magnitudes. Note from the plots that at fainter magnitudes, the magnitudes of the recovered stars tend to be fainter than the input ones. Row 3 and 4 in Figure 2.5 show the photometric uncertainties for F606W and F814W filters, respectively. Row 5 in Figure 2.5 shows the uncertainties in color (F606W-F814W), which are calculated by square root of sum of squares for the uncertainties of the magnitudes at F606W and F814W bands. These uncertainties are the photometric spreads of the main-sequence stars on the CMDs. From those plots we can see that most stars in NGC 1851 has similar photometric accuracy and uncertainties as that in NGC 5053, only that in NGC 1851 there are more stars with large errors scattering around, even for bright stars.

Row 6 in Figure 2.5 shows the completeness curve (or star recovery percentage), which is calculated by dividing the total number of recovered stars (N(out)) at certain magnitude interval by the total number of input stars (N(In)) at the same magnitude interval. The completeness curve for NGC 5053 is quite flat down to the 26.5 magnitude, indicating even star recovery percentage down to very faint magnitude. For NGC 1851, however, the star recovery percentage is not even, with relatively higher recovery percentage towards brighter stars than the fainter ones. This can be seen from the fake CMDs in Figure 2.4, where there are fewer faint stars in NGC 1851 than in NGC 5053, even though they have similar exposure times. This indicates that faint stars are hard to recover in dense stellar region due to high and un-uniform background lights.

2.4 The High Mass-ratio Binary Fraction

Binary fraction with high mass-ratio close to 1 is relatively easy to measure using CMDs. Those binaries have relatively large distances to the main-sequence stars,

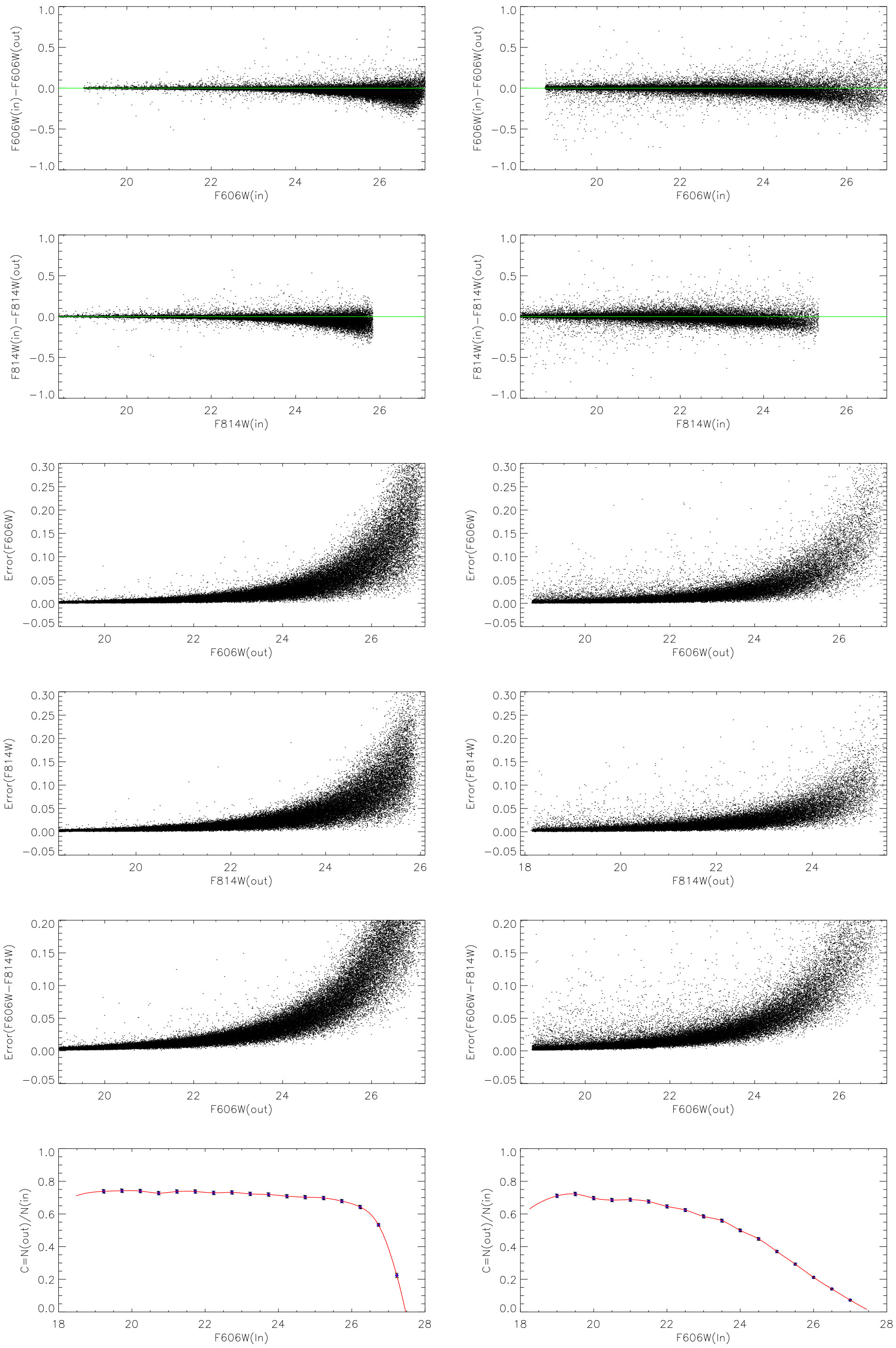

Figure 2.5: Examples of the results for the artificial star tests: NGC 5053 (left column) and NGC 1851 (right column). Row 1 & 2: differences of the input and recovered magnitudes for filter F606W and F814W. Row 3 & 4: magnitude uncertainties for filter F606W and F814W. Row 5: color uncertainties. Row 6: completeness curve.

and are usually beyond at least 3 σ of the photometric errors from the main sequence stars. This can be seen from the straightened CMD (i.e. the CMD subtracted the color of the MSRL), where the binaries distribute on the right side and with certain distance to the main sequence below the turn-off point (Figure 2.6). The maximum distance is from equal-mass binaries, and this distance varies with the shape of the MSRL (the green line in Figure 2.6). The minimum distance is for binaries with mass-ratio close to 0, and they are undistinguished from those main-sequence stars (the blue solid line in Figure 2.6). When the photometric errors get larger, the main-sequence stars will eventually spread to the equal-mass binary region, smearing out all the binary signals (see Figure 2.6, right panel for example). But as long as the photometry for the CMD is good enough, the main sequence will be tight and high mass-ratio binaries will be distinguishable from main-sequence stars (such as stars in the region B of Figure 2.6). There are two other contaminations, however, beside photometric errors: superposition of stars and field stars.

2.4.1 The Model for the Superposition of Stars

The superposition of stars in a star cluster occurs when the cluster is projected from 3D to 2D. Two stars (or more) in the line of sight and within the minimum angular resolution will be measured as one star (or a blend). They are not physically bound binaries, but have exactly the same effect on CMD as those real ones. It is very difficult to screen blending stars, but statistically, we can simulate their distribution through Monte-Carlo simulations. In Appendix B, we discussed the blending fraction in terms of Poisson function and tested it with Monte-Carlo simulations. The blending fraction is proportional to the radial stellar number density of a cluster, decreasing from the core to outside region. The general way to measure blending fraction is through artificial star tests, in which fake stars from MSRL are added to real images and are recovered with the same photometric processes as real stars. Any fake stars overlapping with real stars will represent a blending source, and the recovered magnitudes will be the sum of them. As long as the added fake stars follow the radial light distribution of a globular cluster, it then represents the similar blending fraction as that cluster. The drawback for this method is that it is really time-consuming. A 100,000 star run will take more than 24 hours. In practice, we used the following method to save the simulation time, which uses the real star map instead of images to avoid large amount of photometric time.

In each simulation, we added fake stars to the real star map, and the fake stars have the same luminosity function and light distribution as the real ones, so it should have a similar blending fraction as the observed one. To generate the fake star list, we chose fake stars with their V magnitudes sampled by the observed luminosity function, and their I magnitudes calculated from the MSRL, i.e. all the fake stars are on the MSRL and have the same luminosity function as the real stars. The number of total fake stars added is equal to that of the total observed stars to produce similar condition. Each fake star was assigned a radius r to the center of the cluster, which was sampled by the radial light distribution of real stars, so that the radial light distribution of fake stars is similar to the real ones. Then the azimuth angle is randomly assigned to the fake star to calculate the coordinates (x,y). To that position (x,y), any real star with distance less than 1 resolution element (the minimum resolution size Dolphot used) will be considered as a blended star, and the total magnitude will be added. To find those blended stars, we used our IDL routine with K-D tree algorithm by comparing lists of the observed stars and fake stars. Those blended sources were then added photometric errors from the observed stars (see Figure 2.5). We repeated this simulation 30 times to obtain an average number or an average residual color distribution (used later) of blending stars, which took less than 1 minute in most cases.

2.4.2 The Model for the Field Star Population

Field stars, both faint foreground stars and bright background stars, can also contaminate the binary population on CMDs and thus affect the accuracy of the measurement of the binary fraction, especially for low Galactic latitude clusters. They affect the number of binaries in the binary region on CMD, as well as the number of single stars on main-sequence. High galactic latitude clusters do not have many field stars contaminated. NGC 4590 ($b = 36.05°$), for example, only has 24 field stars (simulated from the model of Robin et al. (2003)) in the ACS field of view, or 0.06% of the total observed stars in that field. Low Galactic latitude clusters, however, have many contaminations from field stars. NGC 6624 ($b = -7.91°$), for example, has 51,325 field stars in the ACS field of view, which is about 50% of the total observed stars in that field. The best way to select cluster members is by proper motion, which, however, requires at least two epochs HST observations separated by years. An alternative way is to construct the field star model from the theoretical model of the Galaxy to statistically account for those field stars. We used the Stellar population Synthesis model of the Galaxy (Robin et al., 2003) to simulate field stars at the cluster position, with the size of ACS CCD chips, $202'$ by $202'$. The V and I Johnson-Cousin magnitudes of the generated field stars are corrected the reddening first and are converted into ACS F606W and F814W magnitudes by the transformations of Sirianni et al. (2005), then are randomly added to the original images with Poisson noise added. Then we adopt the same photometry method with Dolphot to recover those field stars. The recovered field stars will have similar photometry errors as the cluster stars, as well as the completeness and blending effect.

2.4.3 Estimate the High Mass-ratio Binary Fraction

To estimate the high mass-ratio binary fraction, we divided the MSRL-subtracted CMD into different regions to count stars (see Figure 2.6, left panel). In Figure 2.6, the green line is the equal-mass binary population. The red line on the right side of the main sequence is the binary population with binary mass-ratio equal to 0.5. The binary mass-ratio of 0.5 is chosen because in most cases, this binary population is beyond the 3 σ photometric errors of the main-sequence stars. The dash blue lines are the upper and lower limits of usable stars for both F606W magnitude and residual color. The main-sequence star (or single star) region S is defined between the red lines. The binary region B is where the residual color is greater than the 0.5 binary mass-ratio curve and less than 0.2 (i.e. on the right side of the red lines but on the left side of dash blue line). The residual region R is where the residual colors are beyond the blue side of the symmetric line for the 0.5 binary mass-ratio curve. but greater than -0.2.

We then count stars separately in those regions for three types of star populations, observed stars, simulated blended stars, and simulated field stars. The simulated blended stars and field stars are generated with methods mentioned in Section 2.4.1 and 2.4.2. Region S contains mainly single stars (main-sequence stars), with some field stars contaminated. Region R contains main-sequence stars with large photometric errors, and with some field stars contaminated. Region B contains mainly binaries with mass-ratio greater than 0.5, with some blended stars and field stars. It also has some main-sequence stars with large photometric errors, and can be estimated with the number in region R. So the high mass-ratio binary fraction $fb(highq)$ can be calculated by the formula:

$$fb(highq) = \frac{n_B^{obs} - n_B^{blend} - n_B^{field} - (n_R^{obs} - n_R^{field})}{n_t^{obs} - n_t^{field}}, \tag{2.1}$$

where n_B^{obs}, n_B^{blend}, and n_B^{field} are the star numbers in region B for the observed stars, blended stars, and field stars, respectively. n_R^{obs} and n_R^{field} are the star numbers in region R for observed stars and field stars, respectively. $(n_R^{obs} - n_R^{field})$ represents any residual main-sequence stars with large photometric errors. This number should be also subtracted from region B assuming symmetric distribution. n_t^{obs} and n_t^{field} are total star numbers in the dashed blue line box for observed stars and field stars, which is the whole restricted region we use during the analysis. The 1 σ error estimate for the binary fractions is given in Appendix C.

2.5 The Global Binary Fractions

The high mass-ratio (> 0.5) binary fraction discuss in Section 2.4 only accounts for those binaries with large distances to the main-sequence stars. Binaries with small mass ratios, however, are ignored, as they are too close to the main-sequence and are hidden by the photometric errors. But as long as we know exactly what the photometric errors are and the rate of superposition of stars, we can even statistically recover small mass-ratio binaries hidden in the main sequence.

2.5.1 The Star Counting Method

To avoid contaminations from photometric errors, we did three things. First, we only select stars 3 to 4 magnitudes below the turn-off point to exclude faint stars with larger photometric errors. Second, we add two gaussian models to represent the photometric errors during fitting, one for the main component with similar small errors, and the other for stars with larger errors. Third, we introduce the parameter q_{cut} in the binary model, which represents the minimum binary mass-ratio we can get from the data, below which binaries are undetectable.

To estimate this, we first fit the residual color distribution with two Gaussian models, which represent the photometric errors of the main-sequence stars. The fit is only applied from 0.02 on the red side to all the blue side, since the blue side is not affected by both blending stars and real binaries, the broadening is only due to photometric errors. The fit is quite good (with χ^2 close to 1). The positive residual

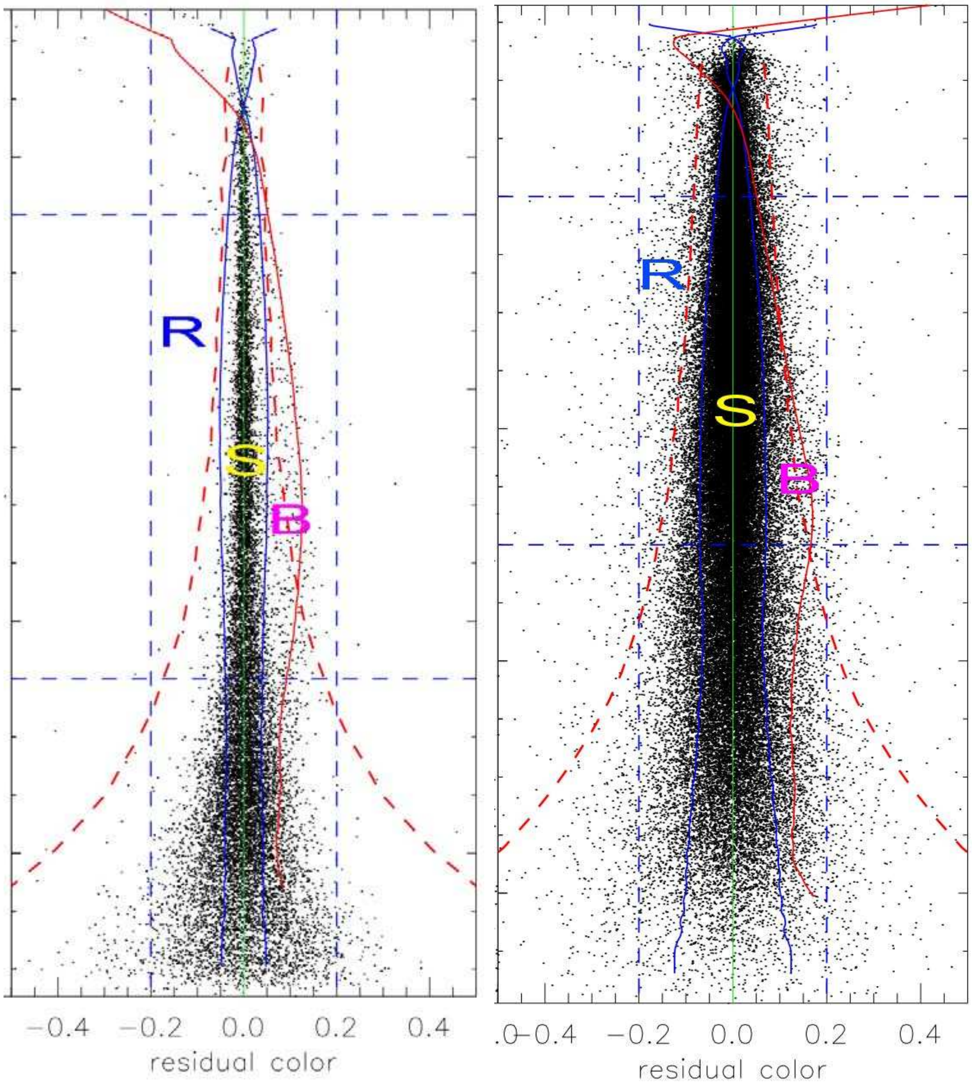

Figure 2.6: Demonstration of the regions when measuring the minimum binary fraction. The straightened color-magnitude diagrams are for NGC 5053 (left) and NGC 2808 (right). Left panel: the green line is the equal-mass binary population. The solid blue curves are the binary population with mass ratio equals 0.5 (right curve), and its symmetric one on the left. The dashed red lines are the $\pm 3\sigma$ photometric spread of color in comparison. The dash blue lines are the upper and lower limits of usable stars for both F606W magnitude and residual color. The main-sequence star (or single star) region S is defined between the solid blue lines. The binary region B is where the residual color is greater than the 0.5 mass-ratio binary line and less than 0.2. The residual region R is where the residual colors are beyond the blue side of the left solid blue line but greater than -0.2. Right panel: same as left but for NGC 2808 with large photometric errors. The 3 σ photometric limit lines (dashed red lines) intersect with the equal-mass binary line, indicating that the photometric spread is so large that even the equal-mass binary signals are buried.

of the fitting on the red side is due to binaries, with contaminations from blending stars and field stars.

After subtracting the photometric errors, field stars, and blended stars, the residual color distribution on the red site is only from the contribution of physical binaries. We summed all the residuals on the red side and divided it by the total number of stars without the field stars, which gives the binary fraction including low mass-ratio binaries.

2.5.2 The χ^2 Fitting Method

There is another way to account for low mass-ratio binaries, and one can even constrain the binary mass-ratio distribution function. Here, we constructed the binary population by fitting to an additional binary mass-ratio distribution function.

We assume the binary mass-ratio distribution function following the power law: $f(q) \propto q^x$, where $q \equiv M_s/M_p$, and with a minimum value of q_{min}, and a maximum value of 1 (equal mass binaries). The minimum mass for the secondary star is set to 0.2 $M_\odot$ (the observed lowest mass from luminosity function of F606W band), thus this will set a minimum value of q_{min} not to be 0. We have a detailed discussion on how the stellar IMF could affect the binary mass-ratio distribution function in Appendix D. First we assume here three different cases for the power of x, $x = 0$, a flat mass-ratio distribution; $x = -1$, which leads to a peak at low mass ratios; $x = 1$, which leads to a peak at high mass ratios. Whenever there are enough stars, we can let x free to fit.

To construct the physical binary population, we first assume a binary fraction of f_b, or a total of $N * f_b$ stars to be in the binary systems, where N is the total number of the observed stars. We then extract V magnitudes with the number $N * f_b$ from the observed V magnitude luminosity function to be the primaries' V magnitudes. The V magnitudes of the secondary stars are calculated using a mass-ratio q extracted from an assumed mass-ratio distribution and an assumed mass-luminosity relationship: $L \propto M^{3.5}$. Their I magnitudes are derived from the MSRL, and the combined binary magnitudes are calculated. Each binary system is added the photometric errors at their V and I magnitudes to simulate the photometric spreads. Finally, we can obtain the residual color distribution for the constructed binary population by subtracting the color of MSRL. We repeat this process for 30 times for each binary fraction f_b, and construct the average profile for the physical binary population as the way we applied to blended stars.

Now, we have models for single stars (two gaussian models), field stars (see Section 2.4.2) , superposition of stars (see Section 2.4.1), and binary model with the known fraction f_b (see Section 2.5.2). The total sum of all these models will produce the final model to compare to the observed residual color distribution profile with a χ^2 test. For a given cluster, the models for single stars, field stars, and the blending stars are fixed as they depend only on the observed luminosity function, Galactic positions, and observed light distribution. The only model that changes during the fitting process is the binary model, as it varies with the binary fraction f_b, and the power index x from the binary mass-ratio distribution function.

We use the bi-section method to search the best-fit f_b (i.e. fits with the minimum chi-square value) at each assumed x. For clusters with enough bins, we also fit the power of x.

A fitting example is shown in Table 2.3, for NGC 4590. The first three rows in the table show the fitting results with the power x, and the minimum binary mass ratio q_{min} fixed, only with the binary fraction as a free parameter to fit. The error range in the table is estimated by changing the parameter so that the χ^2 value changes by 1.0 (or 1 σ confidence level). The χ^2 value favors more on the model with the power $x = -1$, which also gives the higher value of binary fraction $(10.8 \pm 0.4)\%$. With the power x, and q_{min} free to fit, the fit improves significantly ($\chi^2/dof = 88.4/82$), with a binary fraction of (10.8 ± 0.3)%. Figure 2.7 shows the residual color distribution fitted by only Gaussian model (upper) and by best-fit model (lower) for NGC 4590. Symmetric spread of the main-sequence is due to photometric errors, which can be fitted by Gaussian model fairly well, as there is no large systematical residuals on the blue side. The asymmetric spread of the main-sequence is due to binary populations and blending of stars, which is shown as positive residuals on the red side on the upper panel. In the lower panel, models for binaries and blending of stars are included, and this best-fit model fits well to the observed data. Figure 2.8 shows the model components for the fitting (upper) and the enlarged view (lower) for NGC 4590. Solid red line: overall model; dashed red line: gaussian model for photometric errors; dashed green line: binary model; dashed blue line: model for blending due to overlapping stars; black histogram: observed residual color distribution. For this cluster, the field stars are around 50 in the field of view of HST, so they are negligible.

Table 2.3: Example of the fitting results for NGC 4590.

Method	Power x	q_{min}	f_b(counting)%	f_b(fitting)(%)	χ^2/dof
fixed x, q_{min}	0	0.24	10.4	9.4 ± 0.7	175.9/84
fixed x, q_{min}	1	0.24	10.4	6.8 ± 0.2	236.3/84
fixed x, q_{min}	-1	0.24	10.4	10.8 ± 0.4	126.7/84
fit all	-2.3 ± 1.5	0.325 ± 0.007	10.8	10.3 ± 0.4	88.4/82

2.6 The Binary Fraction Radial Analysis

One effect of globular cluster dynamical evolution is mass segregation, which implies that massive stars tend to sink to the center of the core while light stars tend to drift to the outside of the cluster. Since a binary system contains two stars, it is more massive than a single star. So binaries tend to sink towards the cluster core by mass segregation. By performing radial analysis of binary fractions, we can test this dynamical effect.

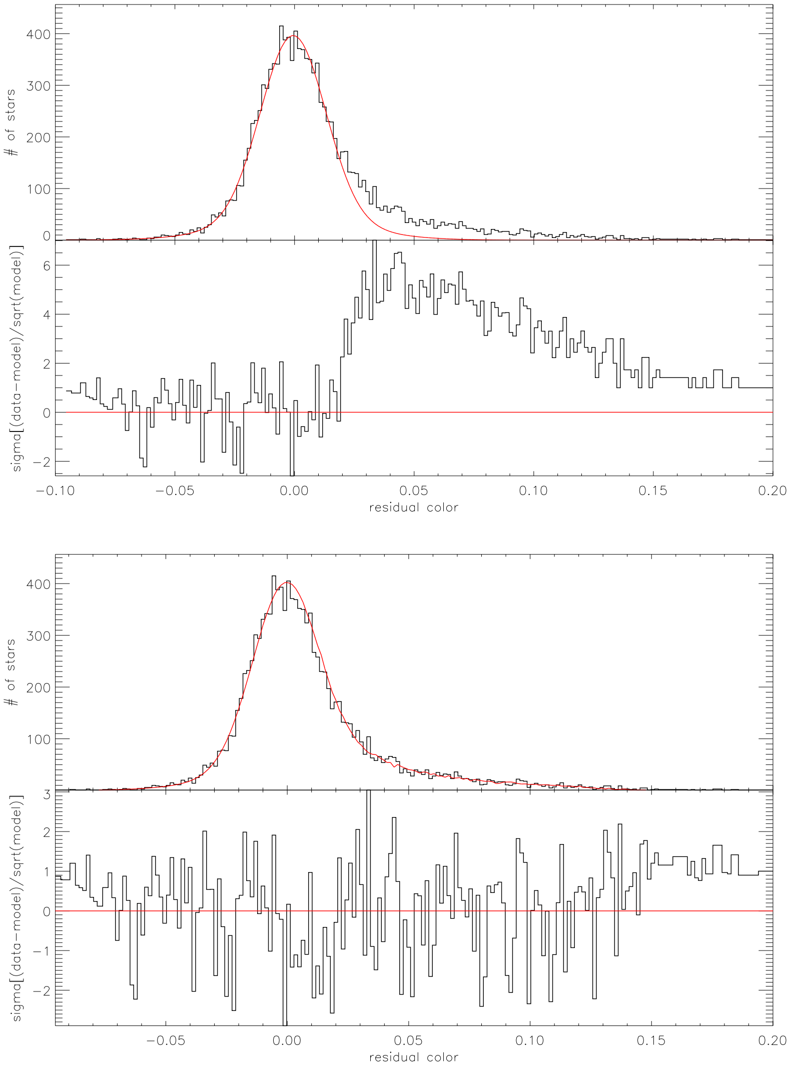

Figure 2.7: The residual color distribution fitted by only Gaussian model (upper) and by best-fit model (lower). Symmetric spread of the main-sequence is due to photometric errors, which can be fitted by Gaussian model fairly well, as there is no large systematical residuals on the blue side. The asymmetric spread of the main-sequence is due to binary populations and blending of stars, which is shown as positive residuals on the red side on the upper panel. In the lower panel, models for binaries and blending of stars are included, and this best-fit model fits well to the observed data.

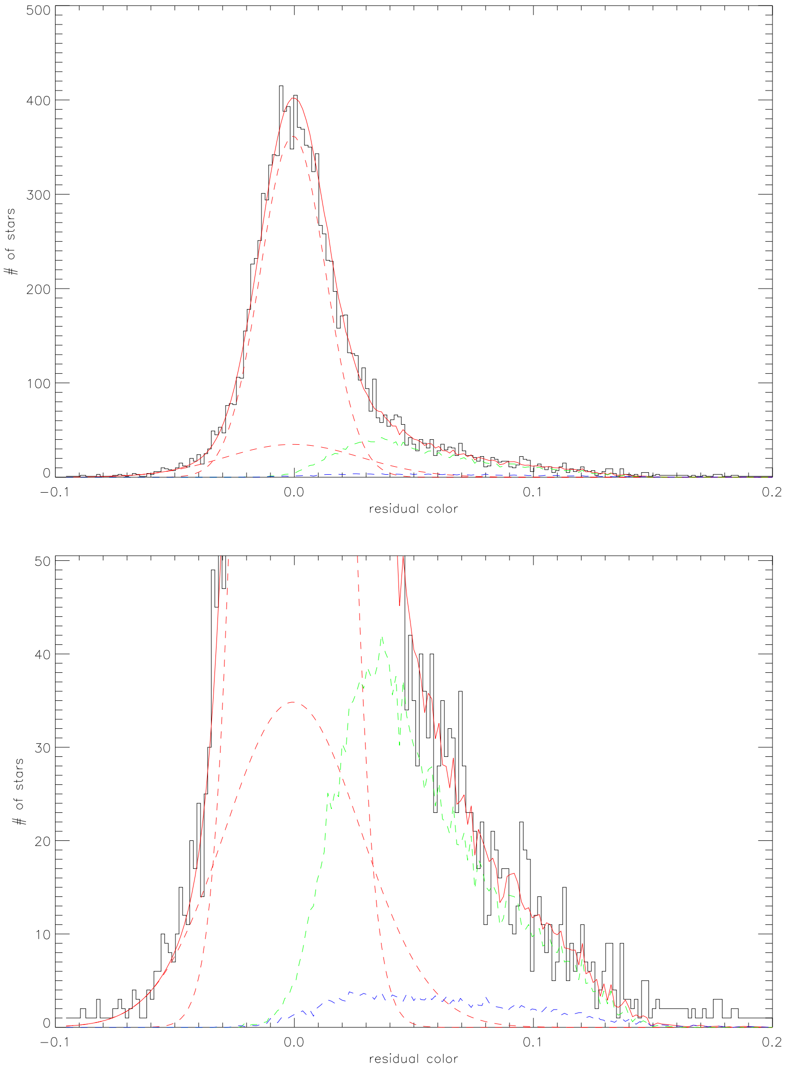

Figure 2.8: Model components for the fitting (upper) and the enlarged view (lower). Solid red line: overall model; dashed red line: gaussian model for photometric errors; dashed green line: binary model; dashed blue line: model for blending due to overlapping stars; black histogram: observed residual color distribution. For this cluster, the field stars are around 50 in the field of view of HST, so they are negligible.

2.6.1 The Analyzing Method

In this analysis, we divide the whole ACS field of view into three annular bins, with their centers at the cluster center obtained from Harris 1996 (2010 edition). The bin sizes are determined so that each bin contains roughly one-third of total stars recovered from the whole field. This is done iteratively by searching from the outer most bin, which is half size of the ACS CCD side. The inner radius is 1 pixel smaller than the outer radius. Then we count the star number inside this annulus. If the star number achieves one-third of total stars, we then find the inner radius for the bin. Otherwise, we decrease the inner radius by 1 pixel, and count again until the star number achieves one-third of total stars. By dividing image into three annular bins with similar star number, we can have similar statistical quality for each bin to compare.

2.6.2 The Radial CMD Qualities

In Appendix F, we plot the CMDs at different radii bins. The CMD quality for the central bin is the worst among the three, which shows larger photometric spread and fewer faint star recovery than the other two. This is understandable, as towards the center region of a cluster, the star density becomes higher and higher. This not only increases the background level, making fainter stars harder to detect, but also increases the blending probability, making the PSF determination poorer.

2.7 Discussions on the Techniques

In this section, we will discuss the factors that can affect the measurement accuracy of binary fractions in globular clusters using their CMDs.

2.7.1 The Photometric Errors

The key aspect to estimate binary fraction using CMD method is the highly accurate photometry for the CMDs. As the photometric errors become larger, the spread of the main-sequence becomes larger, which will smear out the signals from binaries with small mass-ratio. In order to decrease the photometric errors, we need to increase the exposure time to increase the S/N ratio at certain magnitude. This is true for low density clusters, in which stars are quite isolated, and the PSF can be determined quite well. The photometric errors are approaching to their theoretical limit. High density clusters, however, have very crowded central region, where the high and varied background make the PSF determination quite uncertain. Most of the errors are not from low S/N ratios but from uncertainties in the PSFs and the backgrounds. Increasing the observing time for those crowded clusters would not help lower the photometric errors. Instead, developing more sophisticated PSF photometry algorithm for crowded region is needed, which is still not matured yet.

2.7.2 The Metallicity Dispersion

Theoretical model shows that the dispersion of the metallicity of a globular cluster can also cause spread in color on the main sequence. Figure 2.9 shows that a metallicity (Z) difference of 0.002 (from red to blue line at certain V magnitude), equivalent to $\delta[Fe/H] = 0.30$, can cause a spread of about 0.054 magnitude in color, and 0.284 in V magnitude. So given the uncertainty in [Fe/H] of 0.03, the caused spread in color will be 0.005, and shift in V magnitude will be 0.028. The intrinsic color spread is smaller compared to the typical width in color of the main-sequence with the HST observation (about 0.012), and the shift in V magnitude will not affect the color distribution. Thus the intrinsic metallicity dispersion in most clusters can be negligible. For multi-population systems, however, this will not be the case (Piotto et al., 2007; Pasquini et al., 2011).

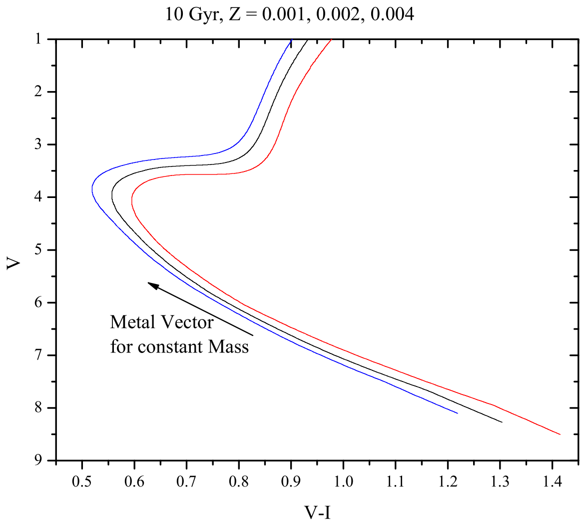

Figure 2.9: Isochrone Models at different metallicity.

2.7.3 The Differential Reddening

Observations on globular clusters located near the Galactic center can be affected by the existence of large and differential extinction of the foreground dust. Alonso-Garcia et al. (2011) show the technique to correct this effect. From our sample, most clusters are well above the Galactic plane and with the reddening E(B-V) less than 0.1, which are not important to spread the color of the main sequence comparing to their photometric errors. For clusters near the Galactic plane, however, the reddening can be very large. Along with the heavily contaminated field stars, the determination of binary fractions in those clusters are quite uncertain.

CHAPTER 3

HST Observations of Globular Cluster Binaries: Results

In this chapter, we will show the analysis results for the binary fractions in the sample. For each cluster, we performed analysis using three different methods (the high mass-ratio binary method, the star counting method, and the χ^2 fitting method) discussed in Section 2.4 and 2.5, and for three different types of regions on the CCD chips (i.e. the region including the whole field of view, within the core and the half-mass radius, and radial annular bins).

3.1 Binary Fractions within the Whole Field of View

Analysis of the whole field of view statistically gives the most reliable results, as it includes the most number of stars. In the Appendix E from Figure E.1 to E.35, we show the results for each cluster in the sample. The 1st row is for HST ACS images in inverted black and white color and squared color scale. The red circle on the left image is the core radius region, while the green one is the half mass radius region. For some clusters (e.g. NGC 104), the green circle is not shown, indicating the half-mass radius region is too large to be covered by the ACS field of view. The image on the right panel shows the recovered stars (green dots) and the three radial bins (blue circles) discussed in Section 2.6. Note that, in some dense clusters (e.g. NGC 104), the center regions do not shown recovered stars, indicating that the stellar density is too high to have a good photometry measurement. There are no stars recovered near the CCD edge and between the gap of two chips, because the drizzled patterns during the observations cause such regions to have only one observation coverage, which will be rejected during the screening process.

The left panel on the 2nd row in Figure E.1 to E.35 shows the observed CMD (left half) and the straightened CMD (right half) for the whole field of view, with the defined MSRL (solid green lines) on top of them. We also plot the equal-mass binary line (solid red line) to indicate the maximum distances in color a binary can be relative to the main sequence. On the straightened CMD, we also add the 0.5 mass-ratio binary line (solid blue line) and its symmetric line on the blue side to show to star selecting region discussed in Section 2.4. To demonstrate the photometric quality, we plot the 3 σ photometric errors in color and its symmetric line on the blue side (dashed red lines). The dashed blue lines show the CMD portion where we analyzed on.

The right panel of the 2nd row shows the luminosity function of the F606W magnitude for stars in all field of view, which is corrected by the completeness at each magnitude.

The 3rd row shows the residual color distribution of the stars (black histograms) in the chosen magnitude and residual color range (i.e. the box region formed by the dashed blue lines on the straightened CMD). The red curve is the two-Gaussian model (representing the main-sequence stars with certain photometric spreads) plus the field star and blending star model. The lower panel shows the red curve subtracted distribution. Note that the residuals on the left side are quite small and around 0, indicating a good fit by the red curve. On the right side, however, there are systematic positive residuals even after accounting for the field star and blending star contaminations, indicating binary signals. With this residual distribution, we can estimate binary fractions using the star counting method discussed in Section 2.5.1.

The right panel on the 3rd row shows the best-fit model (including the binary model) to the residual color distribution. The method is discussed in Section 2.5.2. The last row shows the model components (left panel) for the fitting method and the zoom-in view (right panel). In the plots, the solid red curve is the overall model. The dashed red curves are the two Gaussian components, while the green curve is the binary model. The blending stars is modeled in blue dashed curve, and the field stars is in black dashed curve. By comparing the area of each component in the model, we can get a direct view of the contribution from each component.

In Table 3.1, we list the analysis results using different methods for the whole field of view. In this table, we give the region size in terms of their half mass radii in Column 2. In Column 3, 4, and 5, we list the binary fractions with 1 σ errors for high mass-ratio ($q > 0.5$) method, star counting method, and χ^2 fitting method, respectively. Column 6 and 7 are the fitted parameters in the χ^2 fitting method, where power x is the power index of the power-law function for the binary mass-ratio distribution, and q_{min} is the minimum binary mass ratio we can get. Column 8 gives the χ^2 and degrees of freedom for the fitting method. The last column gives the binary fraction quality flags. They indicate the main error sources. Only the results including one quality flag can be used, such as g (good estimate), d (dense core), and n (small number of stars). Results including flag f (field stars) or e (large photometric errors) should be used in caution, as the contaminations are asymmetric and with large uncertainties (some fractions become negative values due to the asymmetric distribution of field stars).

From the table, we can calculate the mean binary fractions including 25 reliable binary fractions from the three methods: 5.2% (high q), 6.3% (counting), and 7.3% (fitting), respectively. In Figure 3.1, we show the comparisons of binary fractions obtained through different methods. Blue filled circles are for binary fractions obtained by high q method Vs. counting method. Red open circles are for binary fractions obtained by fitting method Vs. counting method. The black solid line shows where the two methods give the same results. From the figure, we can see that the binary fractions obtained through the counting and fitting method are consistent with each other, while they are usually larger than the values obtained through high mass-ratio method. This is because the latter method does not include binaries with small mass ratio that are hidden in the main sequence, while the former methods can statistically recover part of the signals from the small mass-ratio binaries.

For the fitting method in Table 3.1, the fitted power x has a mean value of -1.9 ± 1.1 (from the 25 reliable clusters), indicating that most binaries distribute on small mass ratios. The fitted minimum binary fraction q_{min} has a mean value of 0.30 ± 0.06, which is smaller than the cut-off ratio in the high mass-ratio method ($q = 0.5$), indicating that the fitting method can recover part of mass-ratio binaries that are hidden in the main sequence. In Figure 3.2, we show the average mass-ratio function constrained from the sample, with $x = -1.9$ and $q_{min} = 0.30$.

3.2 Binary Fractions within the Half-mass Radius

The analysis for the binary fractions within the half-mass radius is important, as it provides results that can be compared among different clusters versus their cluster properties. One difference with the fitting method is that we fixed the values of the power index x and the minimum mass-ratio q_{min} to the ones obtained by whole field analysis, because there are more stars to constrain the parameters using the whole chips.

The binary fractions are listed in Table 3.2, which is similar to Table 3.1, only that we omit the size column as all the regions are 1 half-mass radii. We also exclude the columns of power index x and the minimum mass-ratio q_{min}, as they are all fixed

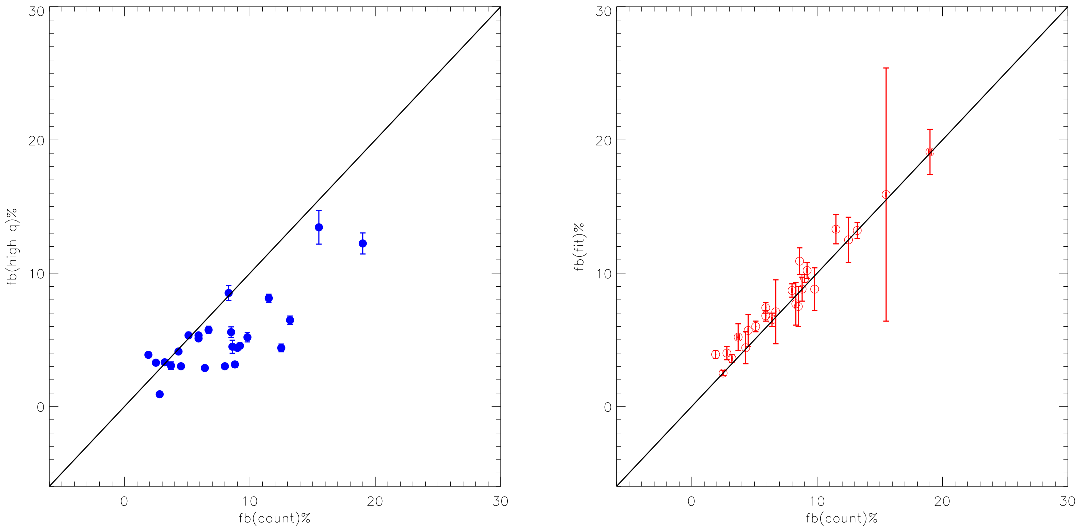

Figure 3.1: Comparisons of binary fractions from the whole field of view between different methods. Blue filled circles: binary fractions obtained by high q method Vs. counting method. Red open circles: binary fractions obtained by fitting method Vs. counting method. The black solid line shows where the two methods give the same results.

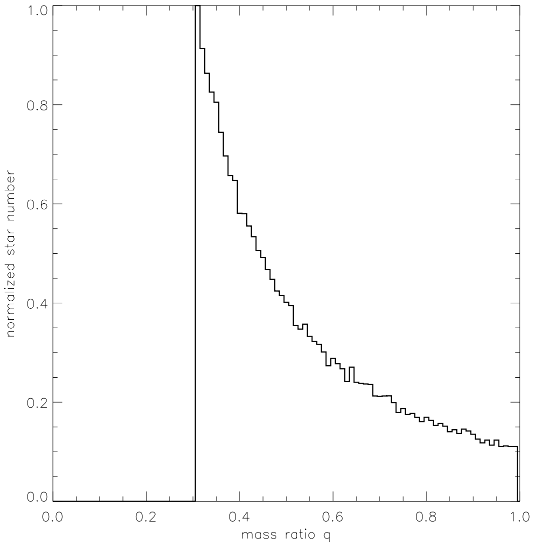

Figure 3.2: The binary mass ratio distribution function constrained by the sample results. The power $x = -1.9$, and the minimum mass ratio $q_{min} = 0.30$.

Table 3.1: Fitting results for whole field of view

Source	size(in r_h)	$f_b(q > 0.5)$%	$f_b(count)$%	$f_b(fit)$%	Power x	q_{min}	χ^2/dof	Note[a]
NGC104	0.75	3.01±0.13	8.04±0.70	8.70±0.50	-2.95±0.05	0.28±0.01	204.1/162	d
NGC288	1.06	6.47±0.31	12.87±1.32	13.20±0.60	-1.50±0.09	0.27±0.00	120.1/106	g
NGC362	2.89	4.39±0.16	8.28±0.75	9.60±0.30	-2.11±0.19	0.24±0.01	176.9/142	d
NGC1851	4.64	2.88±0.15	5.51±0.82	6.50±0.50	-2.91±0.05	0.29±0.01	126.4/136	d
NGC2808	2.96	1.26±0.18	-2.05±0.66	0.50±0.00	0.00±3.00	0.77±0.45	299.5/164	d,p,e
NGC4590	1.57	8.12±0.30	11.14±1.27	13.30±1.10	-2.48±0.38	0.33±0.00	141.6/ 96	g
NGC5053	0.91	5.57±0.40	8.09±1.81	7.50±1.50	-0.98±0.75	0.33±0.01	43.9/ 70	g
M3	1.02	5.10±0.17	5.45±0.70	6.80±0.40	-2.11±0.19	0.33±0.00	200.3/161	d
NGC5466	1.03	5.19±0.35	8.96±1.86	8.80±1.60	-1.50±0.38	0.30±0.03	34.6/ 63	g
NGC5897	1.15	5.74±0.28	6.10±1.27	7.10±2.40	-0.75±0.19	0.33±0.01	100.4/ 98	g
NGC5904	1.34	3.01±0.14	4.61±0.82	5.70±1.20	-3.00±0.05	0.30±0.06	113.6/122	d
NGC5927	2.15	2.44±0.21	12.29±0.93	14.20±0.50	-3.00±0.01	0.24±0.01	157.3/148	f
NGC6093	3.88	3.87±0.18	1.42±0.84	3.90±0.30	-3.00±0.09	0.40±0.00	207.6/125	d
NGC6121	0.55	4.78±0.48	11.73±2.16	16.20±0.90	-3.00±0.19	0.25±0.01	66.0/ 62	f
NGC6101	2.25	5.33±0.23	6.54±1.12	7.40±0.40	-1.50±0.19	0.31±0.00	105.8/100	g
M13	1.40	3.28±0.14	2.15±0.71	2.50±0.20	-2.81±0.09	0.41±0.01	147.1/145	d
NGC6218	1.34	3.15±0.22	8.51±1.29	8.80±0.90	-1.12±0.38	0.18±0.01	92.6/ 91	g
NGC6341	2.32	4.12±0.18	4.19±0.69	4.40±1.20	-1.03±0.75	0.27±0.03	247.0/146	d
NGC6352	1.15	-0.58±0.87	6.92±2.09	5.50±2.30	-1.88±0.38	0.21±0.06	110.4/ 99	f
NGC6362	1.15	4.39±0.29	11.21±1.42	12.50±1.70	-2.48±0.09	0.24±0.03	108.2/ 95	g
NGC6397	0.82	4.48±0.49	7.81±1.81	10.90±1.00	-3.00±0.19	0.35±0.00	103.1/ 79	g
NGC6541	2.23	2.53±0.19	5.57±0.78	7.60±0.30	-3.00±0.02	0.27±0.00	227.7/140	d,f
NGC6624	2.89	1.57±0.54	13.77±1.32	27.30±2.90	-2.98±0.19	0.18±0.03	200.2/144	d,f
NGC6637	2.82	2.06±0.30	5.53±1.10	6.60±0.40	-1.88±0.19	0.18±0.01	142.3/135	d,f
NGC6652	4.93	0.87±0.71	-0.03±2.08	1.50±0.50	0.00±3.00	0.89±0.45	92.7/ 85	d,f
NGC6656	0.70	-4.87±0.28	-0.69±0.97	3.90±1.40	-3.00±0.05	0.18±0.03	488.0/124	f
NGC6723	1.55	4.55±0.19	8.79±0.97	10.20±0.60	-3.00±0.05	0.28±0.00	113.2/118	g
NGC6752	1.24	0.91±0.16	2.97±1.04	4.00±0.50	-2.81±0.19	0.25±0.01	124.2/ 98	g
Terzan7	3.07	12.23±0.79	19.67±2.62	19.10±1.70	0.00±0.19	0.18±0.06	40.5/ 63	g
Arp2	1.34	8.51±0.55	8.32±2.16	7.70±1.60	0.00±0.38	0.44±0.23	57.9/ 74	g
NGC6809	0.84	3.31±0.22	3.10±1.31	3.60±0.30	0.00±0.75	0.25±0.06	64.8/ 77	g
NGC6981	2.54	5.33±0.24	5.50±1.25	6.00±0.40	-1.88±0.75	0.38±0.01	85.3/102	d
NGC7078	2.37	4.38±0.17	0.50±0.62	1.50±0.10	0.00±0.19	0.25±0.03	229.2/160	d,e
NGC7099	2.30	3.06±0.28	4.23±1.08	5.20±1.00	-3.00±0.75	0.33±0.06	85.7/ 68	g
Palomar12	1.38	13.44±1.26	7.99±4.25	15.90±9.50	-0.75±1.50	0.25±0.45	13.1/ 33	n

[a] Note:results quality flags. d: dense core; f: field stars; n: small number of stars; p: multi-populations; e: large photometric errors; g: good estimate. Binary fractions with flags of g, d, and n are usually good to use. Uncertainty from flag f is quite large, so be caution when use those values. Binary fractions with more than one flag are not good to use.

Table 3.2: Fitting results within half light radius

Source	$f_b(q > 0.5)$%	$f_b(count)$%	$f_b(fit)$%	χ^2/dof	Note[a]
ngc104	3.03± 0.13	8.03±0.70	8.73±0.81	205.6/162	d
ngc288	6.29± 0.32	12.26±1.38	11.85±0.36	96.9/ 99	g
ngc362	5.69± 0.36	8.17±1.30	6.62±0.35	122.8/118	d
ngc1851	3.89± 0.85	-1.06±2.79	0.50±0.00	40.3/ 73	d,e
ngc2808	-12.09± 0.96	-4.84±2.44	0.50±0.00	71.9/ 90	d,e,p
ngc4590	6.24± 0.30	7.33±1.39	8.62±1.21	112.3/ 87	g
ngc5053	5.57± 0.40	8.17±1.81	8.25±1.68	42.5/ 70	g
m3	5.03± 0.17	5.42±0.70	6.62±0.24	197.4/161	d
ngc5466	5.23± 0.35	9.03±1.86	9.36±0.63	33.4/ 63	g
ngc5897	5.63± 0.28	5.84±1.28	6.28±0.30	82.5/ 96	g
ngc5904	3.15± 0.15	4.84±0.85	5.48±1.17	111.6/122	d
ngc5927	3.87± 0.28	6.18±1.29	5.18±1.03	107.8/127	f
ngc6093	7.59± 0.58	1.25±1.78	2.22±1.73	80.8/ 98	d
ngc6121	4.79± 0.48	-1.94±3.37	0.50±0.35	46.7/ 40	g
ngc6101	5.50± 0.38	6.59±1.12	7.70±0.65	105.7/100	g
m13	3.46± 0.16	2.12±0.75	2.56±0.60	149.2/144	d
ngc6218	3.21± 0.24	8.31±1.35	8.87±2.94	93.3/ 88	g
ngc6341	5.31± 0.29	3.27±0.98	3.33±0.97	151.0/136	d
ngc6352	-0.57± 0.88	6.06±2.11	5.91±1.53	104.7/ 98	f
ngc6362	4.31± 0.29	10.64±1.44	11.59±1.04	99.9/ 94	g
ngc6397	4.47± 0.49	7.75±1.81	10.84±0.67	100.7/ 79	g
ngc6541	3.94± 0.28	1.69±1.08	2.96±0.40	184.6/123	d
ngc6624	1.31± 0.57	8.13±1.96	5.42±7.96	63.7/ 93	f,d
ngc6637	4.16± 0.40	4.10±1.63	2.96±0.59	102.5/103	f,d
ngc6652	3.17± 0.78	11.82±3.67	3.45±1.70	42.6/ 41	f,d
ngc6656	-4.94± 0.28	-0.69±0.97	3.76±1.39	486.9/124	f
ngc6723	4.66± 0.21	7.19±1.06	8.37±1.03	101.3/115	g
ngc6752	0.74± 0.16	2.26±1.07	2.96±0.45	118.3/ 96	g
Terzan7	17.15± 1.40	13.56±2.71	13.30±2.03	43.9/ 62	g
Arp2	8.05± 0.55	4.92±3.31	4.44±1.39	30.9/ 50	g
ngc6809	3.31± 0.22	-5.14±2.92	0.50±0.06	33.4/ 43	g
ngc6981	7.18± 0.38	5.43±1.27	6.13±0.64	85.7/102	d
ngc7078	5.85± 0.32	0.47±0.62	1.48±0.17	231.0/160	d
ngc7099	3.78± 0.44	2.50±1.52	0.50±1.25	103.6/ 62	d
Palomar12	13.36± 1.30	-8.38±6.02	12.31±19.88	7.2/20.0	g

[a] Note: same as Table 3.1.

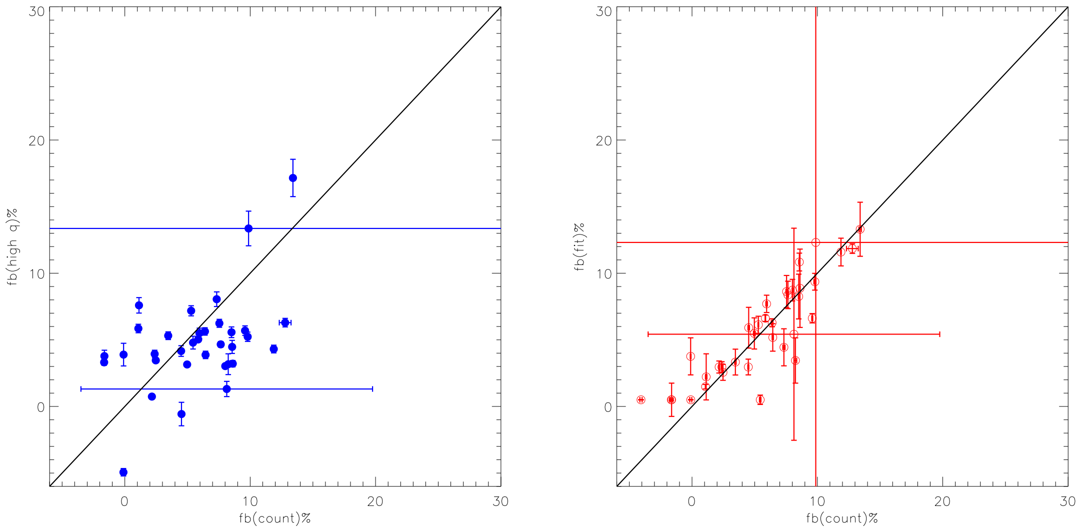

Figure 3.3: Same as Figure 3.1, but for half-mass radius results.

to the values in Table 3.1. The average binary fractions within the half-mass radius from this table is 5.6% (for high q ($q > 0.5$) binary fractions), which includes 27 reliable clusters with flags of d, n, or g. And the results are consistent with the fitting and counting methods (see Figure 3.3).

The binary fractions against ages and the dynamical ages are the most important relation, as it can tell us how the binary fraction evolves with time. The relationship can be compared to the model predictions through different dynamical simulations of globular clusters.

We use a straight line defined below to fit the data points.

$$y = b + k * x, \tag{3.1}$$

where y is the binary fraction and x is the different properties of globular clusters.

Figure 3.4 shows the relationships between the half-mass binary fractions and the ages, dynamical ages (absolute ages divided by the relaxation time at half-mass radius), metallicity [Fe/H], and the absolute V magnitudes. The fitted line parameters and the Spearman rank coefficients are shown in Table 3.3. From this table, we can

Table 3.3: Fitting results for the half-mass binary fractions Vs. different properties of clusters

Vs. Properties	k	b	χ^2/dof	coefficient$_r$	significance
Age	-0.53±0.05	10.02±0.61	1055.2/ 25	-0.392	0.043
Dynamical Age	-0.10±0.01	4.65±0.09	1042.0/ 25	-0.068	0.737
$[Fe/H]$	-1.04±0.11	2.44±0.18	1054.4/ 25	-0.016	0.936
Mv	0.63±0.06	9.12±0.41	1017.0/ 25	0.490	0.010

see that the half-mass binary fractions are anti-correlated with the cluster ages (the Spearman rank coefficient analysis shows a reliable significance), meaning that the half-mass binary fractions are decreasing over time. This could be the fact that binaries are destructed or escape from the clusters, making the whole binary fraction decrease. But we do not see the correlation of half-mass radius binary fractions correlated with the dynamical times, nor the metallicity [Fe/H]. The half-mass binary fractions also show a correlation with the cluster absolute V magnitudes, meaning that less massive clusters (larger Mv in value) should have higher binary fractions. This correlation is also confirmed by Spearman rank coefficient, with very reliable significance. The relationship was also discovered by Milone et al. (2008). The possible explanation for this correlation is that, less massive clusters have lower stellar density, so the relaxation time is longer. This will cause less frequent dynamical interactions between binaries and other stars. So binaries are not destroyed or escape quickly like those in the denser region, leaving the binary fraction still high. The lower density end of this trend is for the open clusters, where they usually have higher binary frequencies ($\sim$ 30% for Hyades by Griffin et al. (1988), $>$ 59 % for Praesepe by Bolte (1991), and 50% for M67 by Fan et al. (1996)). A more recent study of 9 open clusters show 15%-54% of binary fraction (Bica & Bonatto, 2005). For field stars near the solar neighborhood, the binary frequency can be as high as 50% (Duquennoy & Mayor, 1991; Halbwachs et al., 2003).

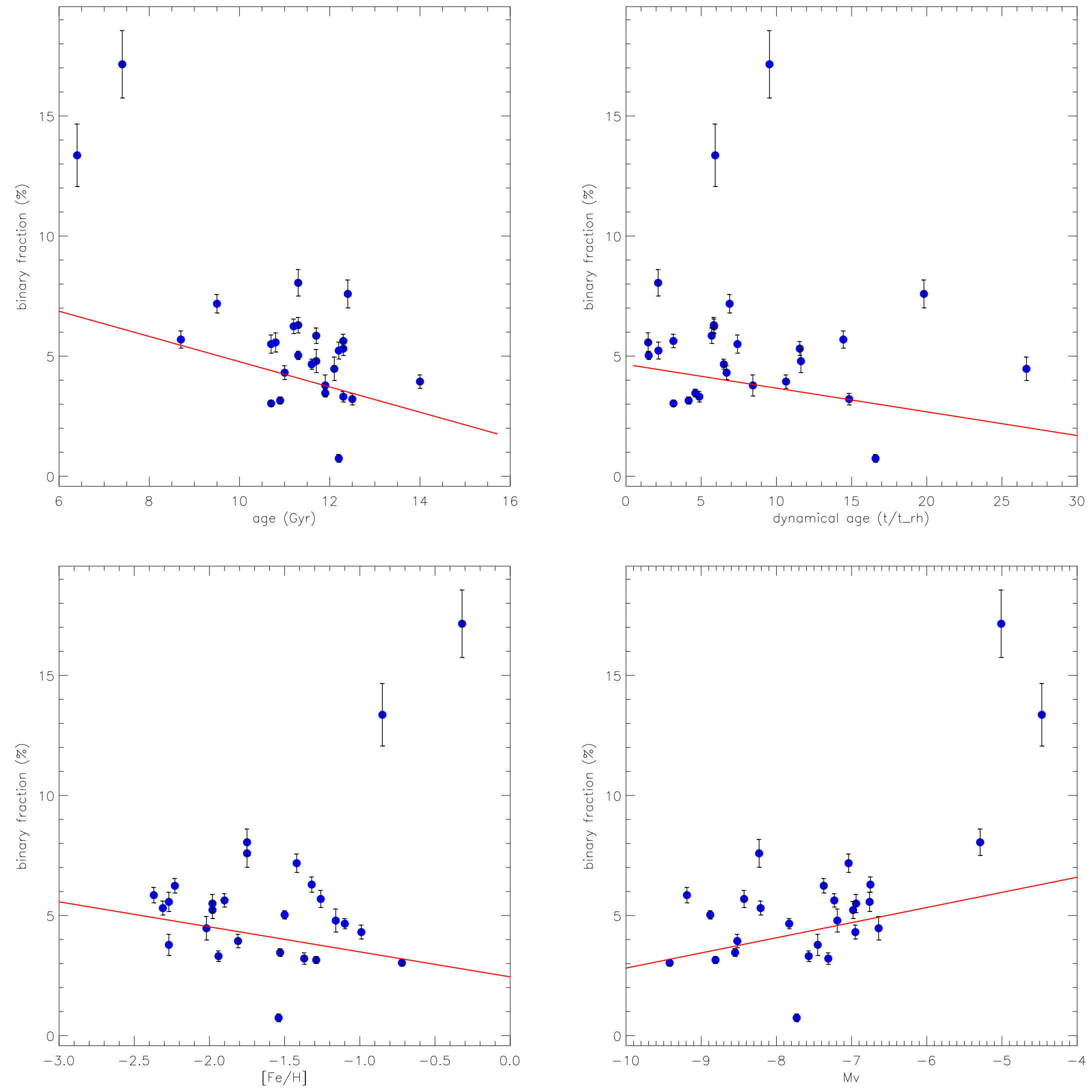

Figure 3.4: The half-mass radius binary fractions Vs. different cluster properties. Upper left: fb(half-mass radius) Vs. ages; upper right: fb Vs. dynamical ages; Lower left: fb Vs. [Fe/H]; Lower right: fb Vs. Mv.

3.3 Binary Fractions within the Core Regions

The binary fractions within the core regions are supposed to represent the dynamical features according to simulations. The binary systems tend to sink to the core while the single stars tend to drift outwards by the mass segregation effect, which make the core binary fractions increase against evolutional time. In our sample, not all the clusters are suitable for the core binary fraction analysis, because 1) the core regions for some dense clusters are too crowded to recover stars; 2) the core regions for some core-collapsed clusters are too small to include enough stars. With such limitations, we only analyzed 25 clusters in our sample with the high mass-ratio method.

Table 3.4 shows the core binary fractions for 25 clusters with the high mass-ratio ($q > 0.5$) method. The mean binary fractions within the core regions is about 7.0% (excluding 8 clusters with field star contamination or due to large photometric errors and low star numbers). Table 3.5 shows the correlation analysis of the core binary fractions with different cluster properties: age, dynamical age, [Fe/H], and Mv. Figure 3.5 shows the correlation plots. From Table 3.5 we can see that, the core binary fractions shows an anti-correlation with the cluster ages. The Spearman rank analysis shows a significant correlation, which indicates that the core binary fractions are decreasing over time, indicating the destruction or escape of the core binaries are more than the binaries sinking to the core caused by the mass segregation effect. The correlation between the core binary fractions and the dynamical ages, however, is not significant. The core binary fractions are also not significantly correlated with [Fe/H] or Mv.

Table 3.4: The core binary fractions for 25 clusters with the high q method

Name	fb(high q)%	Note[a]
ngc104	4.26 ± 2.68	d,n
ngc288	5.64 ± 0.41	g
ngc4590	9.43 ± 0.69	g
ngc5053	5.67 ± 0.40	g
m3	5.42 ± 1.07	d
ngc5466	5.58 ± 0.43	g
ngc5897	5.08 ± 0.34	g
ngc5904	7.73 ± 0.72	d
ngc5927	5.41 ± 0.82	d,f
ngc6101	6.13 ± 0.40	g
ngc6121	4.94 ± 0.63	g
m13	6.17 ± 0.47	d
ngc6218	3.75 ± 0.47	g
ngc6341	1.20 ± 2.47	d,n
ngc6352	1.76 ± 1.30	f
ngc6362	4.81 ± 0.44	g
ngc6541	-0.12 ± 5.47	d,n
ngc6637	8.51 ± 1.27	d,f
ngc6656	-2.39 ± 0.33	f
ngc6723	6.89 ± 0.38	g
ngc6752	5.27 ± 2.47	d,n
ngc6809	3.43 ± 0.24	g
ngc6981	11.56 ± 0.81	g
Arp2	7.42 ± 0.69	n
Terzan7	20.02 ± 2.10	n

[a] Note: same as Table 3.1.

Table 3.5: Fitting results for the core binary fractions Vs. different properties of clusters

Vs. Property	k	b	χ^2/dof	coefficient$_r$	significance
Age	-2.40±0.14	32.75±1.61	501.9/ 23	-0.595	0.002
Dynamical age	0.05±0.03	4.41±0.26	787.3/ 23	-0.150	0.474
$[Fe/H]$	0.97±0.24	6.27±0.37	773.9/ 23	0.140	0.505
Mv	1.94±0.15	19.07±1.11	617.6/ 23	0.265	0.201

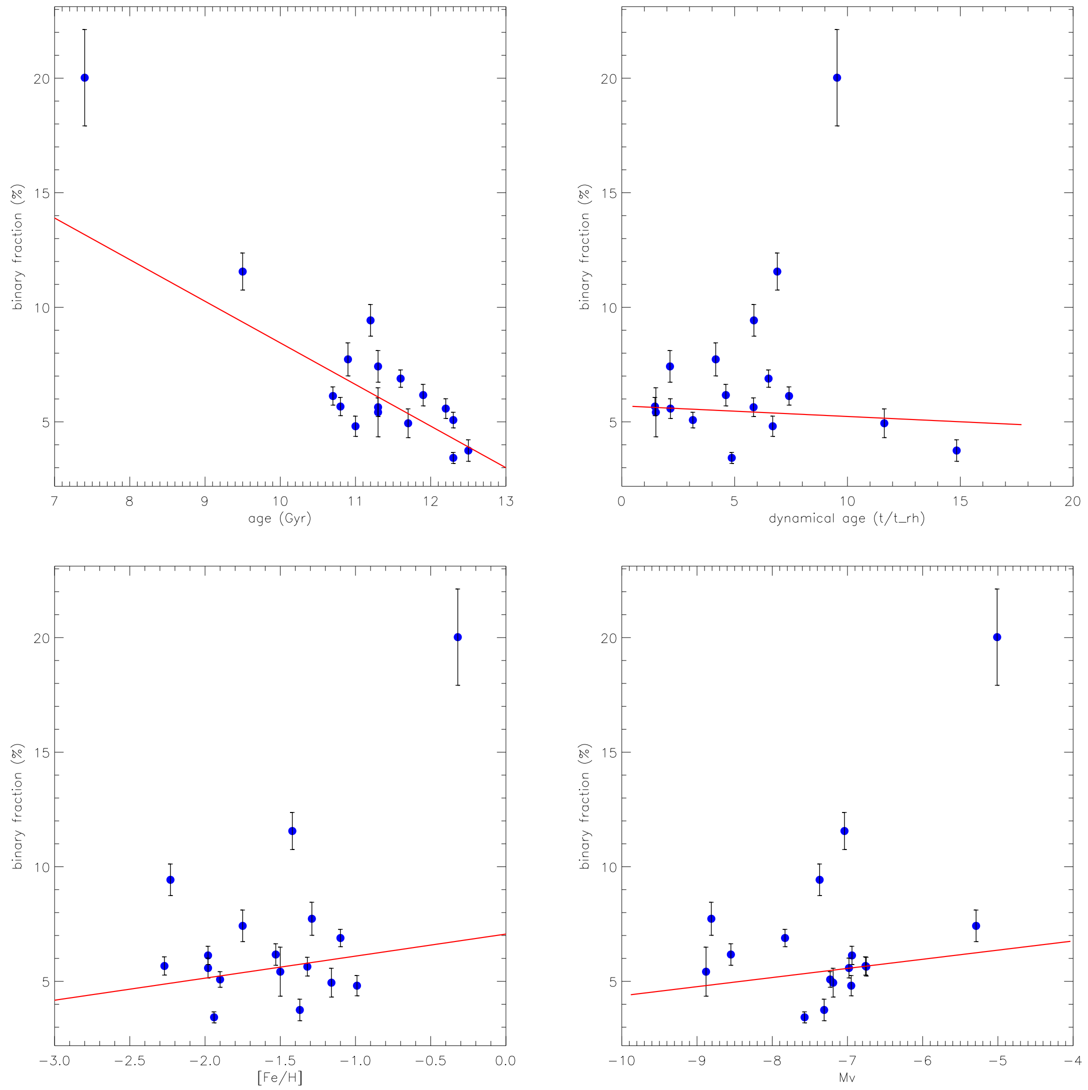

Figure 3.5: Core binary fractions Vs. different cluster properties. Upper left: fb(core) Vs. ages; upper right: fb(core) Vs. dynamical ages; Lower left: fb(core) Vs. [Fe/H]; Lower right: fb(core) Vs. Mv.

Table 3.6: Fitting results for radial bins

Source	Bin Range(r_h)	$f_b(q > 0.5)$%	$f_b(count)$%	$f_b(fit)$%	χ^2/dof	Note[a]
ngc104	0.00-0.29	4.14±0.29	5.63±1.27	4.19±0.38	144.7/130	d
	0.29-0.42	2.72±0.22	10.02±1.25	11.94±0.54	75.7/110	d
	0.42-0.56	2.11±0.18	6.22±1.26	10.59±1.63	104.7/100	d
ngc288	0.00-0.43	4.75±0.51	4.51±2.39	2.59±0.98	64.0/ 63	g
	0.43-0.70	6.96±0.58	17.21±2.33	23.63±2.32	77.0/ 71	g
	0.70-1.05	6.94±0.55	18.69±2.32	35.45±8.90	38.8/ 67	g
ngc362	0.00-0.97	5.74±0.37	8.38±1.34	6.53±0.40	127.7/118	d
	0.97-1.48	4.57±0.27	12.61±1.32	15.76±1.15	91.9/101	d
	1.48-2.16	2.53±0.22	7.73±1.33	10.37±1.14	89.0/ 87	g
ngc1851	0.00-1.55	3.80±0.37	3.03±1.47	2.84±0.63	91.5/113	d
	1.55-2.34	2.20±0.25	5.93±1.45	8.62±1.02	76.0/ 87	d
	2.34-3.55	1.50±0.20	6.48±1.45	8.74±0.97	79.1/ 76	d
ngc2808	0.00-1.35	-1.56±0.38	-2.44±1.19	0.50±0.01	186.9/141	d,e,p
	1.35-1.73	1.14±0.29	-1.08±1.17	0.56±0.14	180.3/132	d,e,p
	1.73-2.26	1.49±0.28	-3.54±1.17	0.50±0.02	204.4/130	d,e,p
ngc4590	0.00-0.44	8.27±0.61	7.02±2.30	5.42±1.21	47.3/ 64	g
	0.44-0.74	3.88±0.45	5.21±2.30	6.90±1.58	38.4/ 55	g
	0.74-1.14	6.40±0.51	10.83±2.28	19.70±1.83	74.5/ 60	g
ngc5053	0.00-0.36	5.64±0.77	8.88±3.24	5.91±2.57	22.2/ 43	g
	0.36-0.52	4.71±0.70	2.33±3.31	6.41±4.18	26.6/ 40	g
	0.52-0.68	4.90±0.74	0.12±3.32	5.42±2.20	25.1/ 41	g
m3	0.00-0.35	6.17±0.39	6.48±1.26	5.44±1.48	112.2/135	d
	0.35-0.54	3.94±0.28	6.85±1.25	9.21±0.38	82.8/111	d
	0.54-0.76	3.62±0.24	5.55±1.25	8.37±1.42	128.6/102	d
ngc5466	0.00-0.39	5.09±0.66	-0.48±3.41	1.48±1.48	31.8/ 39	g
	0.39-0.58	5.23±0.66	3.02±3.37	8.37±4.37	24.6/ 38	g
	0.58-0.79	4.62±0.62	1.96±3.37	6.41±4.51	34.4/ 39	g
ngc5897	0.00-0.44	4.75±0.56	2.11±2.32	1.98±0.67	41.0/ 63	g
	0.44-0.64	4.25±0.49	5.92±2.29	6.65±0.98	29.6/ 59	g
	0.64-0.85	5.70±0.51	7.40±2.29	11.82±1.72	32.6/ 61	g
ngc5904	0.00-0.43	4.85±0.35	1.94±1.49	2.35±1.47	75.4/103	d
	0.43-0.68	2.10±0.24	6.11±1.47	6.90±1.40	75.9/ 78	g
	0.68-0.99	1.15±0.18	4.09±1.48	6.28±2.12	52.3/ 67	g
ngc5927	0.00-0.75	4.69±0.38	4.43±1.66	2.71±0.86	117.0/112	df
	0.75-1.15	1.19±0.34	11.01±1.64	15.85±1.13	87.3/ 96	f
	1.15-1.64	0.78±0.39	21.00±1.66	35.45±2.88	122.6/ 94	f
ngc6093	0.00-1.17	7.09±0.44	3.29±1.46	3.73±0.46	100.7/108	d
	1.17-1.82	2.97±0.29	1.54±1.46	4.25±0.69	89.0/ 85	d
	1.82-2.96	0.41±0.23	-0.52±1.48	0.75±0.96	47.2/ 73	g

continued on next page

continued from previous page

Source	Bin Range(r_h)	$f_b(q > 0.5)$%	$f_b(count)$%	$f_b(fit)$%	χ^2/dof	Note[a]
ngc6101	0.00-0.84	5.74±0.46	3.21±2.01	2.71±0.81	73.0/ 69	g
	0.84-1.25	4.76±0.42	7.64±2.00	9.61±2.16	46.1/ 64	g
	1.25-1.72	4.21±0.40	6.47±2.01	10.84±1.38	46.2/ 61	g
ngc6121	0.00-0.20	5.49±0.82	-9.74±4.05	0.50±0.06	53.9/ 33	n
	0.20-0.30	2.87±0.80	-4.49±4.04	2.47±2.95	29.0/ 35	n
	0.30-0.41	4.11±0.94	-8.79±4.11	0.50±0.00	16.4/ 38	n
m13	0.00-0.50	5.00±0.34	1.26±1.28	1.24±0.43	113.3/120	d
	0.50-0.75	2.28±0.26	1.67±1.27	2.35±2.70	84.0/102	d
	0.75-1.04	1.65±0.21	2.52±1.27	2.71±0.62	86.8/ 90	g
ngc6218	0.00-0.47	3.41±0.45	3.80±2.35	2.35±0.67	51.6/ 59	g
	0.47-0.72	2.87±0.39	3.91±2.35	3.70±1.83	39.7/ 55	g
	0.72-1.00	3.08±0.40	2.75±2.36	4.44±2.31	54.4/ 57	g
ngc6341	0.00-0.75	5.79±0.40	2.66±1.24	2.35±0.44	113.5/121	d
	0.75-1.18	2.77±0.31	3.34±1.23	3.95±0.43	76.3/102	d
	1.18-1.74	2.43±0.25	3.69±1.23	4.44±1.73	104.0/ 87	g
ngc6352	0.00-0.43	1.31±1.24	-2.20±3.50	0.50±0.00	36.8/ 57	f
	0.43-0.64	1.97±1.52	2.14±3.77	1.48±3.55	36.9/ 54	f
	0.64-0.86	-4.64±1.85	-5.00±4.22	0.50±0.00	34.6/ 55	f
ngc6362	0.00-0.44	5.07±0.57	8.48±2.60	4.44±1.49	58.4/ 60	g
	0.44-0.65	3.90±0.52	7.41±2.61	7.39±2.70	28.4/ 56	g
	0.65-0.85	3.44±0.49	16.05±2.59	29.05±4.64	61.7/ 56	g
ngc6397	0.00-0.28	1.83±0.75	-0.18±3.27	0.50±0.00	36.4/ 46	g
	0.28-0.45	1.88±0.77	6.15±3.28	10.84±1.63	33.6/ 45	g
	0.45-0.61	4.16±0.92	0.48±3.36	20.19±7.12	43.3/ 49	g
ngc6541	0.00-0.71	4.92±0.39	2.80±1.39	2.59±0.72	97.4/111	d
	0.71-1.14	1.52±0.32	2.87±1.40	5.79±0.79	96.3/ 93	d
	1.14-1.66	0.86±0.32	11.95±1.40	19.70±1.41	177.0/ 87	g
ngc6624	0.00-0.91	0.93±0.61	12.57±2.10	7.51±0.68	64.2/ 86	f
	0.91-1.45	1.51±0.88	14.60±2.29	16.00±1.11	61.0/ 84	f
	1.45-2.13	2.15±1.34	10.50±2.69	21.42±2.71	73.2/ 90	f
ngc6637	0.00-0.87	4.90±0.46	2.16±1.84	1.12±0.83	102.9/ 96	f
	0.87-1.38	0.87±0.44	5.87±1.88	9.85±2.96	67.2/ 82	f
	1.38-2.15	-0.14±0.65	1.80±2.09	1.98±2.40	56.1/ 76	f
ngc6652	0.00-1.34	3.15±0.66	6.04±3.02	3.45±1.21	34.5/ 50	f
	1.34-2.34	1.54±1.06	0.27±3.48	4.44±2.87	28.7/ 48	f
	2.34-3.77	-4.18±2.18	-9.25±4.86	0.50±0.00	36.2/ 47	f
ngc6656	0.00-0.26	-1.01±0.47	-3.70±1.73	0.50±0.03	86.4/ 84	f
	0.26-0.39	-4.94±0.51	1.70±1.75	7.14±1.02	126.0/ 82	f
	0.39-0.52	-8.16±0.58	-0.51±1.82	8.37±1.04	168.6/ 80	f

continued on next page

continued from previous page

Source	Bin Range(r_h)	$f_b(q > 0.5)$%	$f_b(count)$%	$f_b(fit)$%	χ^2/dof	Note[a]
ngc6723	0.00-0.50	6.87±0.41	7.61±1.72	5.67±0.75	93.7/ 92	d
	0.50-0.80	3.81±0.32	2.83±1.74	4.31±1.15	115.5/ 79	g
	0.80-1.16	2.55±0.30	12.78±1.72	19.14±1.43	132.6/ 72	g
ngc6752	0.00-0.41	0.78±0.35	-1.48±1.90	0.52±0.03	77.4/ 75	g
	0.41-0.66	-0.06±0.26	1.30±1.88	0.50±0.06	70.2/ 65	g
	0.66-0.93	0.85±0.25	5.24±1.87	11.70±1.80	64.5/ 64	g
ngc6809	0.00-0.32	3.29±0.45	2.00±2.44	1.48±2.00	39.3/ 49	g
	0.32-0.47	2.99±0.46	1.85±2.44	4.44±2.15	35.7/ 48	g
	0.47-0.60	2.59±0.40	1.01±2.45	3.45±0.00	44.3/ 48	g
ngc6981	0.00-0.67	9.55±0.58	8.62±2.18	5.18±0.77	54.4/ 75	d
	0.67-1.12	3.60±0.40	3.55±2.20	3.95±3.95	41.2/ 66	g
	1.12-1.89	2.11±0.32	1.14±2.22	2.47±1.48	53.7/ 58	g
ngc7078	0.00-0.85	5.72±0.40	3.97±1.10	2.84±0.51	163.3/140	d,e
	0.85-1.25	3.11±0.31	2.45±1.09	2.41±0.76	136.9/122	d,e
	1.25-1.78	1.56±0.25	-5.58±1.12	0.50±0.00	252.2/107	d,e
ngc7099	0.00-0.64	5.12±0.70	-4.63±1.93	0.56±0.46	74.6/ 52	g
	0.64-1.11	1.39±0.47	3.73±1.94	5.91±2.15	43.0/ 42	g
	1.11-1.74	0.67±0.38	2.87±1.96	6.41±4.29	36.0/ 37	g
Arp2	0.00-0.49	6.65±0.94	0.83±3.85	6.41±2.20	13.0/ 28	g
	0.49-0.72	7.21±0.91	1.15±3.89	12.31±12.31	11.6/ 29	g
	0.72-1.02	10.38±1.08	-7.34±4.05	0.50±0.00	9.1/ 27	g
Palomar12	0.00-0.40	16.60±2.52	-37.87±8.55	0.50±0.00	2.2/ 13	n
	0.40-0.71	13.66±2.15	-22.56±8.15	0.50±0.5	1.5/ 13	n
	0.71-1.05	9.26±1.96	-8.86±7.91	8.37±8.37	3.6/ 13	n
Terzan7	0.00-0.86	17.38±1.58	6.61±4.57	6.41±2.20	13.0/ 28	n
	0.86-1.48	9.85±1.31	3.08±4.76	12.31±12.31	11.6/ 29	n
	1.48-2.35	7.94±1.26	-5.75±5.05	0.50±0.00	9.1/ 27	n

[a] Note: same as Table 3.1.

3.4 The Radial Distribution of the Binary Fractions

The analysis for the binary fractions at radial annular bins is also important, as it can diagnose any radial changes for the binary fractions. In Figure F.1 to F.35, we show the radial analysis results for each cluster. The panels on the left, middle, and right columns are for the inner radial bin, the middle radial bin, and the outer radial bin, respectively. For each column, the 1st to 5th rows are the same as the corresponding panels in Figure E.1 to E.35, only that the formers are for different radial bins. On the 6th row, the left panel shows the radial distribution of the binary fractions obtained through three different methods, high q method (black), star counting method (red), and χ^2 fitting method (green). The right panel shows the luminosity functions (normalized to the maximum number) at different radial bins, inner (black), middle (red), and outer (green).

From those figures, we can see that the quality of the CMDs changes dramatically for some dense clusters (e.g. NGC 1851), In those dense clusters, the inner radial bins usually have the worst photometric quality among the three bins, shown by larger spread of the main-sequence stars and fewer fain stars recovery. The outer bins, however, usually have very narrow main sequence on the CMDs, and produce much reliable results of binary fractions. For low density clusters (e.g. NGC 5053), the photometric quality is not so different among the three bins.

Another concern is that for the star counting and χ^2 fitting methods, the results are more scattered than using the whole field. This is because each radial bin only contains about one third of total stars, making the statistics worse. The analysis involving fitting process will be unable to constrain the model, which causes big errors in the binary fractions (see Figure 3.6 for binary fraction comparison among three methods). The high q method is the more reliable one when the star number is small.

We list all the results for each radial bin in Table 3.6. The tables are similar to

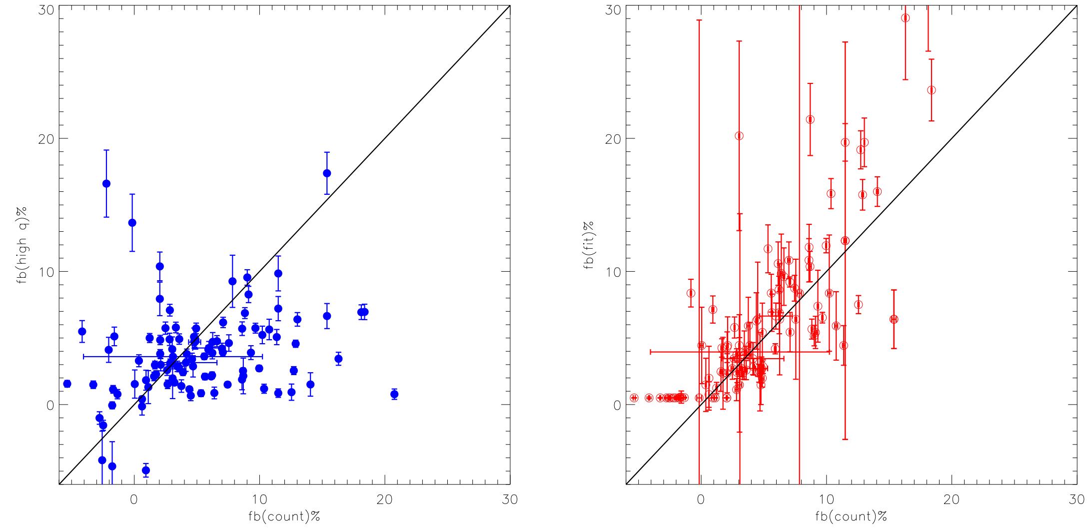

Figure 3.6: Same as Figure 3.1, but for all radial bin results.

Table 3.2, only that we add one column showing the size of each radial bin in terms of the half-light radius. Each cluster has three rows, showing the inner bin, middle bin, and the outer bin results, respectively.

In Figure 3.7, we plot all the high mass-ratio ($q > 0.5$) binary fractions at different annular bins from all the clusters in our sample verse their radial distance to cluster center. The upper panel is the high mass-ratio binary fractions normalized to their core fractions, and the distances are normalized to their core radii. Note that there are only 17 clusters with reliable core binary fractions measured in our sample. The straight line fitted results are shown in Table 3.7, first row, which shows a moderate correlation (slope $k = -0.41$). The Spearman R rank correlation coefficient, however, shows a significant correlation (coefficient $= -0.69$, with a highly reliable significance).

The lower panel in Figure 3.7 and the second row in Table 3.7 show the high mass-ratio binary fractions normalized to their half-mass fractions versus the distances normalized to their half-mass radii. The straight line fit shows a strong correlation (slope $k = -0.99$), which is confirmed by the Spearman R rank correlation coefficient (-0.61) with a highly reliable significance.

Table 3.7: Fitting results for binary fractions vs. radius.

normalize	k	b	χ^2/dof	coefficient$_r$	significance
to r_c and fb_c	-0.41±0.04	1.34 ± 0.07	286.5/64	-0.69	1.9e-10
to r_h and fb_h	-0.99±0.08	1.45 ± 0.06	288.3/100	-0.61	7.4e-12

This correlation (fb Vs. r) is very important, as it confirms the mass segregation effect in globular clusters. Both the recent Monte Carlo and the N-body simulations predict the binary fraction distribution along the cluster radii (see Fregeau et al. (2003), Hurley et al. (2007), and Sollima (2008)), which show that after several half-mass relaxation times, binaries tend to sink to the core of a cluster. The single stars at the core region, however, drift outwards of clusters, which makes the binary fraction at the core region increases. The outer region, on the other hand, decreases in both binaries (sinking to the center) and single stars (due to evaporation), making the binary fraction in the outer region roughly unchanged (Hurley et al., 2008). Thus the binary fractions will decrease against the radii. Sollima et al. (2007) also observed this trend with 7 clusters. Here, we confirmed this relationship with a larger sample (34 clusters in the plot, or 102 annular bins), which gives a robust fit.

3.5 The Catalog for the High Mass-ratio Binary Candidates

Direct search of binaries (by studies of radial velocity variables or eclipsing binaries) and constructing a large binary sample in globular clusters are really challenging. The key problem is that most surveys are not efficient to discover binaries. For instance, in a recent spectroscopic binary survey for globular cluster M4 (= NGC 6121) by Sommariva et al. (2009), where they monitored stars from the red giant tip to the main sequence (one magnitude below the turn-off point), 57 binaries out of 2469 stars were discovered, or a 2.3 % binary discovery rate. The binary discovery rate might be higher in open cluster, e.g. for the open cluster Hyades, Griffin et al. (1988) performed a radial-velocity survey for more than 400 stars including the main sequence.

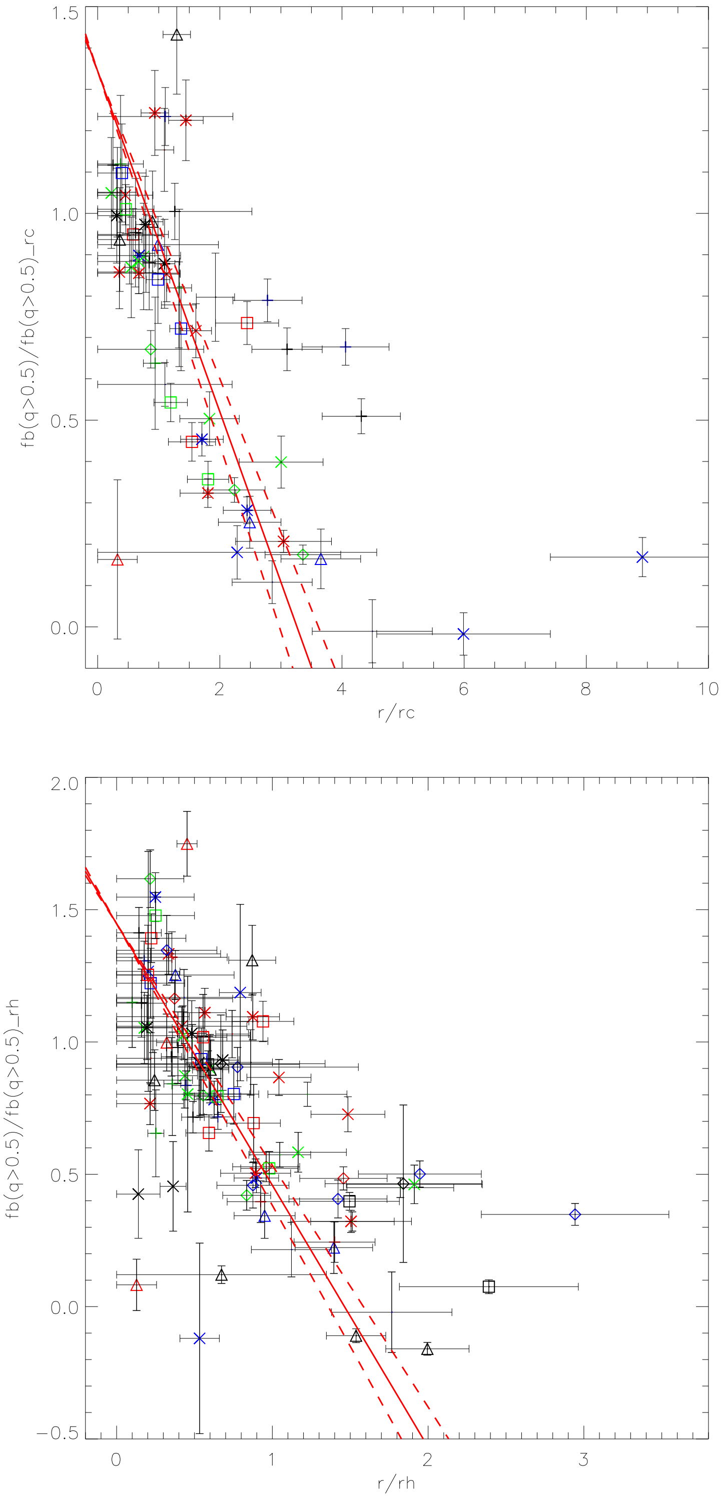

Figure 3.7: Combined high mass-ratio ($q > 0.5$) binary fractions Vs. radius. Each cluster has three bins, and with the same symbol and the same color on this figure.

They found that about 30% of stars are binaries after excluding field stars. But as long as the main sequence stars (mostly are single stars) are included, most of the survey time will be wasted on monitoring single stars.

Observing stars on the second sequence above the main sequence on the CMDs, however, is a very efficient way to search for main-sequence binaries. Bolte (1991) tested this method in open stellar cluster Praesepe (= M44, NGC 2623), where he observed 17 stars above the main sequence through the radial velocity study, and found that 10 out of 17 (or 59 %) stars are demonstrably binary systems. If we can apply this method to globular clusters, monitoring 5000 stars can yield more than 3000 binaries, which will provide valuable and reliable information about the properties of binaries in globular clusters, such as the period distribution (or the separation distribution). Combining with binary mass-ratio distribution, one can calculate the binary hardness distribution, which is a key input parameter in the theoretical model in the dynamical evolution of globular clusters.

3.5.1 Selecting Criteria

One product of this thesis work is to produce such binary candidate catalog for future observations. With the highly accurate CMDs obtained by HST observations, we can select those potential main-sequence binary candidates from their CMDs. To do this, we use the following criteria.

1) The Galactic latitude for the cluster is not within ±15°, so that there are not many field star contaminations. This rules out 9 clusters in our sample.

2) The magnitude range starts from one magnitude below the turn-off point, and goes 2 to 3 magnitudes down the main sequence. Stars are not selected too close to the turn-off point because around that area, binaries are merging with the main sequence, making the binary sequence indistinguishable. We do not

choose stars that are too faint, because the photometric errors will be too large to hide those binaries.

3) We only select those binaries with mass-ratio greater than 0.5 and less or equal to 1. Those low mass-ratio binaries are too close to the main sequence even for bright stars.

4) For low density clusters, we use the whole field of view of ACS images, because the photometries are equally good from the center region to the outside. For high density clusters, however, we only use the outer bin. For some really dense clusters (e.g. NGC 104, M3, and NGC 7078), even the outer bin is too dense, making the CMD too scattered for a clean selection of binaries. In those cases, we do not include them in the catalog.

3.5.2 The Catalog

By the criteria discussed in 3.5.1, we selected a total of 6,004 high mass-ratio ($q > 0.5$) binary candidates from 23 clusters in our sample. In Figure 3.8 to 3.10, we plot the binary candidates (red circles) on their CMDs (main-sequence stars as black circles), as long as the MSRL (green line), 0.5 mass-ratio line (blue line), and equal-mass binary line (red line). We also list the selected region (e.g. all field of view, middle and outer bins, and outer bin only) and the number of binaries selected on each figure. From all those figures we can see that, those high mass-ratio binary candidates are well separated from the main sequence stars with few field stars contaminated. As they are all from low density regions, the rate of star superposition is fairly low (less than 0.05%). There should be very high probability that they are binaries.

In Appendix G, we list all the binary candidates in tables for each selected cluster, including their RA and Dec, magnitudes for F606W and F814W filters, and distance to the cluster center in arcsecond.

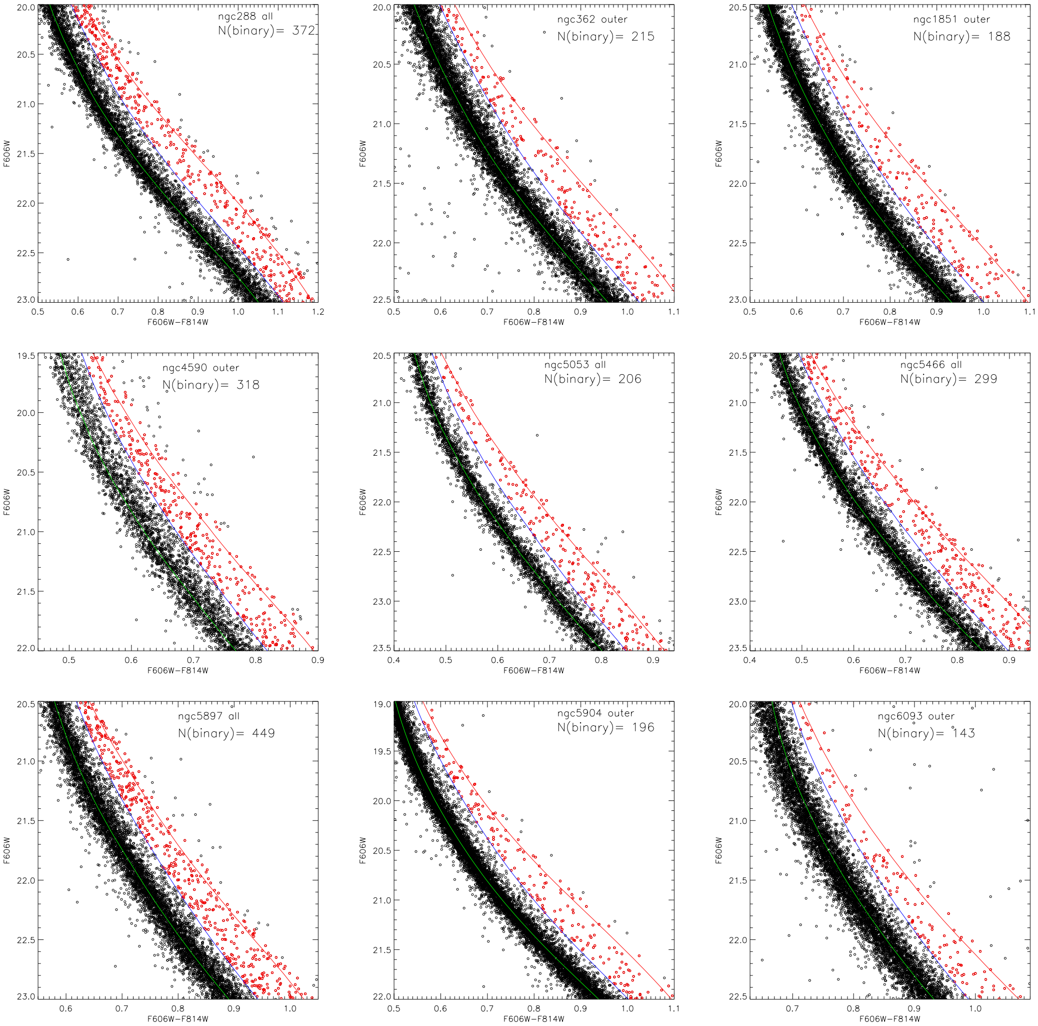

Figure 3.8: The CMDs for selecting high mass-ratio binary candidates.

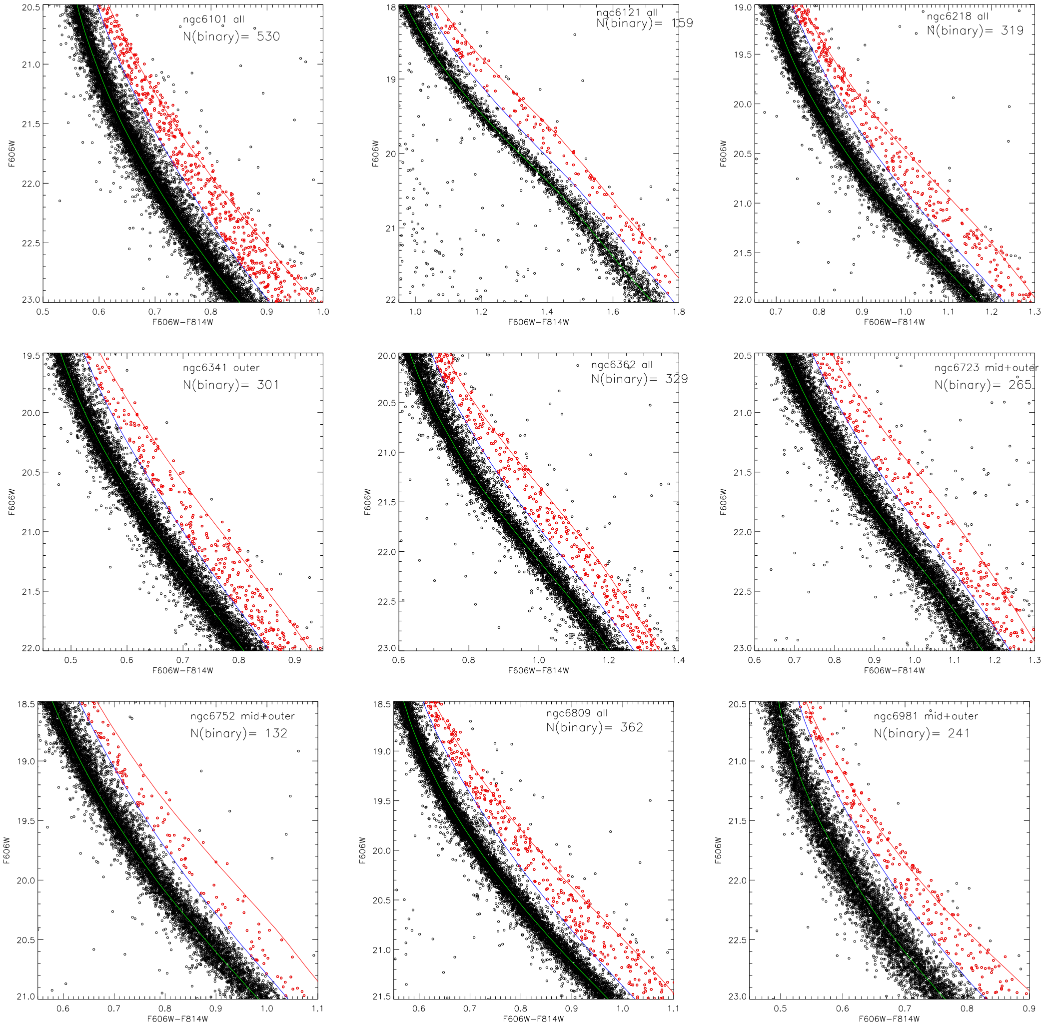

Figure 3.9: The CMDs for selecting high mass-ratio binary candidates (continued)

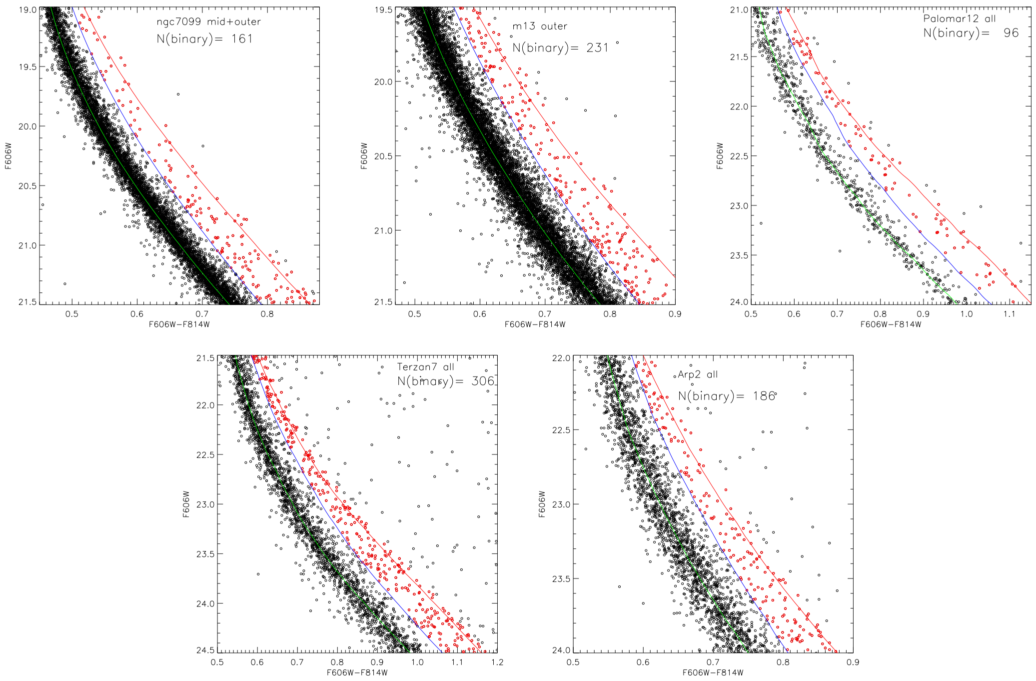

Figure 3.10: The CMDs for selecting high mass-ratio binary candidates (continued).

3.5.3 The Properties of the Binary Candidates

To pre-examine those binary candidates, we plot some of their property distributions in Figure 3.11. On the upper left panel, we plot the distribution of their absolute magnitudes in the F606W band, which were corrected by their distance modulus and reddening. On the upper right panel, we plot the residual color distribution of those binaries (i.e. the colors of binaries minus the colors of their MSRL). On the lower panel, we show the binary surface brightness distribution (absolute magnitude per r_c^2), Vs. radial distance to the center in terms of the core radius (r_c). The red curve is the fitted model from Equation 3.2,

$$S(r) = S(0) + 2.5lg(1 + r^n), \tag{3.2}$$

where S(0) is the center surface brightness, and r is in unit of the core radius r_c. The fitted parameters are S(0) = -0.44 and n = 3.58, with $\chi^2/dof = 472/307$. Note that,

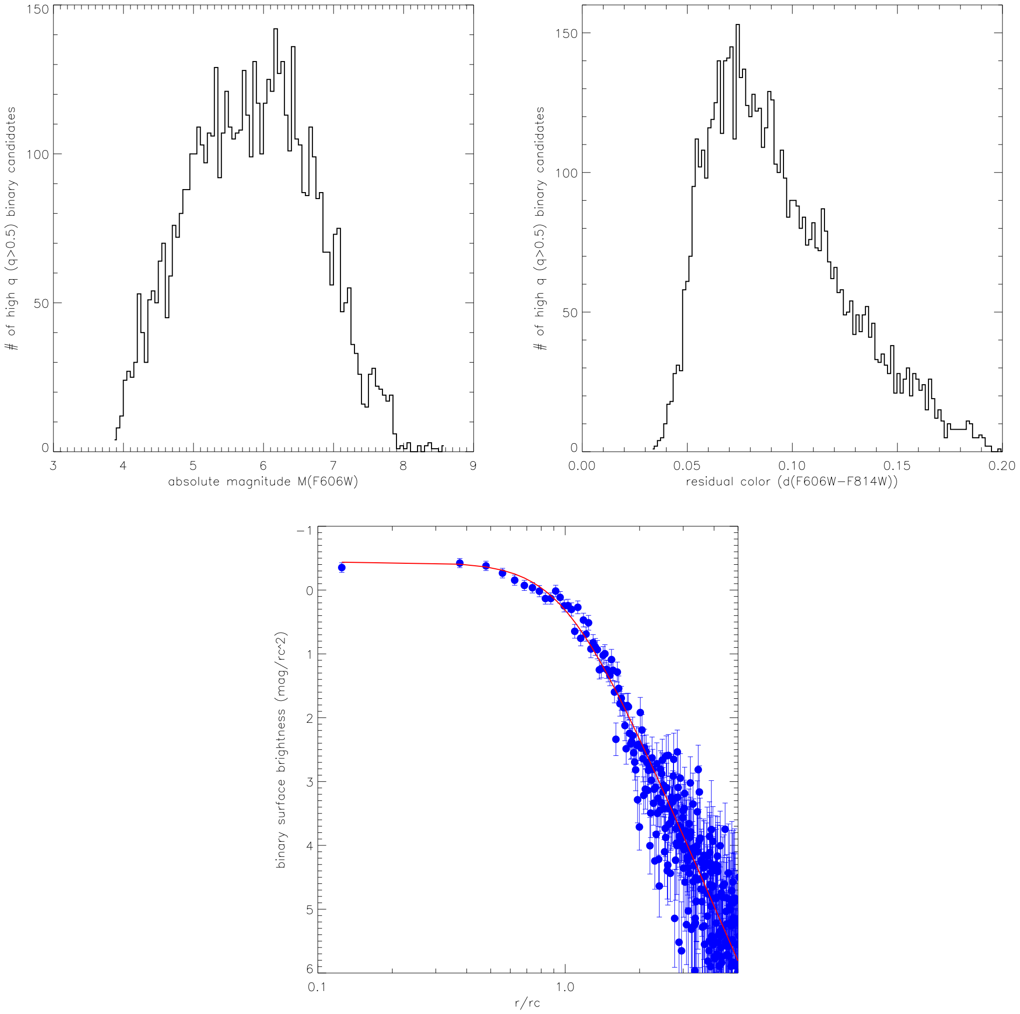

Figure 3.11: Properties of the high mass-ratio binary candidates in the catalog. Upper left: binary candidates absolute magnitude distribution. Upper right: residual color distribution; Lower panel: binary candidates surface brightness profile with model fitted.

the single star surface brightness profile usually follows the King's model (King, 1962, 1966) with the index n equal to 2. The reason that the binary surface brightness profile differs from the single star surface brightness profile is unknown. But this profile again shows an independent evidence that there are more binaries towards the cluster centers than outward, which is the result of the mass segregation effect.

CHAPTER 4

Summary and Future Work

4.1 Summary

4.1.1 Summary of the Methodology

I used the photometric binaries method on CMDs to determine binary fractions for a sample of 35 Galactic globular clusters, which covers a wide range in the dynamical ages and metallicity. Those CMDs were constructed with the PSF photometry by Dolphot (V1.2) from their HST ACS archival data. Three different methods to measured the binary fractions were introduced, the high mass-ratio ($q > 0.5$) method, the star counting method, and the χ^2 fitting method. For each method, I constructed the models for the blending stars and field stars. A single star model was introduced to the star counting method, while additional binary model was applied to the χ^2 fitting method. I also discussed the method to perform radial analysis of binary fractions. Finally, I discussed the other errors that can affect the accuracy of the binary fraction measurement.

4.1.2 Summary of the Results

In Section 3.1 to 3.5, we showed and discussed the results for this sample, which includes analysis within full field of view, within the core and the half-mass radius region, within radial annular bins, and with the high mass-ratio binary candidates.

We analyzed each cluster with three different methods (the high mass-ratio method, the star counting method, and the χ^2 fitting method) and for different types of regions. We found that binary fractions obtained by the star counting method and the χ^2 fitting method are consistent with each, but are systematically higher than the high mass-ratio method, which shows that the former two methods can statistically recover part of the binary signals even within the main sequence. The mean binary fractions within the whole field of view from the three methods are: 5.2% (high q), 6.3% (star counting), and 7.3% (χ^2 fitting), respectively. We also constrain the binary mass-ratio distribution function with the χ^2 fitting method (assuming a power-law function $f \sim q^x$), with an average power index x of -1.9 ± 1.1 and a minimum binary mass-ratio of 0.30 ± 0.06.

For binary fractions within the core and the half-mass radii, we obtained the mean binary fractions with the high mass-ratio method: 7.0% and 5.6%, respectively. We also examined the correlations between the binary fractions and different cluster properties among the clusters in our sample. We found that the half-mass binary fractions correlate with the cluster ages and their absolute V magnitudes, but not with their dynamical ages or their [Fe/H]. The core binary fractions also correlate to the cluster ages, but not with their dynamical ages, [Fe/H], or absolute V magnitudes. We also found a significant distribution of the binary fractions along the cluster radii, with binary fractions increasing towards the cluster centers. This is the evidence that the mass segregation effect has an impact in distributing stellar masses inside the globular clusters.

Finally, we compiled a catalog consisting of 6,004 binary candidates with mass-ratio greater than 0.5 from 23 Galactic globular clusters in our sample. Those binaries are well separated from the main-sequence stars, and are selected from low density regions and high Galactic latitudes. The contaminations from photometric errors, blending stars, and field stars are very small. With this binary candidate catalog, people can search for the main-sequence-main-sequence binaries very efficiently in globular clusters through future radial velocity studies. We also found a binary candidates radial distribution pattern through their surface brightness profile, with increasing binary number towards the cluster center, which is a separate evidence for the mass segregation effect in globular clusters.

4.2 Future Work

4.2.1 Improvement for the PSF Fitting Program

The aperture and PSF photometry both work very well in low stellar density clusters. But when the stellar density becomes larger, the aperture photometry becomes hard to recover faint stars. At some high density region, even the PSF photometry would not work, due to too high background and large uncertainty. The better PSF algorithm to recover stars in very dense region is still not mature, making determinations of binary fractions in core region for some clusters difficult.

4.2.2 Proper Motion to Screen Field Stars

For low galactic clusters, field stars are the main contamination source when determining the binary fractions. The uncertainties are mainly from the contribution of field stars. The best way to clearly remove non-member stars is to use proper motion method, which requires more observations separated by at least 1 year. NGC6397 and M4 are currently the best examples with this method (see Davis et al. (2008) and Richer et al. (2004)). There are 9 globular clusters in our sample with galactic latitude within $\pm 15^\circ$. We need more HST observations to screen out those field stars, and constrain the binary fractions of them.

4.2.3 Studies with the Ground-based Telescopes

Binary study based on CMDs is only a statistical way to study the overall properties of binary fractions. The direct way to study the binaries in globular clusters is to use radial velocity observations, which can provide much valuable information on the properties of the binary systems in globular clusters, such as period distribution. Combining with the binary mass-ratio distribution, we can obtain the binary hardness distribution, which is a key input parameter in the simulations of the dynamical evolution of globular clusters. This thesis provides such binary candidate catalog for future studies with ground based telescopes. This requires huge amount of observing time for the survey, and some are very challenging to observe even by today's technology. But as long as we can obtain such a large sample of binaries in globular clusters someday, we will be able to see how dense stellar environment would affect the evolution of binaries.

4.2.4 Studies on the White Dwarf Populations

The binary fractions measured here are main-sequence-main-sequence binaries. They consist only 23% of total true binaries (Fregeau et al., 2009), which will give us an estimate of the total core and half-mass radius binary fractions of at least 30.4% and 24.3%, respectively. The majority of binaries are in forms of white-dwarf-main-sequence (44%) and white-dwarf-white-dwarf (32%) binaries. If this simulation is true, white dwarf population will be the majority components in globular cluster binaries. By studying the basic properties of white dwarfs through CVs or isolated white dwarfs in globular clusters by HST and X-ray telescopes, we can gain more insight in globular cluster binaries.

4.2.5 Correlation of Binary Fractions with X-ray Point Source Frequencies in Globular Clusters

Since binaries can dramatically affect the globular cluster evolutional path, there should be certain correlation between the binary fractions and the X-ray point source frequencies. We can study this by classifying those X-ray point sources first, into LMXBs, CVs, ABs, and MSPs. Since the ABs and part of CVs are thought to be primordially formed, they should be correlated with the main-sequence-main-sequence binary fractions obtained here. The LMXBs and MSPs are dynamically formed. They can be scaled with the close encounter rate, which should be anti-correlated with the binary fractions, as higher close encounter rate indicating higher destroying/escaping rate for binaries. By systematically analyzing archival X-ray source catalog in globular clusters or published results, we should be able to answer those questions.

APPENDICES

APPENDIX A

Discussions on Hard Binaries and Planets in Globular Clusters

Binary fraction is a critical parameter in globular cluster evolution, since their binding energy can be a heating source to other stars to prevent core collapsing. But only hard binaries will heat up other stars during interactions and become harder, while most soft binaries will be disrupted during their first interactions with other stars. This gives us a question how many binaries we detect by CMD method are actually hard binaries. Also, how many binaries we detect by radial velocity method are hard binaries.

1) **Binary Binding Energy:** The energy needed to give the system in order to disrupt it, i.e. become physically unbound (the total energy of the system to be greater than 0).

   e.g. Two stars with the same mass of M are in a circular orbit with a separation of r. Thus the total energy of this system is E_t:

$$\begin{aligned} E_t &= V + K \\ &= -\frac{GM^2}{r} + Mv^2 \\ &= -\frac{GM^2}{2r} \end{aligned} \tag{A.1}$$

Here we use the circular orbit motion:

$$F = \frac{GM^2}{r^2} = \frac{Mv^2}{r/2} \tag{A.2}$$

So

$$v^2 = \frac{GM}{2r} \tag{A.3}$$

Since the total energy of this system E_t is less than 0, which is bound, in order to disrupt this system, we need to provide an energy of at least $-E_t$ to make the total energy no less than 0. Thus the binding energy for this system is:

$$E_b = -E_t = \frac{GM^2}{2r} \tag{A.4}$$

Notes:

1. Binaries with larger binding energy are harder to disrupt.
2. From Equation A.4, we see that the binary binding energy depends on masses of the two stars as well as their separation. If they have larger masses, and smaller separation, the binary system will have larger binding energy.
3. From Equation A.3, we see that binaries with larger separations will have smaller orbital velocity.

4. In order to have the same binding energy as the large mass binaries, low mass binaries should have smaller separations. For example, a binary system containing two stars with masses 1 $M_\odot$ and 0.08 $M_\odot$ (brown dwarf) should have a separation of 1.6 AU in order to have the same binding energy as the binary system which contains two stars with the same mass of 1 $M_\odot$ and a separation of 20 AU.

5. For binaries with different masses, the binding energy still has similar form as Equation A.4,

$$\boxed{E_b = \frac{GM_1M_2}{2r} \qquad \text{(A.5)}}$$

This can be derived from the following equations:

$$F = \frac{GM_1M_2}{r^2} = M_1\omega^2 r_1 = M_2\omega^2 r_2 \tag{A.6}$$

where

$$r = r_1 + r_2 \tag{A.7}$$

$$M_1 r_1 = M_2 r_2 \tag{A.8}$$

From Equation A.6, we have:

$$r_1 = \frac{GM_2}{r^2\omega^2} \tag{A.9}$$

$$r_2 = \frac{GM_1}{r^2\omega^2} \tag{A.10}$$

So the binding energy E_b is:

$$
\begin{aligned}
E_b = -E_t &= -(V+K) && \text{(A.11)}\\
&= \frac{GM_1M_2}{r} - \frac{1}{2}M_1\omega^2 r_1^2 - \frac{1}{2}M_2\omega^2 r_2^2 && \text{(A.12)}\\
&= \frac{GM_1M_2}{r} - \frac{1}{2}M_1\omega^2 r_1^2 - \frac{1}{2}M_1\omega^2 r_1 r_2 && \text{(A.13)}\\
&= \frac{GM_1M_2}{r} - \frac{1}{2}M_1\omega^2 r_1(r_1+r_2) && \text{(A.14)}\\
&= \frac{GM_1M_2}{r} - \frac{1}{2}M_1\omega^2 \frac{GM_2}{r^2\omega^2} r && \text{(A.15)}\\
&= \frac{GM_1M_2}{r} - \frac{GM_1M_2}{2r} && \text{(A.16)}\\
&= \frac{GM_1M_2}{2r} && \text{(A.17)}
\end{aligned}
$$

6. By adding Equation A.9 and A.10, we have:

$$\frac{G(M_1+M_2)}{r^2\omega^2} = r_1 + r_2 = r \qquad \text{(A.18)}$$

So

$$\frac{r^3}{P^2} = \frac{G(M_1+M_2)}{4\pi^2} \qquad \text{(A.19)}$$

Here, P is orbital period, and we have replaced ω with P by $\omega = 2\pi/P$.

If we use units of $M_\odot$, AU, and *year* for mass, separation, and period, respectively, then we can get the simple relation between separation and period (this is valid even for elliptical orbits):

$$\boxed{\frac{r^3}{P^2} = M_1 + M_2 \qquad \text{(A.20)}}$$

2) Hard Binaries: By definition, a hard binary system is defined when the system's binding energy is $\gg kT$. Here the mean stellar kinetic energy of a globular cluster is $\frac{3}{2}kT$. We can derive some meaningful results as followed.

Since the mean stellar kinetic energy of a globular cluster is $\frac{3}{2}kT$, also is $<\frac{1}{2}Mv^2>$. So we have

$$\frac{3}{2}kT =< \frac{1}{2}Mv^2 >= \frac{1}{2} < M >< v^2 >= \frac{1}{2} < M > \sigma^2 \tag{A.21}$$

Here,$< M >$ is the mean stellar mass, and σ is the velocity dispersion of globular cluster. So, we have

$$kT = \frac{1}{3} < M > \sigma^2 \tag{A.22}$$

Since a hard binary system has the binding energy much greater than kT, so with Equation A.3, we have

$$E_b = \frac{GM^2}{2r} = Mv^2 \gg kT = \frac{1}{3} < M > \sigma^2 \tag{A.23}$$

or

$$v \gg \sqrt{\frac{< M >}{3M}}\sigma. \tag{A.24}$$

So for a equal-mass binary system, if its orbital velocity v exceeds the velocity dispersion σ of the globular cluster, it is definitely a hard binary. From Equation A.24, we also know that less massive binaries need to have higher orbital velocity to become hard binaries.

With Equation A.5, we also have

$$E_b = \frac{GM_1M_2}{2r} \gg kT = \frac{1}{3} < M > \sigma^2 \tag{A.25}$$

So hard binaries should have separation

$$\boxed{r \ll \frac{3GM_1M_2}{2 < M > \sigma^2} \quad (A.26)}$$

3) Example: Galactic globular cluster M4 has a velocity dispersion $\sigma \sim 9.8km/s$. Assuming $< M >= 1M_{\odot}$, a binary system with two stars having the same mass of 1 $M_{\odot}$ should have a separation at most of 13.3 AU in order to be hard binary system. This binary system would have a maximum period of 34.4 years. If one of the binary star is a brown dwarf with a mass of 0.08 $M_{\odot}$, then this system should have a maximum separation of 1.06 AU in order to be hard one. This would give a maximum period of 1.06 years. If one of the binary star is a Jupiter-like planet with mass of $10^{-3}M_{\odot}$, it should not exceed 0.013 AU, which is far less than the Mercury orbit of 0.387 AU. The maximum period would be 13.0 hours. If one of the binary star is an Earth-like planet with mass of $3 * 10^{-6}M_{\odot}$, it should not exceed $4 * 10^{-5}$ AU, which is far less than the radius of the Sun of $4.64 * 10^{-3}$ AU. This is impossible for non-degenerate primaries, but possible for degenerate ones, such as white dwarfs and neutron stars.

Those calculations give us a clear picture that those primaries (non-degenerate stars) with planets would not provide heating energy during interactions with other stars, but would be disrupted because of their small binding energy. From Figure A.1, we show that for the 228 extra-solar planets published by Wright et al. (2011), only 4 (1.75%) could be qualified as hard binaries. So we make a further conclusion that most planet systems would be disrupted when their first interactions with other pass-by stars in globular clusters, which make the globular clusters an unlikely place to search for extra-solar planets. Weldrake et al. (2007) searched for hot Jupiter planets in 47 Tuc and ω Cen with HST observations, but none are detected in either clusters. M4, however, was de-

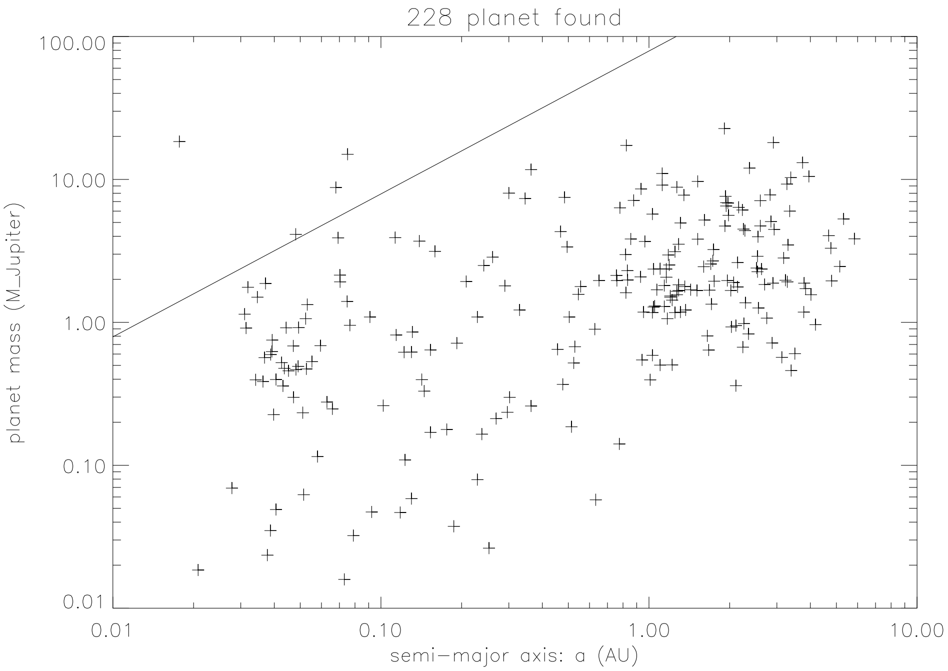

Figure A.1: Semi-major axis VS. planet minimum mass for 228 extra-solar planets published by Wright et al. (2011). The solid line is the one above which the binary system is a hard one assuming a dispersion velocity of 9.8 km/s for globular clusters.

tected a pulsar with several planets (Sigurdsson, 1993; Richer et al., 2003; Beer et al., 2004).

APPENDIX B

Estimate and Simulations of Superposition of Stars

The Superposition of stars is a contamination that has the exact same effect as real binaries on CMD. It is very difficult to screen them, but statistically, we can estimate the number of blended stars. In this appendix, we will discuss the probability for different types of blending stars (i.e. unresolved doubles, triples, etc.) in globular clusters, which can provide a good estimate on the blending frequency for globular clusters at different stellar density.

1) Poisson Distribution

The probability that one star is blended with others depends on the projected 2D star number density as well as the angular resolution. It is like Poisson process and the probability can be described by the Poisson probability distribution function:

$$P(x) = \frac{\mu^x e^{-\mu}}{x!}$$

where x is the companion number for the blends, i.e. $x = 1$ is for unresolved double stars (star with one companion), and $x = 2$ is for unresolved triple stars (star with two companions), etc. μ is the area ratio of the minimum resolved area to the mean occupied area per star in the reference frame.

2) Monte Carlo Blending Test

To test the hypothesis that blending probability can be described by Poisson distribution function, we performed the following Monte Carlo simulations. Firstly, We randomly distributed N_{total} stars in a fixed square area with each size of 100 pixels to form the reference frame. Secondly, we randomly added one test star to this reference frame. Then we counted how many reference stars are within the minimum resolution radius r_{min} of the added test star, where $r_{min} = 1$ to simulate the ACS image. If the count is more than 0, then the added test star will be considered as a blend. After counting, the test star was removed, and a new test star was randomly added to follow the above process. We added 5000 test stars in all for each simulation, and the final blending fraction is the total number of the blending stars divided by the total number (5000) of added test stars. Note that, blends with different companion number were counted separately. We repeat this simulation 30 times (i.e. 30 different random distributions of the reference stars) for each star number density (i.e. each N_{total}) to get the mean blending fraction and the standard deviation. The simulation setup is shown in Figure B.1.

Results were then compared to the Poisson probability distribution function (see Figure B.2), where μ is defined as

$$\mu = \frac{A_{min}}{A_{mean}} = \frac{\pi * r_{min}^2}{L^2/N_{total}} = \frac{\pi * r_{min}^2}{L^2} * N_{total}.$$

So for the fixed area with size L and the minimum resolution radius r_{min}, μ only depends on the input star number N_{total}.

Here we calculated the blending probability for three different blending stars, $x = 1$ (unresolved double stars), $x = 2$ (unresolved triple stars), and $x = 3$ (unresolved quadruple stars), and compared to the Monte Carlo simulations (Figure B.2). In Figure B.2, we can see that the Poisson distribution curves match those MC data points fairly well. This indicates that as long as we know the projected star number density and the minimum resolution, we can estimate the blending fraction using the Poisson distribution function.

For example, in our globular cluster sample, the maximum star number density is from NGC 7078, where we obtain 156,080 stars down to the 26th magnitude in the HST ACS CCD with the size of 4096 by 4096 pixels, which is equivalent to around 90 stars in the 100 by 100 pixel area of our Monte Carlo simulation setup (see the blue vertical dot-dash line in Figure B.2). Even for this densest cluster, the blending fraction with one companion is less than 3%, and the blending fraction with two companions is even smaller, less than 0.04%. The typical star number recovered in our cluster sample is around 30,000 stars, which is equivalent to around 17 stars in the 100 by 100 pixel area. The blending fraction is less than 0.7% for blends with one companion, which is only a small fraction in the total binary fraction budget. Blending fraction with higher number of companions is two orders of magnitude smaller.

Note that here we used the average star number density to calculate the blending fraction for the whole field, which is not appropriate, as in globular clusters the star number density varies quickly along the radius. But as long as we only consider small range of radius, the density gradient will be small, and one can use this method to estimate the blending fraction in that area. The blending model in the fitting process, however, takes into account for the star number density gradient, as it follows the observed stellar radial distribution, i.e. it generates more stars in the center than in the outside.

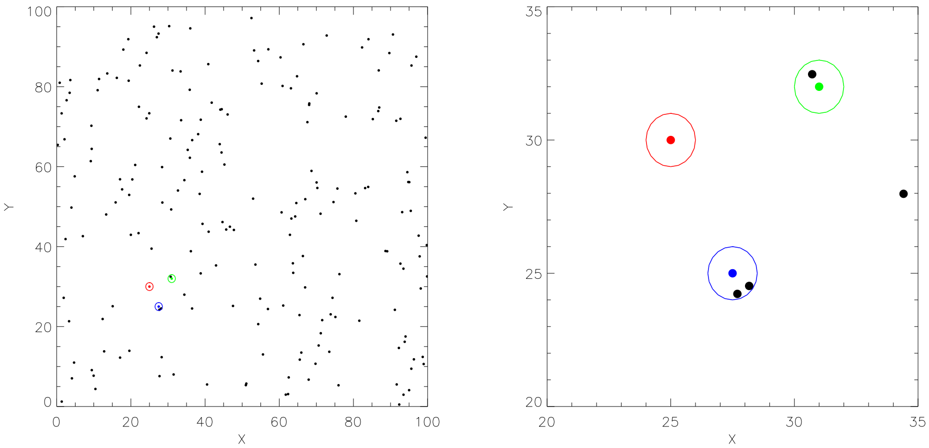

Figure B.1: Monte Carlo simulation rules for determining the frequency of blending of stars. Left: the black dots are randomly input reference stars ($N_{total} = 200$), while the color dots are randomly added test stars with a minimum resolved area within the circles. Right: zoom-in plot for the test stars. Red: added test star without a companion (not a blend); Green: added test star with one companion; Blue: added test star with two companions.

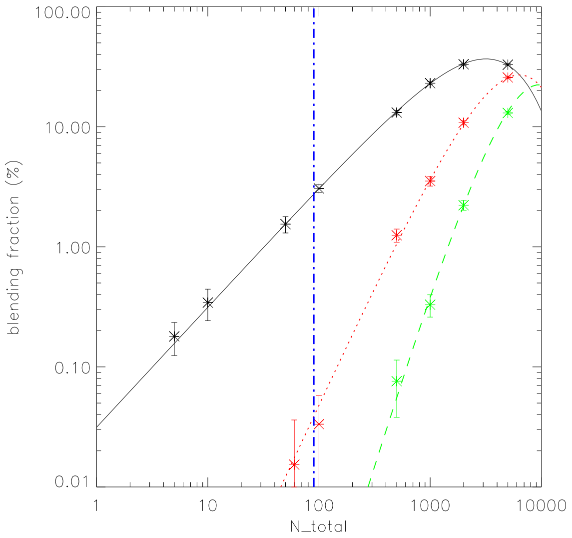

Figure B.2: Monte Carlo simulation results for the blending effect. Each data point is the mean of 30 MC simulations with the standard deviation as the error bars. The underlying lines are the predicted Poisson distribution. Black solid line: blending fraction for blends with one companion; Red dotted line: blending fraction for blends with two companions; Green dashed line: blending fraction for blends with three companions. The blue vertical dot-dash line is where the maximum star number density cluster is in our cluster sample. The error bars for the data points with large N_{total} are much smaller than the symbol size.

APPENDIX C

Error Estimate for Binary Fractions

In this appendix, we give the derivation of the error estimation for binary fractions discussed in Section 2.4 and 2.5.

First, we have the error propagation formulas:

$$\sigma(\frac{x}{y}) = \frac{x}{y} \times \sqrt{(\frac{\sigma x}{x})^2 + (\frac{\sigma y}{y})^2}$$

In high mass-ratio binary method,

$$x = n^B_{binary} - n^B_{blend} - n^B_{field} - n^R_{residual}. \tag{C.1}$$

So

$$\begin{aligned} \sigma x &= \sqrt{(\sigma n^B_{binary})^2 + (\sigma n^B_{blend})^2 + (\sigma n^B_{field})^2 + (\sigma n^R_{residual})^2} \\ &= \sqrt{n^B_{binary} + n^B_{blend} + n^B_{field} + n^R_{residual}} \end{aligned} \tag{C.2}$$

Here we have assumed the Poisson distribution for star counting at different regions, so $\sigma n = \sqrt{n}$. Similarly, for y, we also have

$$y = n_{total} - n_{field} \tag{C.3}$$

and

$$\sigma y = \sqrt{n_{total} + n_{field}}. \tag{C.4}$$

So

$$\sigma(\frac{x}{y}) = \frac{x}{y} \times \sqrt{\frac{n^B_{binary} + n^B_{blend} + n^B_{field} + n^R_{residual}}{x^2} + \frac{n_{total} + n_{field}}{y^2}}, \tag{C.5}$$

where x and y are defined by Equation C.1 and C.3.

In C.5, we can see that, when the number of blending stars or field stars increases, the error of binary fraction $\sigma(\frac{x}{y})$ will increase. When the photometric error increases, the number of residual stars $n^R_{residual}$ will increase, which also increase the error of binary fraction. So the error estimating formulas C.5 reflects the contaminations from the field stars, blending stars, and photometric errors.

APPENDIX D

The Effect of the Stellar Initial Mass Function of Globular Clusters on the Binary Mass-ratio Distribution

The mass-ratio function of binaries in globular cluster is a critical factor in determining the binary fraction f_b, but it is still uncertain for its form based on the current observations of globular cluster binaries. Since binary formation has two main ways, one through capture, and the other through primordial formation together. The first way to form binaries is not very common in low stellar density region, like field stars or even the early stage of globular clusters, but becomes more frequent at the core region during the core collapse phase. Current observations show that degenerate stars (such as neutron stars and white dwarfs) tend to capture other stars through dynamical interactions when the stellar density is high. The second way, on the other hand, is more likely for most of field binaries and the primordial binaries in globular clusters. Thus the initial mass function of globular cluster is essential to determine the mass-raio function of binaries.

Method:

1. We adopt the power law form of IMF:

   $$\xi(M) = C * M^{-\alpha} \tag{D.1}$$

   where C is a normalization constant.

2. We consider the mass range of $0.078 \sim 1.0\ M_{\odot}$. This is because the lower end, $0.078\ M_{\odot}$, is the brown dwarf mass upper limit, while the upper end, $1.0\ M_{\odot}$, is the most massive stars that are about to leave the main sequence. Since the average age of Galactic globular clusters is 11.5 ± 1.3 Gyrs, while the main sequence life time of a $1\ M_{\odot}$ star is around 10 Gyrs, so for almost all the Galactic globular clusters, we are seeing stars with mass below $1.0\ M_{\odot}$ which are still in the main sequence region. This range gives a minimum mass-ratio of 0.078 in binary systems.

3. By considering different IMFs, we adopt the following index α:

   i) α in the range of [-2,3] with 0.5 increment, which will give a grid show of the change in the resulted binary mass-ratio distribution.

   ii) $\alpha = 1.35$. This is the Salpeter IMF (Salpeter, 1955), which is steep at low mass end (generates much more low mass stars than high mass ones).

   iii) $\alpha = 0.3$. This is the mean power index for low concentrated clusters obtained from De Marchi et al. (2007), who studied 20 Galactic globular clusters that have index α measured in the mass range of $0.3 \sim 0.8\ M_{\odot}$. The mean power index for high concentrated clusters from their work is 1.4, close to the Salpeter IMF.

4. A binary system is created by random association of any two stars extracting from the assumed IMF. By doing this, we actually make an assumption that

any stars formed in globular clusters all follow the same IMF, including stars in binaries.

5. We generate 200,000 stars from the given IMF, and randomly associate them to form 100,000 binaries, in which we make the masses of the primaries greater than the secondaries to ensure the mass ratio q in the range of (0,1]. Then we plot the initial mass function distribution with the assumed power index α as well as the resulted binary mass-ratio distribution from such IMF in Figure D.1 and D.2.

Conclusions: In this simulation test, we can see that:

1. The IMFs have impact on the binary mass-ratio distribution if assuming that the primordial binaries are formed through random association. By adopting different IMFs, we can generate different binary mass-ratio distributions.
2. When the index power α equals 0 and 2.0, the resulted binary mass-ratio distribution tends to be flat. When α is less than 0 or is greater than 2.0, the binary mass-ratio distribution tends to peak at 1.0. When α is between 0 and 2.0, the binary mass-ratio distribution tends to peak at low q, around 0.2.
3. From Section 3.1, we constrained the binary mass-ratio distribution to be like what peaks at low q. This indicates that the power index α for the IMF of the Galactic globular clusters is probably between 0 and 2.0, which favors more on the Salpeter IMF ($\alpha = 1.35$).

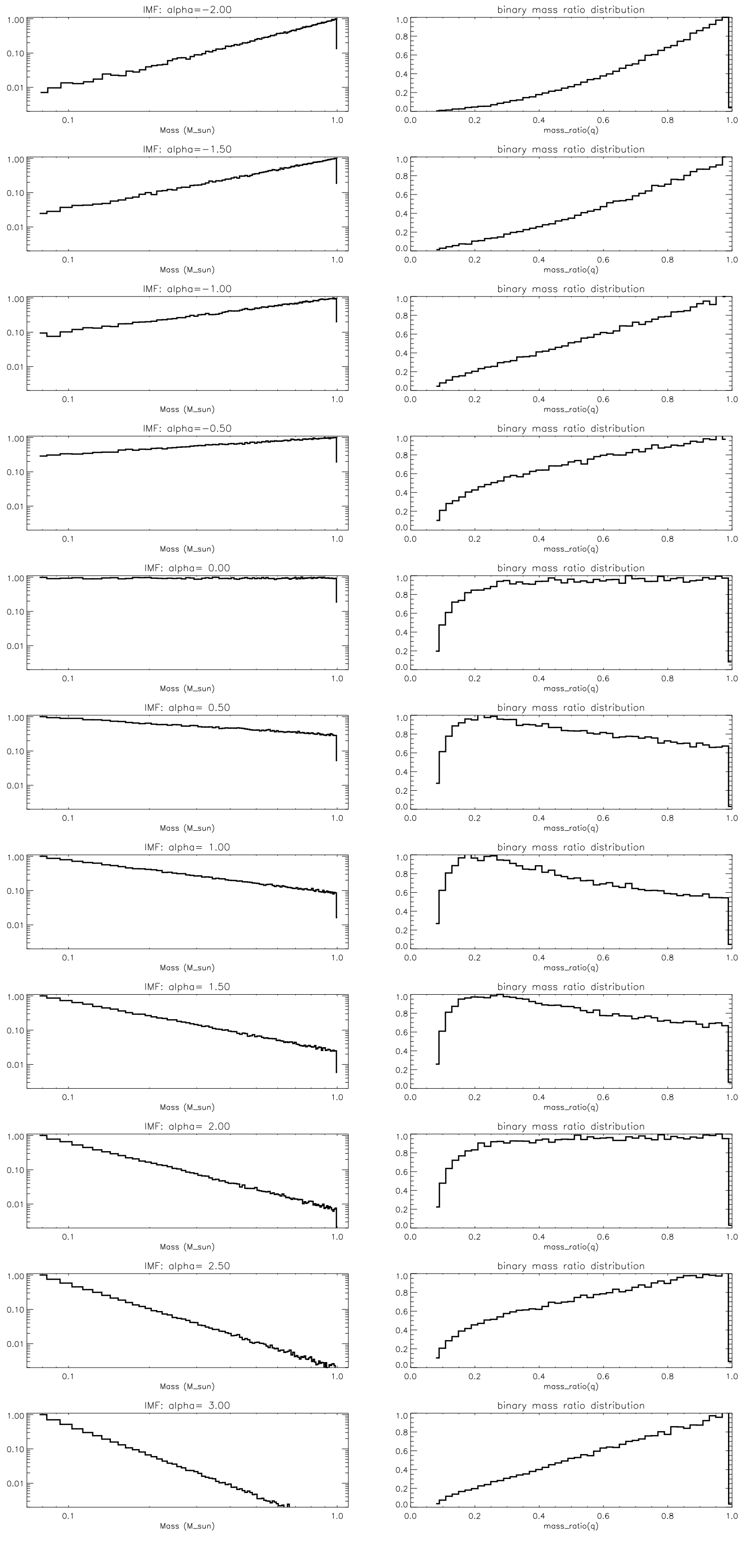

Figure D.1: Initial mass function and the resulted binary mass-ratio distribution for α in the range of [-2,3]. Left column: IMF at different power index α, with increment of 0.5; Right column: the resulted binary mass-ratio distribution.

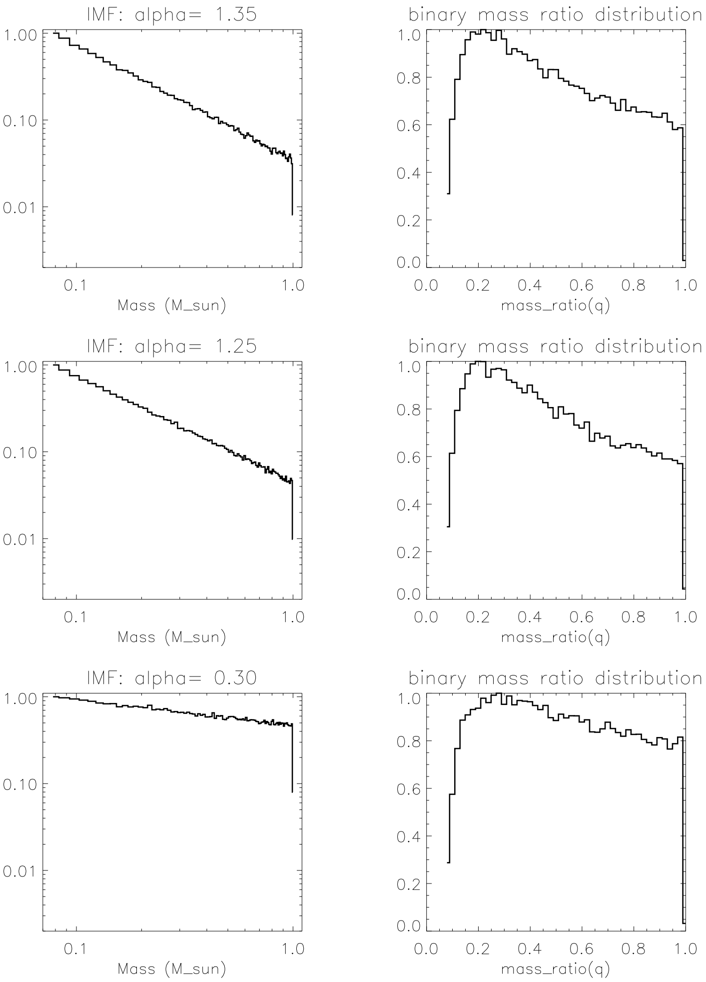

Figure D.**2:** Initial mass function and the resulted binary mass-ratio distribution for three common IMFs. Note: $\alpha = 1.35$ from Salpeter (1955); $\alpha = 0.3$, the median power index for low concentrated globular clusters from De Marchi et al. (2007).